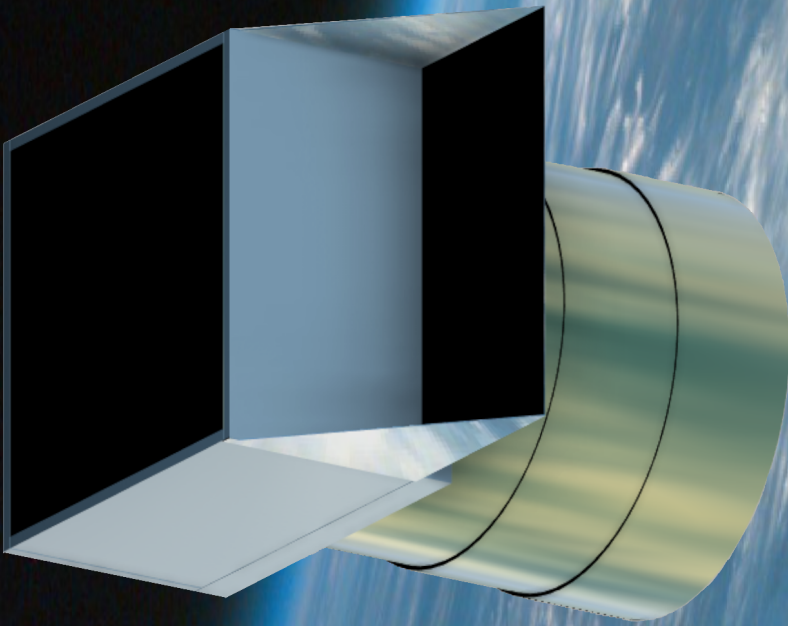


Passive Thermal Design of a Thermal Infrared Telescope

MSc. Thesis
Frank Eshuis

Delft University of Technology



Passive Thermal Design of a Thermal Infrared Telescope

by

Frank Eshuis

To obtain the degree of Master of Science
at the Delft University of Technology,
to be defended publicly on Thursday August 24, 2023 at 10:00.

Student number: 4560477

Thesis committee:

Daily Supervisor: Dr. ir. J. Bouwmeester TU Delft, SSE

Chair: Dr. A. Menicucci TU Delft, SSE

External: Ir. I. Uriol Balbin TU Delft, AS&M

Cover: Render of the DST, background image courtesy of NASA JPL [34]

Preface

Finally. This thesis is the culmination of years of being a student and I am happy to be finished. My interest in Aerospace Engineering originated ever since seeing a Space Shuttle launch more than a decade ago in Florida, and I am happy to have been able to work in a space-related field for my thesis.

I would like to thank Jasper Bouwmeester for providing me with the opportunity to work on this thesis and for his guidance throughout the process. I would like to thank the other members of the DST team. I would like to thank my friends and family for supporting me during this time. A special thanks to my mom and dad for always being there for me and inspiring my curiosity and always pushing me to continue.

*Frank Eshuis
Hengelo, August 2023*

Summary

This thesis reports the development of the thermal control system of the deployable space telescope (DST) demonstrator. The aim is to cool the thermal infrared (TIR) detector to at least 150 K (and lower) using only passive thermal control.

The decrease in the ground sampling distance of a telescope is typically accompanied by an increase in both volume and mass, increasing costs. The DST aims to reduce the stowed volume of the telescope and thus increase the volume efficiency and reduce cost. The DST functions in the TIR domain. The TIR domain imposes strict requirements on the detector temperature. The detector must be below 150 K, cooling the detector further improves performance. The detector requires a dedicated radiator to cool it sufficiently.

The starting point of this thesis was the collection of thermal and mechanical requirements. System inputs, such as the detector heat load or expected bus dissipation, were calculated. Design choices were made regarding the deployment mechanism, surface coatings, propulsion system, expected power allocation per subsystem, solar array, and bus temperature limits and specific heat. Subsequently, the initial model is created using computer-aided design (CAD). The components were characterized and adapted for the thermal modeling program ESATAN. The bus heat load is determined to be 50 W.

The bulk materials and coatings used in the model were defined. Conductors representing the mounting equipment of the instrument box and its internals were calculated. An initial radiator sizing was done using the model assumptions and detector heat load. This analysis showed that two radiators are necessary. The cryo-stage radiator cools the detector, and the cold-stage radiator cools the instrument box. Next, the thermal model is recreated in ESATAN. The conductive interfaces are investigated, and several conductors are added to more accurately represent the real situation. The initial thermal model showed that there was too much external heat input on the radiator surfaces, resulting in the detector and instrument box temperatures being too high. This prompted the addition of the Earth shade door. The Earth shade door provides (near-complete) shading for a portion of the radiator side panel. An investigation of the potential temperatures of the radiator side panel yielded an optimal cryo- and cold-stage radiator size of 7 cm by 36 cm, where the cryo-stage is flush with the Earth shade door.

The thermal analysis at full system level is done by performing several additional analyses. First, the orbit analysis demonstrated that the thermal control system's design held up for all orbits. The worst-case analysis indicated that the detector temperature would remain within the requirements. The insulated design of the instrument box results in a low thermal gradient. The sensitivity analysis revealed that the instrument box would become too warm with a bus heat load of 90 W, providing an upper limit for the current design configuration. The detector stayed within the temperature limit for a bus heat load of 150 W. The conductor analysis showed that the material used for the radiator, detector, and instrument box mounting is vital to its thermal performance and that low-conductivity materials must be used. The baffle analysis determined that the baffle design may function better if no MLI is used and that a high-conduction material may yield better results.

The thesis goal of passively cooling the detector to 150 K is achieved with a nominal-case detector temperature of 120.2 K. The Earth shade door is added to the thermal control system. The thermal control system functions for different sun-synchronous orbits, permitting constellation flight.

Contents

Preface	i
Summary	ii
List of Abbreviations	viii
1 Introduction	1
1.1 Background and Motivation	2
1.2 The DST project	2
1.2.1 The Secondary Mirror Deployment System	3
1.2.2 The Baffle	4
1.3 Theoretical Background	4
1.3.1 Conduction	4
1.3.2 Convection	4
1.3.3 Radiation	4
1.4 Spacecraft Thermal Control	5
1.4.1 Passive thermal control	5
1.4.2 Active Thermal Control	6
1.5 Thesis Overview	6
1.5.1 Thesis need and goal statement	6
1.5.2 Research questions	7
1.5.3 Thesis Deliverables	7
2 Thermal control system requirements	8
3 Thermal Model Input Generation	9
3.1 System Inputs	9
3.1.1 The Spacecraft Bus	9
3.1.2 Detector and Filter heat load	9
3.1.3 Orbit analysis	11
3.2 Design Choices	13
3.2.1 CubeSat deployment	13
3.2.2 Surface coatings	13
3.2.3 Propulsion system	15
3.2.4 Subsystem power allocation	16
3.2.5 The solar array	17
3.2.6 Important aspects of the spacecraft bus	18
3.3 Chapter Summary	19
4 Model Geometry Generation	21
4.1 The baffle	21
4.2 The optics	22
4.3 Nadir-Facing surface	23
4.4 Instrument Box	24
4.5 The Bus	25
4.6 CubeSat Structure	26
4.7 The Solar Array	26
4.8 Chapter Summary	26
5 The Thermal Model and Analysis	29
5.1 Thermal Model Bulk Materials and Coatings	29
5.1.1 Modeling of the MLI	31
5.2 Model Assumptions	31

5.3	Initial Radiator Sizing and Design	32
5.4	Conductive interfaces and conductors	34
5.4.1	MLI	36
5.5	Radiative Cases	37
5.5.1	Environment	37
5.5.2	Orbit Parameters	37
5.5.3	Satellite Pointing	37
5.6	The Analysis Case	37
5.6.1	Analysis case results	37
5.7	The Initial Thermal Model Results	38
5.8	Earth shade	39
5.9	Earth shade Sides	41
5.10	Radiator Area Optimization	43
5.11	Chapter Summary	47
6	Full system level Thermal Analysis	48
6.1	The orbit analysis	48
6.1.1	Simulation Tolerances and Long-term Temperature Evolution	50
6.2	Worst Case Analysis	52
6.2.1	Solar Constant	52
6.2.2	Albedo and OLR	52
6.2.3	Operating temperatures	53
6.3	Instrument box thermal gradient	54
6.4	Conductor Material Investigation	55
6.5	Sensitivity Analysis	56
6.6	Baffle (Re)design	56
6.6.1	Coating Analysis	57
6.6.2	MLI Analysis	57
6.7	Final Design	58
6.8	Chapter Summary	60
7	Conclusion and Future Work	61
7.1	Conclusion	61
7.1.1	Design Conclusions	62
7.2	Recommendations and Future Work	62
7.2.1	The Spacecraft Structure and Bus	62
7.2.2	Baffle (Re)design	63
7.2.3	The Earth Shade door	63
	References	64
A	Optimal radiator surface area results	68
B	Cold Stage Analysis	70
C	Worst Case Analysis Results	72

List of Figures

1.1	The original design of the VIS DST, taken from [22]	2
1.2	The design of the SMDS, taken from [33]	3
3.1	Sun-Synchronous orbital plane precession, taken from [21]	12
3.2	A diagram of orbital parameters, taken from [72]	12
3.3	A 1U CubeSat deployed using a rail system [68]	13
3.4	A 6U CubeSat deployment canister [26]	13
4.1	The design of the baffle with its dimensions, on the right a section view of the baffle	22
4.2	The CAD design of the optics, the primary mirror thickness is not to scale	23
4.3	The CAD design of the nadir-facing surface, with an isometric view of the components shown in the drawing, with the top two baffle sections removed	23
4.4	The CAD design of the instrument box, with an isometric view of the closed box and the top surface removed showing the two optical elements	24
4.5	The CAD design of the bus, with labeled subdivisions	25
4.6	A depiction of a sandwich panel, taken from [41]	26
4.7	The CAD model of the DST demonstrator	28
4.8	A section view of the DST demonstrator CAD model	28
5.1	The cryo and cold stage radiator temperatures plotted against the surface area	33
5.2	The geometry of the DST in ESATAN	33
5.3	Simplified thermal network diagram of the DST demonstrator	34
5.4	The automatically generated conductive interfaces, the conductive interfaces between the cryo- and the cold- stage have been removed, as well as between the cold stage and the R-side panel	35
5.5	A more in-depth view of the conductive interfaces	35
5.6	The two measurement points on the instrument box, viewed from the top	38
5.7	The detector and instrument box temperatures for the initial thermal model	38
5.8	The external and conductor heat flow for the initial thermal model	39
5.9	The geometry of the DST in ESATAN, with the Earth-shade door added	40
5.10	The average detector and instrument box temperatures plotted against the Earth Shade door length	40
5.11	The average external and conductor heat flow plotted against the Earth Shade door length	41
5.12	The geometry of the DST, with the Earth-shade door and its sides added, in cyan	41
5.13	The average detector and instrument box temperatures plotted against the Earth Shade side length	42
5.14	The average external and conductor heat flow plotted against the Earth Shade side length	42
5.15	The net heat flow	43
5.16	The net heat flow for the R-side panel	43
5.17	The potential temperatures for an Earth shade side size of 18 cm, using only the external heat input	44
5.18	The instrument box and detector temperatures for an increasing cryo stage radiator height	44
5.19	The external and conductor heat flows for the cryo and cold stage radiators	45
5.20	The detector and instrument box temperatures for a cryo-stage radiator height of 7 cm	46
5.21	The design of the cryo and cold stage radiators	46
6.1	The pointing configuration for the 10 AM (left) and 2 PM (right) orbits	49
6.2	The detector temperature per orbit	49
6.3	The external heat input on the sides of the spacecraft, during one orbit for the 6 and 12 PM SSOs	50
6.4	The detector temperature for the 6 PM SSO, for one and ten orbit durations	51
6.5	The detector temperature for the cases where the relaxation condition is tightened	51

6.6	The detector temperature for the SSO 6 pm orbit, during the entire mission timeline of 5 years	51
6.7	The detector temperature per orbit	54
6.8	The external heat flow for the baffle surfaces for different exterior surface coatings	57
6.9	The interior and exterior MLI face sheet temperatures for different MLI insulation values	58
6.10	The interior and exterior MLI face sheet temperatures for different MLI insulation values	59
A.1	The potential temperatures for an Earth shade side size of 9 and 10 cm	68
A.2	The potential temperatures for an Earth shade side size of 11 and 12 cm	68
A.3	The potential temperatures for an Earth shade side size of 13 and 14 cm	68
A.4	The potential temperatures for an Earth shade side size of 15 and 16 cm	69
A.5	The potential temperatures for an Earth shade side size of 17 and 18 cm	69
A.6	The potential temperatures for an Earth shade side size of 19 cm, using only the external heat input	69
B.1	The detector and instrument box temperatures for a cryo-stage radiator height of 7 cm	70
B.2	The detector and instrument box temperatures for a cryo-stage radiator height of 8 cm	70
B.3	The detector and instrument box temperatures for a cryo-stage radiator height of 9 cm	71

List of Tables

3.1	The orbits that will be used to analyze the thermal environment on the spacecraft.	11
3.2	A summary of potential thermal coatings	14
3.3	Potential representative propulsion systems for the DST demonstrator	16
3.4	The distribution of power requirements for the demonstrator model	17
3.5	The distribution of power requirements for the DST demonstrator model	20
3.6	The orbits that will be used to analyze the thermal environment on the spacecraft.	20
3.7	How each of the (sub)components will be modeled in the thermal model	20
3.8	The temperature limits of the spacecraft bus	20
5.1	The different components of the spacecraft and their corresponding materials and coatings. . .	30
5.2	The materials and their accompanying properties in ESATAN-TMS	30
5.3	The "known" coatings	30
5.4	A comparison of the conductivity and stiffness of detector mounting material	31
5.5	The conductors for the initial thermal model	36
5.6	The conductors for the MLI in the initial thermal model	36
6.1	The orbits that will be used to analyze the thermal environment on the spacecraft.	48
6.2	The solar constants for the hot, cold, and nominal cases	52
6.3	The albedo and OLR values for the hot and cold cases	52
6.4	The minimum and maximum temperatures and total temperature change for the 6 PM SSO . .	53
6.5	The minimum and maximum temperatures and total temperature change for the 12 PM SSO .	53
6.6	The updated coating configuration temperatures	54
6.7	The detector and instrument box temperatures for the different conductor materials	55
6.8	The bus heat load and accompanying temperature results for the sensitivity analysis	56
6.9	The baffle temperature range during one orbit for the specified coating	57
6.10	The baffle temperature range during one orbit for the different insulation values	58
6.11	The different components of the spacecraft and their corresponding materials and coatings. . .	59
C.1	The results for the 6 PM SSO nominal case in the worst case analysis	72
C.2	The results for the cold case - minimum OLR for the 6 PM SSO in the worst case analysis . . .	72
C.3	The results for the cold case - minimum albedo for the 6 PM SSO in the worst case analysis .	72
C.4	The results for the hot case - maximum albedo for the 6 PM SSO in the worst case analysis . .	73
C.5	The results for the hot case - maximum OLR for the 6 PM SSO in the worst case analysis . . .	73
C.6	The results for the 12 PM SSO nominal case in the worst case analysis	73
C.7	The results for the cold case - minimum OLR for the 12 PM SSO in the worst case analysis . .	74
C.8	The results for the cold case - minimum albedo for the 12 PM SSO in the worst case analysis .	74
C.9	The results for the hot case - maximum albedo for the 12 PM SSO in the worst case analysis .	74
C.10	The results for the hot case - maximum OLR for the 12 PM SSO in the worst case analysis . .	75
C.11	The bus temperature range for each orbit, in the cold case - minimum OLR	75

List of Abbreviations

Abbreviation	Definition
ADCS	Attitude Determination and Control System
CAD	Computer-Aided Design
CDHS	Command and Data Handling System
COM	Communications
DobST	Dobson Space Telescope
DST	Deployable Space Telescope
EPS	Electrical Power System
ESATAN	European Space Agency Thermal Analysis Network
GSD	Ground Sampling Distance
IR	Infrared
M1	The Primary Mirror
M2	The Secondary Mirror
MLI	Multi-Layer Insulation
ROIC	Readout Integrated Circuit
SMAS	Secondary Mirror Articulation System
SMDS	Secondary Mirror Deployment System
SMSS	Secondary Mirror Support Structure
TC	Thermal Control
TCS	Thermal Control System
TIR	Thermal Infrared
TSE	Thermal Self-Emission
VIS	Visual

1

Introduction

This thesis reports the development of the thermal control system of the deployable space telescope (DST) demonstrator. The aim is to cool the thermal infrared (TIR) detector to at least 150 K (and lower) using only passive thermal control. This chapter discusses the structure of the report, the background and the current state of the Deployable Space Telescope (DST) project, the underlying theory, and provides an overview of the thesis.

Earth observation allows for the collection of data that cannot be observed from the ground. Earth observation telescopes provide, among others, important insights into weather patterns, wildfire damage, or pollution levels. These satellites can become quite large if high-resolution images are required. The DST project aims to reduce the dimensions of the satellite in its stowed configuration, allowing more efficient use of the available space on the launcher platform. This reduces the costs associated with the satellite's launch. The DST demonstrator operates in the Thermal Infrared (TIR) domain. The desire for a compact system to operate on this wavelength of light creates several challenges. One of these challenges is the thermal control system (TCS). The remainder of this chapter provides background information and motivation for the DST, an initial look at the underlying theory of heat transfer, and an overview of the thesis. The requirements of the DST demonstrator's TCS are detailed in Chapter 2.

In Chapter 3 the heat inputs on the DST are investigated. The dimensions of the spacecraft, the expected power dissipation, the detector and filter heat loads, the orbits in which the DST might fly, the deployment mechanism, the coatings, the propulsion system, and the solar array are investigated, as they are relevant parameters for the thermal model. Where necessary, assumptions are made regarding these factors to arrive at the final set of assumptions for the model. The geometry generation that is used for the thermal model is detailed in Chapter 4. The baffle design is further investigated, and it is determined that it may become design-driving. The optical elements are adapted for analysis using ESATAN. The design of the nadir-facing surface is investigated, which holds the secondary mirror deployment system (SMDS), the primary mirror (M1), and the baffle. The dimensions of the instrument box and the satellite bus are determined. The solar array is omitted from the thermal model. The structural requirements of the satellite are assumed to be met by honeycomb panels of one cm thick, with face sheets of one mm thick.

The thermal model and analysis are detailed in Chapter 5. The design of the radiator(s) and the reduction of its heat inputs are elaborated. Coatings and bulk materials are defined. The model assumptions are investigated, and the radiator is divided into two stages, the cryo- and cold-stage. The conductive interfaces are created, and the manual (user-defined) conductors are defined. The radiative and analysis cases are elaborated upon. The initial thermal model is analyzed, and it is determined that the radiator heat input must be reduced. The addition of an Earth shade door allows the final design of the radiator-side panel to be made. Subsequently, Chapter 6 documents several smaller and more specific analyses, which together are used to investigate the behavior of the DST at the full system level. The orbital and worst-case analyses show that the design supports different orbits and stays within temperature limits. The thermal gradient of the instrument box is determined, and the sensitivity analysis alleviates concerns regarding the bus heat input as determined in Chapter 3. The choice of conductor material is investigated and the baffle coating arrangement is elucidated.

Finally, in Chapter 7, conclusions and recommendations are given for future work. Answers to the main research question and subquestions are given. The feasibility and sensibility of the design choices made in Chapter 5 is discussed.

1.1. Background and Motivation

The DST is a thermal infrared (TIR) Cassegrain telescope that observes the Earth in the TIR domain (8-12 μm). Telescopes operating in the TIR domain absorb the infrared (IR) radiation on the detector. The IR radiation is then converted into an electrical signal, which can be used to obtain various insights. IR telescopes provide insight into weather and ocean patterns, crop and forest conditions, and may also be used for military applications. Earth observation satellites provide observational data on the regions over which they fly. The resolution, or ground sampling distance (GSD), of said data depends on various factors. The (diffraction-limited) GSD is calculated according to Equation 1.1. As an example, a GSD of 1 m means that one pixel in the image represents 1 m linearly on the ground, or $1 \cdot 1 = 1 m^2$.

$$GSD = 2.44 \frac{h\lambda}{D} \quad (1.1)$$

Where h is the orbital altitude, λ is the wavelength, and D is the aperture diameter. As can be seen, if it is assumed that the system is diffraction-limited and that the observed wavelength does not change, then either the orbital altitude must be reduced or the diameter of the aperture must be increased to decrease the GSD. Both of these options carry significant consequences for a satellite's design. Decreasing the orbital height will increase the orbital drag, resulting in a shorter mission lifetime and higher heat input due to higher propulsive power requirements. Increasing the aperture diameter will increase the mass and volume of the satellite.

Therefore, alternate approaches to reducing the GSD are investigated and have led to the DST project. The DST project aims to provide a high GSD in comparison to its cost, compared to other Earth observation satellites. The DST demonstrator is highly compact and deploys its baffle and secondary mirror once it is in space. This allows the DST to have a high volume efficiency, resulting in lower costs.

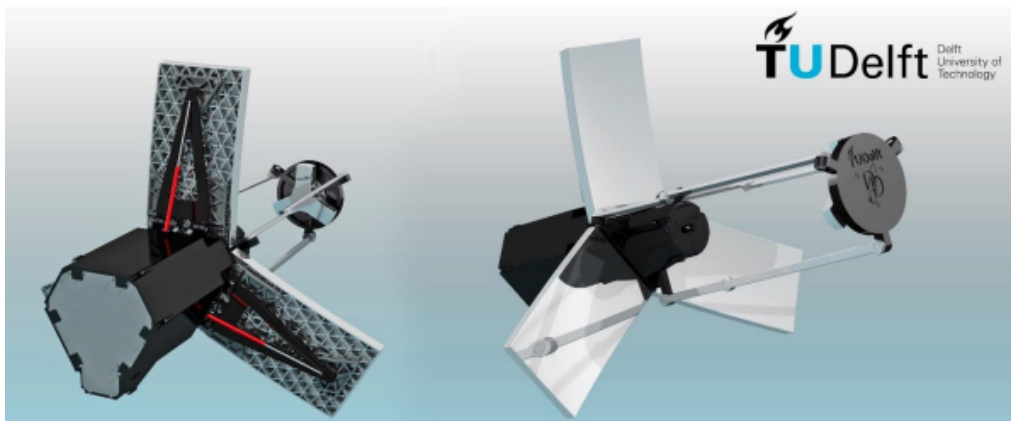


Figure 1.1: The original design of the VIS DST, taken from [22]

1.2. The DST project

The DST project was started in 2015, after the thesis of Dennis Dolkens.[22] In this thesis, the conclusion was made that the DST can reach a high ground resolution, combined with a low stowed volume. This low stowed volume is achieved by designing the telescope to deploy once it has reached its orbital destination. In this way, its deployed volume is much larger than its stowed volume. The team working on the DST project consists of TU Delft staff, Ph.D. students, and MSc students. The DST was initially designed to operate in the visual spectrum, with an aperture of 1.5 m. The initial design of the DST is shown in Figure 1.1. The aperture (or primary mirror) was initially designed to be deployable together with the secondary mirror and the baffle. Later, it was decided that the DST would switch to the TIR domain, as it was considered more lucrative. The iteration of the project that is the subject of this thesis is the TIR DST demonstrator. The DST demonstrator is a smaller version of the TIR DST with an aperture of 30 cm. The aperture is not deployable for the DST demonstrators' design. The external dimensions of the DST demonstrator are those of a 27U CubeSat, 34x35x36 cm, for a volume of approximately 43 liters.

The detector is a vital component of the DST telescope. An IR detector is highly temperature sensitive and

functions best when its temperature is low, and better when its temperature is reduced further. This is caused by the reduction in thermal noise and dark current as the temperature is reduced. IR detectors are typically constructed of Mercury Cadmium Telluride (MCT). [3] In the past, IR detectors were cryogenically cooled to temperatures below 80 K. Typically, 77 K is used as the reference temperature, since the coolant liquid that was typically used, liquid nitrogen, exists at this temperature. [57] Current developments are working to reduce the dark current of detectors, which would allow better performance or higher operating temperatures. Dark current is the charge collected by a detector in the absence of light. By reducing the dark current, the operating temperature for an MCT detector in the LWIR ($10\ \mu\text{m}$) domain has been shown to have increased to 160 K.[42] As another example, the LandSat-9 TIRS-2 detector operates at a wavelength comparable to that of the DST demonstrator ($10\text{-}12\ \mu\text{m}$), and its detector is cooled to 185 K. [1]

No design choice has been made for the detector at this time. Therefore, for this thesis, a temperature limit of 150 K, or $-123.15\ ^\circ\text{C}$, is set for the detector, with the intention of reducing this temperature as low as possible. The rejection of the detector heat load, as well as the other components to which the detector is directly or indirectly connected, is of utmost importance. The radiator and coating design are investigated in detail so that the detector can be cooled as much as possible.

1.2.1. The Secondary Mirror Deployment System

The secondary mirror is deployable, allowing for an increase in the volume efficiency of the DST compared to a fixed telescope. This is achieved using the SMDS, shown schematically in Figure 1.2. The SMDS for the DST demonstrator has been investigated in the work of Hobijn, [33]. The stowed height of the SMDS is approximately 7 cm, and its deployed height is 25 cm. The SMDS holds the secondary mirror, using the secondary mirror support structure (SMSS) and the secondary mirror articulation system (SMAS). The SMAS is used to ensure that the deployment accuracy is within the specified limits.

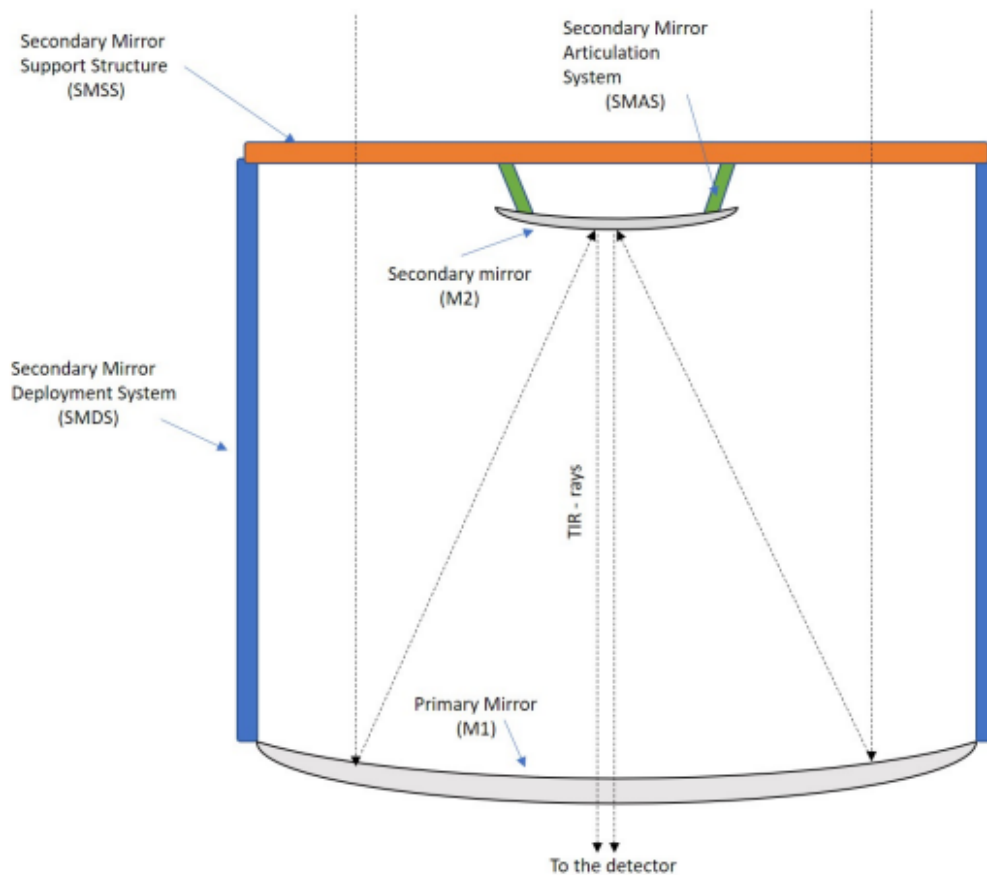


Figure 1.2: The design of the SMDS, taken from [33]

1.2.2. The Baffle

Stray light from the environment has the potential to negatively affect the image. Therefore, a deployable baffle is used to limit the light that is incident on the primary mirror. An initial analysis of the baffle has been carried out in the work of Hu, [35]. The stowed length of the baffle is estimated at 12 cm, and the deployed length is 33 cm. Currently, the baffle is coated on the inside with a highly absorptive ultra-black coating. This coating minimizes any unwanted reflection inside the baffle from reaching the detector.

1.3. Theoretical Background

A short overview of the underlying theory of heat transfer is given. The temperature change in a body is given by Equation 1.2:

$$Q = mc_p\Delta T \rightarrow Q_{in} - Q_{out} = mc_p\Delta T \quad (1.2)$$

Where Q_{in} is the incoming heat, Q_{out} is the outgoing heat, m is the mass of the body, c_p is the specific heat capacity of the body, and ΔT is the heat difference in the body. If the mass, specific heat, Q_{in} and Q_{out} are known, then the increase or decrease in temperature can be calculated at a given time. Q_{in} represents the internal power generation or incoming heat transfer. Q_{out} represents the heat loss by heat transfer. In the following subsections, a short overview of the methods of heat transfer and how they apply to the thermal analysis of the DST demonstrator are given.

1.3.1. Conduction

Conduction is the main method of heat transfer between spacecraft components. Conduction depends on the conductivity, k , of the material, the cross-sectional area, A , of the thermal path, the path length, x , and the temperature difference. The area and path length are dependent on the design, whereas the conductivity is material-dependent. The material and design can be changed should this be required to minimize or maximize conduction.

$$Q = k\frac{A}{x}(T_1 - T_2) \quad (1.3)$$

1.3.2. Convection

Convection is the heat transfer that occurs due to the interaction between fluid and geometry. Equation 1.4 shows the equation for convective heat transfer. h is the heat transfer coefficient, A is the area over which heat transfer occurs, and $T_1 - T_2$ is the temperature difference. For this thesis, it is assumed that there is no convection as there is no "fluid" (air) to support this method of heat transfer in space.

$$Q = hA(T_1 - T_2) \quad (1.4)$$

1.3.3. Radiation

Thermal radiation is electromagnetic radiation generated by the thermal motion of particles in matter. Thermal radiation is generated when heat from the movement of charges in the material (electrons and protons in common forms of matter) is converted to electromagnetic radiation. All matter with a temperature greater than absolute zero emits thermal radiation. Solar radiation is typically the largest external input of thermal energy for a satellite.

$$P = A\epsilon\sigma T^4 \quad (1.5)$$

The power radiated away from a (black) body can be calculated by the Stefan-Boltzmann law. The Stefan-Boltzmann law is shown in Equation 1.5. The radiated power depends on the emissivity, ϵ , the emitting surface area, A , the Stefan-Boltzmann constant, σ , with a value of $5.67\text{e-}8 \frac{\text{W}}{\text{m}^2\text{K}}$, and the temperature, T , in Kelvin.

The radiative heat transfer between two surfaces can be calculated according to the following equation:

$$Q = \sigma\epsilon_{IR}A_1F_{1-2}(T_1^4 - T_2^4) \quad (1.6)$$

Where A_1 is the surface area of the emitting surface, F_{1-2} is the view factor from surface 1 to surface 2, T_1 is the temperature of the emitting surface, and T_2 is the temperature of the receiving surface.

The view factor relates the proportion of radiation that leaves surface 1 and hits surface 2. The sum of all view factors from any given surface equals 1. It is possible that a surface "sees" itself (cylindrical geometries,

for example), which means that it radiates heat to itself. Determining the view factors is a computationally intensive process, depending on the method used. [31]

The solar absorption of a surface is one of the primary aspects of satellite thermal design. The solar absorption is shown in the following equation:

$$Q_{abs} = A_{abs} J_s \alpha_S \quad (1.7)$$

Where A_{abs} is the area that receives solar heat flux, J_s is the solar heat flux, which has an average value of $1367 \frac{W}{m^2}$ at earth's distance, and α is the absorptivity of the given surface.

Thermo-optical properties

The emissivity, ϵ , and absorptivity, α , of a surface coating represent these values in the IR spectrum and solar spectrum, respectively. For a given coating, the emissivity and absorptivity are equal in their specified spectrum (the emissivity in the IR spectrum is equal to the absorptivity in the IR spectrum). The sum of the emissivity/absorptivity, reflectivity, and transmissivity in the IR/solar spectrum equals 1, as shown in Equations 1.8 and 1.9. Unless otherwise stated, it is assumed that all coatings are opaque and that the transmissivities, τ_{IR} and τ_S , are assumed to be 0.

$$\epsilon_{IR} + \rho_{IR} + \tau_{IR} = 1 \quad (1.8)$$

$$\alpha_S + \rho_S + \tau_S = 1 \quad (1.9)$$

ρ_{IR} and ρ_S are the reflectivities in the IR and solar spectra. This reflectivity is the sum of two distinct reflectivity values, the specular and the diffuse reflectivity. Specular reflection reflects all light with the same incidence angle and typically occurs when light is incident on a mirror. Diffuse reflectivity reflects light in a broad range of directions.

1.4. Spacecraft Thermal Control

The thermal control (TC) of a satellite is of utmost importance. The TC of a satellite can be done in two ways, active or passive TC. Passive TC is typically preferred, as passive TC is less complex, is thus easier to use, and is less expensive (design-wise). However, this depends on the specific case. The required dimensions of a passive system may become too large, making the usage of passive TC no longer feasible. Active TC is typically used if the passive TC cannot meet the requirements, such as size or required temperature range. Active TC will add complexity to the design as additional parts and/or mechanisms are required.

1.4.1. Passive thermal control

There is a wide range of possibilities for passive cooling. The most important methods of passive TC are the spacecraft's coatings, Multi-Layer Insulation (MLI), and radiators. The major constraint for a passive TC system is that heat can only flow from hot to cold. Heat pipes and highly conductive metal straps can be used to improve conduction and reduce the temperature difference between connected components.

MLI

MLI blankets are the most efficient thermal insulation for space applications. An MLI blanket is typically made of a certain number of low-emittance sheets combined with low-conduction netting layers to control heat transfer for low-temperature applications, such as cryogenic instruments. The thermal insulation performance is quantified as the effective emissivity (ϵ^*). It depends on the number of inner layers and geometric considerations. The effective emissivity is defined as in Equation 1.10. [49]

$$\epsilon^* = \frac{q_{total}}{\sigma(T_{hot}^4 - T_{cold}^4)} \quad (1.10)$$

Where q_{total} is the heat transmitted through the MLI blanket (W/m^2), T_{hot} is the temperature of the MLI hot side (K), and T_{cold} is the temperature of the MLI cold side (K). The typical values for ϵ^* are in the range of 0.015 to 0.03 but can be much lower. [49].

Thermal conduction across the thickness of the MLI is very sensitive to layer compression (as this would cause a thermal "short circuit"). To minimize MLI conductive heat transfer, any compressive pressure or bending of the blankets must be avoided. [49] MLI efficiency decreases as the size of the blanket decreases

because the heat transfer at the edges of the blanket increases relative to total heat transfer. Therefore, MLI generally does not perform well on smaller satellite platforms. [51]

As the number of layers of MLI increases, so does the effective emissivity, as shown in Equation 1.11. [65]

$$\epsilon^* = \frac{1}{\frac{1}{\epsilon_{out}} + \frac{1}{\epsilon_{in}} - 1} \left(\frac{1}{N+1} \right) \quad (1.11)$$

Where N is the number of layers and ϵ_{out} and ϵ_{in} are the emissivities of the outside and the inside of each of the layers, respectively. MLI is more effective with a decrease in effective emissivity. The effective absorptivity of an MLI blanket is related to the effective emissivity, as shown in Equation 1.12. [10],[44]

$$\alpha^* = \epsilon^* \frac{\alpha_{out}}{\epsilon_{out}} \quad (1.12)$$

Where α^* is the effective absorptivity in the solar spectrum, and α_{out} is the absorptivity of the outermost layer in the solar spectrum. This equation works only under the assumption that there is only radiative heat transfer and no conductive heat transfer between the layers of the MLI.

Radiators

Radiators are dedicated surfaces that are used to radiate heat away from the spacecraft. They may be single-faced (body-mounted) or double-faced (deployable radiators). Radiators can be a challenge for smaller satellites, as the available space is heavily contested by other components, such as solar panels. The radiator surface may be painted or coated, depending on the required emissivity and absorptivity. The radiative heat transfer is defined as follows: [61],[51]

$$Q_{rad} = A_{rad} \epsilon_{IR} \sigma F_v (T_{rad}^4 - T_s^4) \quad (1.13)$$

Where Q_{rad} is the radiative heat transfer, A_{rad} is the surface area of the radiator, ϵ is the emissivity of the radiator, T_{rad} is the surface temperature of the radiator, T_s is the deep space temperature and F_v is the view factor of the radiator to deep space. Ideally, the view factor of the radiator to deep space is 1, and 0 to the Sun and Earth. If another component partially obstructs the radiator, then the view factor and radiative heat transfer to deep space are reduced.

1.4.2. Active Thermal Control

Active TC can allow certain components to be cooled to much lower temperatures, or the temperature stability may be greatly improved by incorporating a heater into the design. Other options for active TC, such as thermoelectric coolers or heat pumps, may also be used to manage the thermal system. [51] Active TC can allow for the transfer of heat from a colder surface to a warmer surface, for example, by using a stirling cryocooler. However, adding such a system to the DST demonstrator will greatly introduce design complexity. In addition, power consumption is greatly increased. To move heat from a cold end to a hot end, the stirling cryocooler requires power, significantly inflating the power budget of the satellite. For this thesis, the desire is to cool the detector as cold as possible using passive TC. Therefore, active TC will not be considered further.

1.5. Thesis Overview

The previous sections have detailed the challenges facing the thermal design of the DST demonstrator, the applicable heat transfer methods, and the applicable thermal control methods. The detector must be cooled to (near) cryogenic temperatures. The project aims to provide a low-cost and high-performance system. Active thermal control adds complexity to the design, increases mission costs, and adds a potential point of failure. Therefore, in this thesis, the possibility of passive cooling of the DST demonstrator is investigated.

1.5.1. Thesis need and goal statement

There is a need to constrain the temperatures of the DST within its specified limits, with the main challenge the required cooling of the detector to a maximum of 150 K and the instrument box to a maximum of 200 K.

The thesis objective is the design of a radiator that results in detector and instrument box temperatures that meet the specified requirements for all relevant orbit configurations.

1.5.2. Research questions

The main research question is formed from the literature study:

"How can the Thermal Control System of Earth observation satellites in a constellation be optimized to meet operational requirements?"

The main research question is subdivided into smaller research questions, which provide the pieces to answer the main research question.

1. "Where do the limits of radiators in a low Earth orbit lie?"
2. "To what extent is the orbit choice a design driver for the thermal control system of a satellite?"

1.5.3. Thesis Deliverables

The main deliverable of this thesis is the thermal model of the DST demonstrator. Several additional analyses are done that provide a more complete image of the DST's thermal behavior for different orbits and varying environmental conditions.

1. The final thermal model is shown in Section 6.7
2. The additional analyses are done in Chapter 6

2

Thermal control system requirements

In this section, the requirements for the DST demonstrator are elaborated upon. The requirements that will be considered are the requirements that are relevant for the design of the DST demonstrator TCS.

Driving requirements

- **Mass (g)**
The mass of the thermal control system.
- **Volume (m^3)**
The volume of the thermal control system in the stowed and deployed configuration.
- **Detector Temperature (K)**
The temperature of the detector.

Mass

The mass concerns all components of the TCS, including the radiator, any thermal hardware such as thermal straps or thermal tape, and insulation. Since launch costs are directly related to mass, the mass should be optimized to be as low as possible. A mass approximation for the TCS has not yet been made; therefore, the general desire for this aspect will be to make the TCS as light as possible while maintaining functionality.

Volume

The volume of the TCS concerns all components of the TCS that can contribute to the stowed and deployed volume. From the literature study, it was determined that it may be necessary to include some manner of deployability in the design of the TCS. Should such a system be part of the final design for the TCS, its volume should be minimized, especially in the stowed configuration, so that launch costs are suppressed.

Detector Temperature

The cooling of the detector is the main function of the TCS. The detector temperature is directly related to the performance of the DST demonstrator. Depending on the specific detector used, the detector temperature requirement can be 150 or 80 K. The maximum temperature of the detector is set at 150 K. Since reducing the detector temperature results in better images, the detector temperature is also considered a driving requirement, where the detector temperature should be as low as possible.

Instrument box Temperature

The cooling of the instrument box is the TCS's secondary function. The instrument box is conductively and radiatively connected to the detector and thus has the most significant impact on the detector temperature outside of the detector itself. The maximum temperature of the instrument box is set at 200 K, from previous analyses. Since reducing the instrument box temperature indirectly reduces the detector temperature, this requirement is also considered a driving requirement, with a lower priority than the detector temperature requirement.

Thermal Model Input Generation

In this section, the required information for the thermal modeling of the DST demonstrator is investigated, and where necessary approximated. The dimensions of the spacecraft, the power usage, power generation, the detector heat load, the orbits, the deployment mechanism, the coatings, the propulsion system, and the solar array are all important parameters for the thermal model. Some of these parameters are as of yet unknown, or only assumptions have been made. Therefore, in this chapter, these aspects of the model are investigated, and preliminary choices/assumptions are made, where possible.

3.1. System Inputs

3.1.1. The Spacecraft Bus

To model the thermal behavior of the spacecraft, the spacecraft bus must be analyzed. The spacecraft bus is the main body of the spacecraft and houses the components and payload. These components are the Attitude Determination and Control System (ADCS), the Command and Data Handling System (CDHS), Communications (COM), Electrical Power System (EPS), and Thermal Control System (TCS) (if an active TCS is used). At this moment, no design for the spacecraft bus for the DST has been made (yet). An in-depth bus design is out of the scope of this thesis project. However, since various important inputs are dependent on the spacecraft bus, approximations will be made using comparable projects.

The Dobson Space Telescope (DobST) is used as a reference. The DobST is a spacecraft that is very similar to the DST. The DobST-35 design has a primary mirror of 35 cm diameter, compared to the DST's 30 cm. The DobST works in the visual spectrum compared to the DST which works in the infrared spectrum. It is assumed that this does not affect the power requirements. The DobST-35 has an average power draw of 20 W, up to a maximum value of 50 W.[28] The maximum power draw includes the discharging of internal batteries. The DST is assumed to require a propulsion system. The final power requirements that will be used for the model are determined in Section 3.2.4.

The dimensions of the spacecraft also depend on the bus. The size of the bus is also related to the driving dimension, which is the diameter of the primary mirror, 30 cm. For a 27U CubeSat, deployer standards have been devised. Since a CubeSat is typically deployed using a canister (see Section 3.2.1, the dimensions of the spacecraft are tied to the specifications of the CSD (Canisterized Satellite Dispenser). For a 27U CubeSat, this provides limits for the mass, 54 kg, and the dimensions, 34-35-36 cm. These dimensions will be assumed to be leading in this thesis.[25]

3.1.2. Detector and Filter heat load

The detector temperature is a driving requirement for the DST demonstrator. The heat input on the detector comprises the signal heat load, the enclosure heat load, the optics heat load, and the readout integrated circuit (ROIC) heat load. In the thermal model, the detector will be modeled with a constant applied heat load, which will be determined in this subsection.

The signal heat load is calculated by the following equation:

$$Q_{det,signal} = \alpha\rho Q_{IR} \quad (3.1)$$

Where α is the absorptivity, which is assumed to be one. ρ is the reflectivity of the optical chain, which is also assumed to be one. This implies that all light entering the aperture reaches the detector. The DST sees an

area of 7.5 km by 7.5 km, equivalent to a circle with a diameter of 10.6 km. $Q_{aperture}$ is the aperture heat load, calculated using Lambertian theory. The heat flux collected by the aperture is calculated according to the following equation:[55]

$$Q_{IR} = \frac{L_{IR}A_0}{z_0^2} A_{aperture} \quad (3.2)$$

Where L is the radiance of the surface in $\frac{W}{m^2 sr}$, A_0 is the surface area of the radiating surface, $8.824e7 m^2$. Where $\frac{A_{aperture}}{z_0^2}$ is the solid angle and its unit is the steradian (sr).[55] z_0 is the orbital altitude, $3e5 m$, and $A_{aperture}$ is the aperture area, $0.0707 m^2$. The radiance of a surface, depending on the wavelength, is given by the following equation: [55]

$$L_\lambda = \frac{\rho_\lambda E_\lambda}{\pi} \quad (3.3)$$

Where ρ_λ is the reflectivity of the surface at the specified wavelength and E_λ is the incoming flux at the specified wavelength. For the detector heat load, $\rho_\lambda E_\lambda$ is replaced by the spectral radiance of the Earth in the TIR wavelength with a wavelength range of 4 microns. The Earth's temperature is assumed to be 300 K. The spectral radiance of the Earth at the peak wavelength of 10 microns can then be calculated according to the following equation: [56]

$$B(\lambda) = \frac{2\pi hc^2}{\lambda^5} \frac{1}{e^{\frac{hc}{\lambda k_b T}} - 1} \quad (3.4)$$

Where h is Planck's constant, $6.626e-34$, c is the speed of light at $300e6$, and k_b is the Boltzmann constant, $1.38e-23$. This yields a spectral radiance of $3.1e7 \frac{W}{m^3}$. Multiplying this number by the width of the spectral band, 4 microns, yields a flux of $124.18 \frac{W}{m^2}$. Entering this and all other values into Equation 3.6 results in a heat flux of 2.74 mW or 0.00274 W.

The enclosure heat load is calculated by the following equation:

$$Q_{enc} = \epsilon_{enc} A_{det} \sigma (T_{enc}^4 - T_{det}^4) \quad (3.5)$$

Where the emissivity of the enclosure is assumed to be one. The detector surface area has not been determined yet. Therefore, the assumption is made that the detector has a diameter of 1 cm and a negligible thickness. Finally, it is assumed that the rear surface of the detector is used to attach the cold finger, meaning that no radiation can impinge on the rear surface of the detector. This results in an effective detector surface area of $7.853e-5 m^2$. The enclosure temperature and detector temperature are the subjects of this thesis. Therefore, their actual value is unknown. Therefore, the desired temperature will be used in this calculation. The desired enclosure temperature is 200 K and the desired detector temperature is 80 K. This results in an enclosure heat load of 0.00694 W. Further analysis should be done on whether a baffle around the detector is required when the final detector (dimensions) has been determined.

The optics heat load and the read-out integrated circuit heat load were determined by Lars Boer. [14] The optics heat load, Q_{opt} , is 0.000412 W. The read-out integrated circuit heat load, Q_{ROIC} is 0.008 W. This provides a total detector heat load, Q_{det} , of 0.018 W rounded to 0.02 W for the analysis.

The visible light heat load

The visible light heat load must be removed from the incoming light so that it does not impact the detector. Therefore, a filter is added before the detector in the optical chain. The visible light is again calculated assuming a Lambertian source, where the heat input is due to the (diffuse) reflection of sunlight. The magnitude of the reflected light depends on the conditions under which the DST is flying at a given point in time. The oceans, the poles, and the clouds all have different values, with clouds resulting in the highest reflection. The cloud albedo is assumed to be 0.8, representing a worst-case scenario. The heat flux collected by the aperture can then be calculated again according to the following equation:[55]

$$Q_{vis} = \frac{L_{vis}A_0}{z_0^2} A_{aperture} \quad (3.6)$$

All values other than L_{vis} are the same as in Equation 3.2. The previously calculated TIR heat load is a portion of the total radiance in the IR spectrum. Therefore, the remaining amount of IR radiation is included

in the filter heat load as a worst-case assumption. The radiance in the infrared spectrum is calculated by the Stefan-Boltzmann law:

$$P = \sigma T^4 \quad (3.7)$$

Where σ is $5.67\text{e-}8$, and the temperature is 300 K. This yields a radiance of $459.27 \frac{W}{m^2}$. The total radiance incoming on the surface is then: [55]

$$L = \frac{\rho S + P - L_{IR}}{\pi} \quad (3.8)$$

Where ρ is the reflectance, or the albedo of the surface, assumed to be 0.8. S is the solar intensity, approximately $1360 \frac{W}{m^2}$. This yields a total radiance of $454 \frac{W}{m^2 \cdot sr}$. Entering all values in Equation 3.6 results in a heat flux of 31.5 mW or 0.0315 W. The final filter heat load is then rounded to a total value of 0.032 W.

3.1.3. Orbit analysis

The orbit analysis is done to provide a characterization of the orbital parameters that determine the thermal environment to which the spacecraft will be exposed. Since the demonstrator will perform earth observation, sun-synchronous orbits are obvious candidates for the orbit choice. These orbits all exhibit different thermal environments, with variations in eclipse times and which surfaces are sunlit, among other factors. All orbits are assumed to be circular. The orbits that will be modeled are shown in Table 3.1.

Orbit	Semi-major axis (a) [km]	Inclination (i) [deg]	Right ascension (RAAN) [deg]
Sun-synchronous 12 PM	300 (+6371)	96.648	0
Sun-synchronous 2 PM	300 (+6371)	96.648	30
Sun-synchronous 4 PM	300 (+6371)	96.648	60
Sun-synchronous 6 PM	300 (+6371)	96.648	90
Sun-synchronous 8 PM	300 (+6371)	96.648	120
Sun-synchronous 10 PM	300 (+6371)	96.648	150
Sun-synchronous 12 AM	300 (+6371)	96.648	180

Table 3.1: The orbits that will be used to analyze the thermal environment on the spacecraft.

The sun-synchronous orbit

An SSO precesses through one complete revolution each year so that it remains in the same orientation to the sun. This is achieved by having an orbital inclination slightly higher than 90° , typically between 96.5 and 102.5 degrees. This allows an SSO to provide global coverage at almost all latitudes (except a few degrees from the poles).[12] Figure 3.1 shows how a Sun-synchronous orbit develops during the orbit. As can be seen, the angle α remains constant between the orbit and the Sun.

With the Sun angles in Figure 3.1 measured counterclockwise relative to the Sun-Earth line, the zero angle corresponds to 12 PM, 90 deg to 6 PM, 180 deg to 12 AM, and 270 deg to 6 AM. To provide a constant Sun angle, the satellite's orbital plane (or equivalently the line of nodes) must precess at a rate of one revolution per solar year, i.e., $(360 \text{ deg} / 365.24 \text{ days}) = 0.9856 \text{ deg/day}$. [11]

The required inclination of the orbit to precess 0.9856 deg/day is dependent on the altitude. The inclination is related to the semi-major axis according to the following equation:

$$\cos(i) = -\left(\frac{a}{12352}\right)^{\frac{7}{2}} \quad (3.9)$$

This yields an orbital inclination of 96.648° for an orbital altitude of 300 km.

Mean Local Time

The mean local time is necessary to define the "time" of an SSO. It relates to the sun angle as shown in Figure 3.1. The mean local time (in hours) at the ascending node is given by the following equation:

$$MLT = \left(24 \frac{(\Omega + \delta)}{360}\right) \text{ mod } 24, \text{ where } \delta = 180 - 360 \left(\frac{\text{Days since Vernal Equinox}}{365.242199}\right) \quad (3.10)$$

Where the vernal equinox occurs on March 20 at various times, e.g., at 17:32 UTC in 2010. In Eq. (3) above, $(\Omega + \delta)$ is the angle (measured from the ascending node) between the line of nodes and the Sun-Earth line.

The time since the vernal equinox appears in Equation 3.10. It accounts for the precession of the orbital plane because Ω is defined relative to the direction of the vernal equinox, as can be seen in Figure 3.2. [11]

Assuming that the thermal model is run at the vernal equinox, the required right ascension (RAAN) can be determined for the orbits. This yields a right ascension, Ω , of 0 for the 12 PM orbit, a right ascension of 30° for the 2 PM orbit, a right ascension of 60° for the 40 PM orbit, and a right ascension of 60° for the 6 PM orbit, continuing until a right ascension of 180° for the 12 AM orbit. More broadly, the right ascension increases by 15° for each hour after 12 PM.

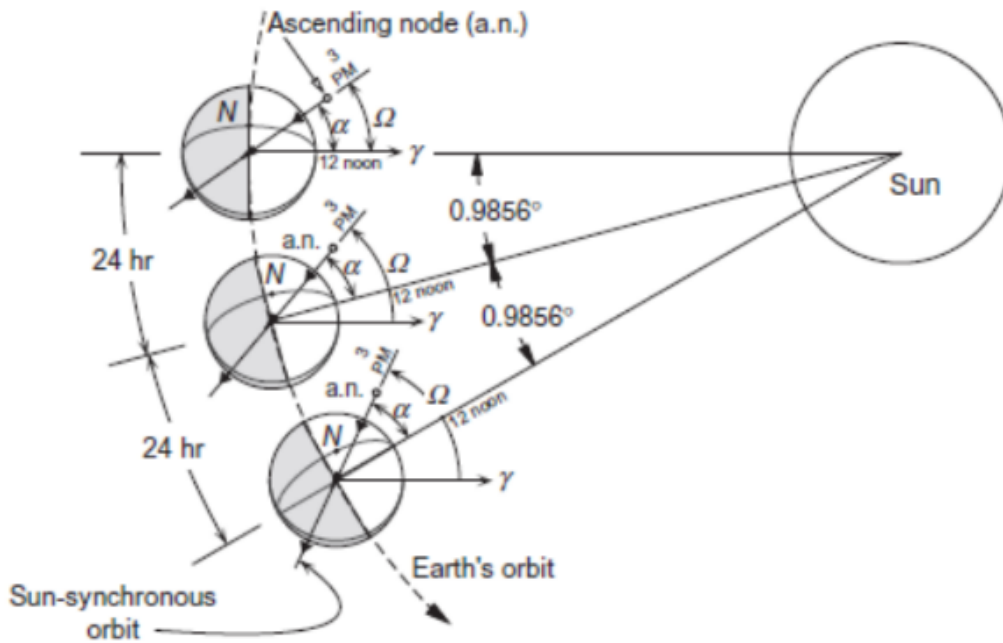


Figure 3.1: Sun-Synchronous orbital plane precession, taken from [21]

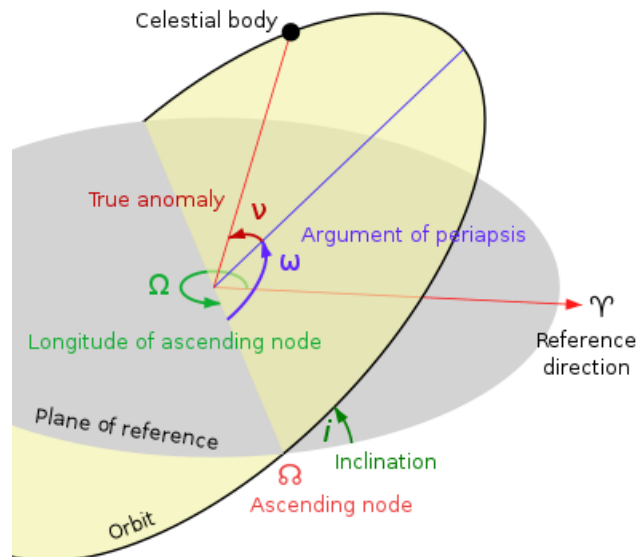


Figure 3.2: A diagram of orbital parameters, taken from [72]

3.2. Design Choices

3.2.1. CubeSat deployment

The CubeSat deployment methods affect the potential coatings and insulation that can be applied to the spacecraft. Thus, the deployment method is investigated. CubeSats are typically deployed via a canister. This canister may use certain techniques to deploy the CubeSat. Smaller CubeSats are typically deployed using a rail system. This requires the corners of the satellite to be clear of any components as the rails must be free. This method is shown in Figure 3.3. This method of deployment results in the segregation of the surfaces. For example, it is not possible to use an MLI blanket on 2 adjacent surfaces without breaking the blanket.

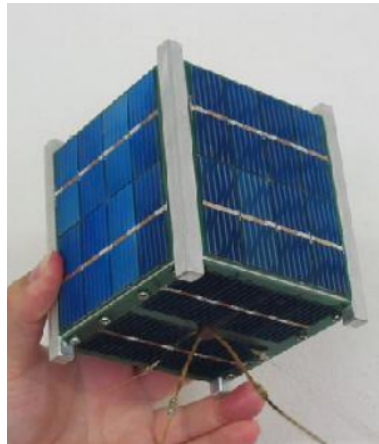


Figure 3.3: A 1U CubeSat deployed using a rail system [68]

Another option, typically used for larger CubeSats, uses two tabs to deploy the CubeSat. This method is shown in Figure 3.4. This method allows for a continuous MLI blanket around the majority of the three sides. Considering that the DST demonstrator falls on the larger side of the CubeSat spectrum, it is assumed that the DST demonstrator will be deployed using tabs.

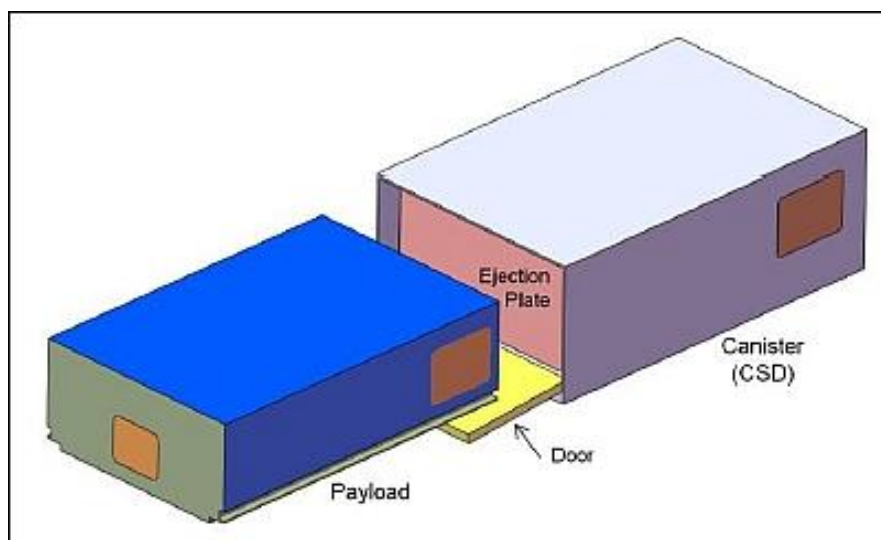


Figure 3.4: A 6U CubeSat deployment canister [26]

3.2.2. Surface coatings

To achieve thermal control of the spacecraft using only passive methods, a variety of different coatings must be applied. Certain paints are used which have different optical properties. Certain coatings have already been decided, such as Acktar ultra-black, [4], for certain components; the SMDS booms, the inside of the

baffle, the frame of the secondary mirror, and the top of the secondary mirror panel. For all other surfaces of the spacecraft, coatings have yet to be defined. Thus, several available coatings are proposed and their optical parameters are noted. All emissivity values are in the IR spectrum, while all absorptivity values are in the solar spectrum.

The Acktar ultra-black coating is used for these components as its reflectivity is low, causing less scattering of stray light inside the baffle. The emissivity value is >0.93 for wavelengths between 3 and 30 μm , and a value of 0.93 is used for the model. An absorptivity value is not given and thus it is assumed to be equal to 0.93, although it is likely slightly higher. [4]

It may be necessary to insulate the spacecraft from sunlight. This can be achieved by using Multi-Layer Insulation (MLI) blankets. The emissivity and absorptivity values of an MLI blanket depend on the number of layers. Additional layers reduce the emissivity and absorptivity, thus improving insulation performance. In the work of Arink, [40], an investigation was carried out into the effective emissivity and absorptivity to the number of layers. His findings are included in Table 3.2. It is assumed that the absorptivity and emissivity of the blanket are equal. Further increasing the number of layers was found to only marginally improve the MLI's performance, and is thus not considered further.

Coating	Emissivity	Absorptivity	Reflectivity	Reference
Acktar ultra black	0.93	0.93	0.07	[4]
Anodized black	0.88	0.88	0.12	[47]
Catalac black paint	0.96	0.88	0.12	[47]
Catalac white paint	0.9	0.24	0.76	[47]
Silver FEP tape (1 mm thick)	0.48	0.14	0.86	[62]
Silver FEP tape (10 mm thick)	0.85	0.14	0.86	[62]
YB71 White paint	0.9	0.18	0.82	[47]
Z93	0.92	0.16	0.82	[47]
Z93SC55 Conductive paint	0.94	0.14	0.86	[47]
GSFC white paint MS74	0.92	0.17	0.83	[47]
MLI (2-layer)	0.0260	0.0260	-	[40]
MLI (3-layer)	0.0212	0.0212	-	[40]
MLI (4-layer)	0.0184	0.0184	-	[40]
MLI (5-layer)	0.0164	0.0164	-	[40]
MLI (6-layer)	0.0150	0.0150	-	[40]
Solar cells	0.718	0.6	0.1	[29]
Standard OSR (CMX)	0.1	0.86	0.9	[54]

Table 3.2: A summary of potential thermal coatings

Optical Solar Reflectors (OSR) consist of a thin glass substrate, which has a rear surface coating of a highly reflective material, silver for example. The reflective layer reflects solar radiation through the glass, which is transparent in this spectral band. The outer glass surface emits radiation in the infrared band.[32] OSRs are typically used for spacecraft radiators. Typical values for the absorptivity and emissivity of an OSR are 0.1 and 0.86, respectively. [54]

Solar panels require a high absorptivity to absorb as much sunlight as possible to convert to power. This results in a (relatively) high heat load on the solar cells. The emissivity of a solar cell is also relatively high. The emissivity value that will be used is 0.718, and the absorptivity value is 0.9. [29] Since solar cells convert a fraction of incident radiation to electricity, this value should be subtracted from the absorptivity, as this does not contribute to the heat balance of the solar panels. As is discussed in Section 3.2.5, the solar panel efficiency is 30%, resulting in an (effective) absorptivity of 0.6.

The values described in this subsection are tabulated in Table 3.2. For all coatings, it is assumed that the transmittance is 0 and that the reflectivity is thus $(1 - (\text{absorptivity or emissivity}))$.

3.2.3. Propulsion system

The necessity of a propulsion system depends on the initial mission altitude. The objective is to fly at an altitude of 300 km. Depending on the results that this orbit altitude yields for the thermal analysis, it may be necessary to raise the orbit altitude to 500 km. The DST will deorbit quickly at an altitude of 300 km, in the order of weeks to a month or two, depending on the solar pressure and ballistic coefficient of the final design. [71] Therefore, the requirements of the propulsion system are analyzed for both cases, and a preliminary choice of the propulsion system is made. These system choices provide the required power consumption information which serves as power input to the thermal model.

The estimated orbit lifetime varies by a factor of 4 between the solar minimum and solar maximum, thus, an average value is taken between the two values. The ballistic coefficient, see Equation 3.11, relates to the mass of the satellite, the cross-sectional area of the satellite, and the drag coefficient of the satellite. In [59], the ballistic coefficient for various spacecraft with varying cross-sectional areas is determined. Two spacecraft, with a mass of 40 kg and a cross-sectional area of approximately 0.18 m^2 , have a ballistic coefficient of approximately 0.01. The DST is expected to have a mass of 50 kg and a cross-sectional area of 0.09 m^2 , with the baffle adding another 0.09 m^2 , and the solar array adding another 0.29 m^2 (calculated in Section 3.2.5) for a total cross-sectional area of 0.47 m^2 . [33] This is slightly more than double the cross-sectional area in [59]. However, it is assumed that it is a worst-case scenario, and thus a ballistic coefficient of double that of the reference can be used. Thus, the ballistic coefficient of $0.02 \frac{\text{m}^2}{\text{kg}}$ is used to determine the satellite decay since the cross-sectional area is double that of the reference area.

$$b = \frac{m}{C_d A} \quad (3.11)$$

The ballistic coefficient is often also displayed as the inverse ballistic coefficient:

$$\beta = \frac{1}{b} = \frac{C_d A}{m} \quad (3.12)$$

This inverse ballistic coefficient has the unit $\frac{\text{kg}}{\text{m}^2}$ and is used in reference tables, like table I-1 in [71], which shows the expected orbit lifetime for various altitudes and ballistic coefficients. With an inverse ballistic coefficient of $50 \frac{\text{kg}}{\text{m}^2}$, an altitude of 300 km, and an average taken between the solar minimum and maximum, the expected lifetime will be approximately 35 days. The required ΔV to maintain altitude for one year is then approximately 515 m/s.

Using Table I-1 again, the expected orbit lifetime is estimated for an altitude of 500 km. Using the ballistic coefficient of $50 \frac{\text{kg}}{\text{m}^2}$ and an average between solar minimum and maximum, the expected orbit lifetime for an altitude of 500 km is approximately 611.5 days. The required ΔV to maintain this altitude for one year is approximately 19.88 m/s.

The total impulse required to maintain these orbits depends on the required ΔV and the mass of the spacecraft, according to the following set of equations. Here it is assumed that the mass before and after the burn is almost the same. Then, the logarithm is approximately equal to 1, and the equations can be substituted. [73], [50]

$$\begin{aligned} \Delta V &= v_e \left(\ln \frac{m_0}{m_f} \right) \\ I_T &= m v_e \\ I_T &= \Delta V m \end{aligned} \quad (3.13)$$

For an orbit altitude of 300 km, with a required $\Delta V = 515$ and $m = 50 \text{ kg}$, this yields a required total impulse of 25750 Ns per year. Table 3.3 shows several propulsion systems for CubeSat applications. The Bit-3 RF ion thruster can support the DST demonstrator mission for at least one year. The propulsion system can deliver a ΔV up to 2390 m/s, for a spacecraft mass of 14 kg. [18] Since the total impulse does not change, this implies that this propulsion system could deliver a ΔV up to 669.2 m/s for a spacecraft mass of 50 kg. This would allow the demonstrator to fly at an altitude of 300 km for more than a year. With additional propellant, this duration can be increased.

Since this propulsion system is an electric propulsion system, it has a high power consumption. The required

input power ranges from 56 to 75 W and the thermal dissipation load is 35 W.[18] Electric propulsion systems typically produce less thrust compared to chemical propulsion systems. To determine if the BIT-3 is capable of handling the requirements, the orbital drag is calculated according to Equation 3.14.[23]

$$\frac{F_D}{m} = C_D \frac{A_{ref}}{m} \frac{1}{2} \rho v^2 \quad (3.14)$$

Where F_D is the drag force, m the mass, C_D the drag coefficient, A_{ref} the reference area, ρ the (atmospheric) density, and v the relative velocity of the atmospheric particles with respect to the spacecraft. It can be seen that the mass term cancels out. The term $C_D A_{ref}$ is equal to 1, as can be seen in Equation 3.12, where β and m are both 50. For the atmospheric density, the mean value is taken from Table I-1 from [71], and the circular velocity at 300 km is used for v . This results in a drag force of 0.582 mN. The BIT-3 propulsion system can supply up to 1.1 mN, so it is assumed that it can meet the mission requirements.

For an orbital altitude of 500 km, with a required $\Delta V = 19.88$ and $m = 50$ kg, this produces a total impulse of 994 Ns per year. Again, Table 3.3 shows potential propulsion systems which, with the exception of the BIT-3 RF ion thruster, use chemical propulsion. It can be seen that a mission duration of 3 years is attainable using the Vacco Industries - NASA lunar flashlight micro propulsion system. All other propulsion systems will not allow the spacecraft to maintain its altitude for even a year. The electric propulsion system can also easily meet the 500 km altitude mission requirements.

Now, for the two cases, a representative propulsion system has been determined. The orbit of 300 km requires an electric propulsion system. This is not the case for the orbit of 500 km. The potential propulsion systems have comparable mass and size, however, they differ significantly when comparing the thermal dissipation. The Vacco Green mono-propellant MiPS has a power draw of 15 W, whereas the BIT-3 propulsion system has a thermal dissipation of 35 W. Furthermore, the Vacco green MiPS will operate at a higher altitude, where there is less drag and more time between thruster firing. It is assumed that the power draw is 0 when the propulsion system is not firing. Since the 500 km orbit requires such infrequent firing, it can be assumed that the incidental firing of the propulsion system is negligible, resulting in the power systems' contribution to the bus dissipation being neglected.

For the 300 km orbit, the orbital drag is approximately half of the thrust of the BIT-3 propulsion system. This implies that the BIT-3 propulsion system can fire at approximately half its maximum thrust, allowing for continuous operation and a more stable thermal environment aboard the spacecraft. It is assumed that the propulsion system would continuously fire at $\frac{0.582}{1.1} = 52.9\%$ of its thrust. This would result in a continuous thermal dissipation of 18.5 W. Considering that the propellant storage is expandable and a mission duration of 5 years may be possible, the values calculated for the 300 km mission are used for the remainder of this thesis.

CubeSat Propulsion System	Dimensions	Total Impulse [Ns]	Power [W]	Total Mass [kg]	Reference
1U CubeDrive - Dawn Aerospace	1U	>850	12.5	1.41	[58]
CPOD - Vacco systems	1U	186	5	1.244	[66]
Palomar - Boeing	1U	85	5	1.063	[66]
Standard - Vacco systems	0.3-1U	250	10	0.542	[66]
PUC - AFRL Vacco	1U	595	15	0.835 (dry)	[66]
Vacco - NASA lunar flashlight MiPS (Vacco green monopropellant MiPS)	1U	3220	15	3 (dry)	[67]
BIT-3 RF ion thruster	2U	33460	35	1.4 (dry)	[18]

Table 3.3: Potential representative propulsion systems for the DST demonstrator

3.2.4. Subsystem power allocation

The power required by the various subsystems is investigated. Comparable satellites are used to determine appropriate power budgets. As was stated in section 3.1.1, the required power of the demonstrator is assumed to be 20 W. Including the propulsion system, this value reaches 38.5 W. For the thermal model, this 38.5 W does not originate in one system but is spread over multiple different systems: ADCS, CDHS, COM, the propulsion system, and EPS. Active TCS is not used.

The sources [46], [53], and [69] are used to provide reference values for the power budget. In [46], the power budget for the ADCS of an 8 kg spacecraft is shown. In [53] the power budget for a 14 kg satellite with high propulsive requirements is shown. In [69] the power budget of a 30 kg satellite with high ADCS requirements is shown. These sources are used to determine power values for the ADCS, CDHS, and COM subsystems.

ADCS

The ADCS system ensures that the spacecraft remains properly aligned with the target (in this case the Earth). Therefore, this system must function correctly and accurately. [46] assigns 6 W to the ADCS system, while [69] assigns 23 W. Since the DST demonstrator will be larger than the first spacecraft, but will not require extreme accuracy and will not make extra maneuvers after having reached steady-state, a value between these two values is chosen, at 10 W.

CDHS

The CDHS system is the "brain" of the spacecraft and controls spacecraft functioning, as well as image processing. [53] and [69] both assign 5 W to the CDHS. Considering that the DST demonstrator will require image processing, this value is doubled to 10 W.

COM

The communications system transmits the satellite's data back to Earth. [53] and [69] both assign 5 W to the communications system. Considering that the DST demonstrator will produce large amounts of data (images), this value is doubled to 10 W. Since approximately 2-3 W of the communication system is RF power, this number is actually a bit lower, around 7 W.

EPS

The EPS power consumption is a marginal value, representing the power losses throughout the system. Due to its low value, it is assumed to be negligible and is thus not included.

Payload

Considering that the payload will not be actively cooled, this value will likely be less than 1 W. Therefore, the choice is made to consider the payload power as 1 W.

Propulsion

The propulsion system power requirement has been determined in Section 3.2.3.

Subsystem	Steady-State - Power [W]	300 km orbit - Power [W]
ADCS	10	10
CDHS	10	10
COM	7	7
Payload	1	1
Propulsion	0	18.5
Total	28 (\approx 30)	46.5 (\approx 50)

Table 3.4: The distribution of power requirements for the demonstrator model

All values are shown in Table 3.4. The total power during steady-state operation is 28 W, rounded to 30 W to incorporate minor margins and uncertainty. Since the 500 km orbit assumes the propulsion systems' contribution to be negligible, its dissipation is the same as the steady-state values. For the mission at an altitude of 300 km, the dissipation is 46.5 W, rounded to 50 W. As was stated before in Section 3.1.1, a sensitivity analysis will be performed on the power draw of the spacecraft to determine the effects this has on the thermal model.

3.2.5. The solar array

The spacecraft requires power to operate, and the solar array provides this power. Therefore, the required surface area of the solar array must be determined as it may have an impact on the thermal behavior. Depending on the desired performance and permissible complexity, various options are available for the solar array. The first option is body-mounted solar panels. These solar panels are mounted directly to the spacecraft. This is

the simplest option but also causes the spacecraft to absorb more solar heat. The second option is deployable solar panels. These are more complex and result in another deployable component on the spacecraft, but the heat input on the spacecraft is greatly reduced compared to the body-mounted panels, as the conduction is nearly negligible. However, the deployable solar panels will have a radiative coupling with the spacecraft, still causing some heating. However, it is assumed that this heating is smaller in magnitude than for the body-mounted panels. The third option is sun-tracking deployable solar panels. This option utilizes solar panels that rotate during orbit, allowing them to maintain high efficiency during orbit. However, this option is more complex than "simple" deployable solar panels.

It is assumed that the spacecraft consumes 50 W, as is established in section 3.2.4, during normal operation. During an eclipse, the internal batteries must be discharged, to ensure system functionality. Their required capacity will not be calculated, but the required solar panel area will be calculated by incorporating a solar eclipse factor. For circular orbits at 300 km altitude, the eclipse loss factor is approximately 0.4. [20] Thus, the solar panels have 60% of one orbit to generate the required power. This results in $P_{req} = \frac{50}{1-0.4} = 83.33W$. The required surface area is calculated using the following equation: [30]

$$A = \frac{P_{req}}{I_0 \cos(q_i) \eta} \quad (3.15)$$

Where I_0 is the solar constant, $1366 \frac{W}{m^2}$, and η is the efficiency, which is assumed to be 30%. [38] q_i is the incidence angle, which is 0 degrees in the best case, but 45 degrees in the worst case. Unless a sun-tracking deployable solar array is used, it is assumed that this worst-case scenario should be used to calculate the required area. This results in a required surface area of $0.2876 m^2$, $\approx 0.29m^2$.

Considering that the surface area of one side of the spacecraft is assumed to be approximately $0.09 m^2$, it is assumed that body-mounted panels will not be able to provide enough power to the spacecraft, as at most only one side will be viewing the Sun straight on at any given time. Therefore, it is assumed that a deployable solar array is required to provide the required power. Since the conduction between the solar array and the spacecraft is minimal and the radiative coupling to the radiator will be nonexistent, the solar array is not included in the thermal analysis.

Batteries

Typically, the batteries are the constraining factor for the operating temperature of a spacecraft bus. Li-ion batteries are commonly used in small satellites, with approximately 2 out of every 3 pico- and nano-satellites using such batteries according to [15]. Therefore, it is assumed that the batteries will be lithium-ion.

3.2.6. Important aspects of the spacecraft bus

All inputs have been collected in this chapter. The power consumption of the individual subsystems has been determined, or assumptions have been made. At this point, it is important to distinguish between different methods of modeling the bus. While the desire for completeness of the model would lead to an individual model of each and every subsystem, the lack of knowledge regarding their dimensions and actual power consumption provides ample reason to model the bus components as one lump system. This would include the ADCS, CDHS, COM, EPS, and propulsion system.

Considering all of these components as one spacecraft bus requires that all of the components can withstand the temperature of this lumped system. To incorporate the operating temperature of the various components, a thermal budget is assumed to be representative. The operating temperature of the batteries is typically the constraining factor, and for lithium-ion batteries is from -30 to 40 ° C. [17] The proposed propulsion systems have operating temperatures of -15 to 45 ° C and 10 to 40 ° C. Thus, the operating temperature of the propulsion system is considered leading.

Specific Heat

The heat capacity of the bus must also be included in the thermal model. The heat capacity strongly influences the spacecraft's resistance to thermal changes. A high heat capacity results in slower heating and cooling of the spacecraft, ensuring a more stable thermal environment during eclipses, for example. The heat capacity strongly depends on the materials used and the mass of the materials/bus.

Due to the uncertainty regarding the in-depth design of the spacecraft bus, an accurate heat capacity is difficult to determine. It is known that the bus will consist of aluminum, PCBs, and general electronic components. To arrive at an assumption for the spacecraft's heat capacity, several approaches are combined to reach one conclusion.

The first approach will use several (smaller) satellites as reference values on which the expected value for the DST demonstrator is based. The Delfi-PQ, a 3p PocketQube, has a heat capacity of $290 \frac{J}{K}$, with a mass of 600 grams and an approximate volume of 375 cm^3 . [8] The DelFFi is a 3U CubeSat, which has a heat capacity of $2933 \frac{J}{K}$, with a mass of 3.4 kg and an approximate volume of 3000 cm^3 . [16] It can be seen that there is a factor 8 difference in the volume between the Delfi-PQ and the DelFFi, and a factor 10 difference in thermal capacity. It is assumed that this relationship holds when translating from the DelFFi to the DST demonstrator. The DST demonstrator bus has an expected volume of 16000 cm^3 . Thus, the volume difference is a factor of 5.3. Using the same ratio, this yields an approximate heat capacity of the bus of $19550 \frac{J}{K}$, or, with a mass of 25 kg, a specific heat of $782 \frac{J}{kgK}$.

The second approach will use the material distribution of a larger satellite to reach an equivalent specific heat capacity, on which the expected value of the DST demonstrator is then based. The mass distribution per material of the DART spacecraft (Double Asteroid Redirection Test, [19]) is detailed in [52]. The DART spacecraft weighs 535 kg, of which 436.57 kg in aluminum, 54.43 kg in Ti-6Al-4V alloy, 22.4 kg in stainless steel alloy, and 21.6 kg in silicon. This number for the mass includes the spacecraft bus and the solar panels. If it is assumed that the DST has the same material distribution with a mass of 25 kg, then the specific heat would also be similar. Thus, the specific heat is calculated by determining the mass fraction of each material and multiplying this by the respective specific heat of the material. The specific heat of aluminum is $900 \frac{J}{kgK}$, Ti-6Al-4V alloy is $560 \frac{J}{kgK}$, stainless steel is $500 \frac{J}{kgK}$, and for silicon is $712 \frac{J}{kgK}$. This yields an equivalent specific heat of $841 \frac{J}{kgK}$. [45], [24], [9]

The third approach is to calculate the expected weight per component of the spacecraft bus and to calculate the average specific heat. It is assumed that 15 kg of the spacecraft will consist of electronics. Electronic components have been found to have a specific heat of $690 \frac{J}{kgK}$. [45] It is assumed that the mass of the PCBs on the spacecraft will be approximately 3 kg. PCBs have a specific heat of $904 \frac{J}{kgK}$. [36] The structure of the spacecraft will be made of aluminum, with a specific heat of $900 \frac{J}{kgK}$, and its mass will be approximately 5 kg. [63] The remaining mass of 2 kg, is assumed to be aluminum as well. Using these values, this yields an effective specific heat of $774.5 \frac{J}{kgK}$.

It can be seen that three different but relatively close values have been calculated for the specific heat of the spacecraft bus. The choice is made to choose a value between these three values, which is chosen to be $800 \frac{J}{kgK}$.

3.3. Chapter Summary

In this chapter, various system inputs and design choices have been made that are necessary for the thermal model. Dimensional limits have been established by an analysis of available spacecraft buses. The detector heat load has been determined, and the method of application in the model has been discussed. The orbital parameters of the orbits under investigation have been determined. Design choices have been made on the deployment mechanism, coatings, propulsion system, subsystem power allocation, and solar array. For the deployment mechanism, the choice is made for tabs, in line with recent development for larger CubeSats. A list of coatings has been supplied that can be used for the thermal model. The potential requirements of the propulsion system have been investigated and a choice has been made for a representative propulsion system. The power allocation for each subsystem has been made, and two cases have been determined; steady-state and propulsion maneuver. The size of the solar array has been calculated, resulting in the determination that a deployable solar array is required to provide the required power. The temperature limits for the spacecraft bus have been defined and an estimate of the specific heat capacity of the spacecraft bus has been done.

Tables 3.5, and 3.6 are repeated here as they are considered the most important results. Table 3.7 shows the

choices for the various components to be modeled. Table 3.8 shows the temperature limits that are considered during the modeling.

Subsystem	Steady-State - Power [W]	Propulsion Maneuver - Power [W]
ADCS	10	10
CDHS	10	10
COM	7	7
Payload	1	1
Propulsion	0	18.5
Total	28 (\approx 30)	46.5 (\approx 50)

Table 3.5: The distribution of power requirements for the DST demonstrator model

Orbit	Semi-major axis (a) [km]	Inclination (i) [deg]	Right ascension (RAAN) [deg]
Sun-synchronous 12 PM	300 (+6371)	96.648	0
Sun-synchronous 2 PM	300 (+6371)	96.648	30
Sun-synchronous 4 PM	300 (+6371)	96.648	60
Sun-synchronous 6 PM	300 (+6371)	96.648	90
Sun-synchronous 8 PM	300 (+6371)	96.648	120
Sun-synchronous 10 PM	300 (+6371)	96.648	150
Sun-synchronous 12 AM	300 (+6371)	96.648	180

Table 3.6: The orbits that will be used to analyze the thermal environment on the spacecraft.

Component / Design Choice	How is it modeled
Payload	The components of the payload will be modeled, with adaptations for, the thermal modeling program ESATAN.
Detector	The detector will be modeled normally, with an applied heat load.
Solar array	The solar array will not be modeled.
Spacecraft bus	The spacecraft bus will be modeled as one lumped system, containing all subsystems.
Deployment Method	Tabs, not included in the thermal model.

Table 3.7: How each of the (sub)components will be modeled in the thermal model

Component	Operating Temperature	Survival Temperature	Reference
BIT-3 Electric Propulsion System	-15 to +45 ° C	-	[18]
Vacco green monopropellant MiPS	+10 to +40 ° C	-34 to +60 degree C	[67]
Lithium Ion battery	-30 to +40 ° C	-	[17]

Table 3.8: The temperature limits of the spacecraft bus

4

Model Geometry Generation

This chapter details the generation of the computer-aided design (CAD) model of the DST demonstrator. The baffle's design is further investigated, and the placement of its section is determined. The optical elements are modified for analysis using ESATAN. The design of the nadir-facing surface on which the baffle and SMDS are placed is investigated. The dimensions of the instrument box are determined. The sizing and subdivision of the bus into multiple components is elaborated. The solar array is considered to be thermally decoupled. Its influence is considered negligible and is thus not considered further. Representative sandwich panels provide sample values for the density and thermal conductivity of the spacecraft's structure. The required area for the nadir-facing surface is considered leading for the rest of the satellite's dimensions. The satellite's maximum dimensions are 34x35x36 cm, as determined in Section 3.1.1.

4.1. The baffle

The baffle is a vital component, as it reduces the stray light incident on the primary mirror, which causes interference with the image. The dimensions of the baffle have been determined in the thesis of Hu [35]. It was determined that the baffle's length should be 8 cm greater than the top of the secondary mirror. This yields a length of 33 cm. Since the baffle must also be deployed, the choice is made to segment the baffle into three sections. Each section's interior is coated with Acktar ultra-black paint, which minimizes thermal self-emission due to its high absorptivity. The exterior is covered in 2-layer MLI. This likely requires the MLI to bend. Arink investigated the foldability of various MLI thicknesses. [40] He determined, for the 1.5 m VIS DST, that it was possible to fold MLI once (or multiple times, but this greatly increases the packing thickness). Thus, it is assumed that this holds for the DST demonstrator.

The thickness of the MLI and the Acktar ultra-black coating is 0.506 mm. [35] Assuming that the wall thickness of each baffle segment is 3 mm, this yields a total thickness per segment of 3.506 mm, rounded up to 3.6 mm. The base ring of the baffle is mounted on the edge of the nadir-facing surface. The second and third rings of the baffle can then use the excess envelope, which is assumed to be approximately 1 cm, comparable to other CubeSat envelopes. [27] This is necessary, as these design choices leave a space of 2.14 cm between the mirror's edge and the inner edge of the baffle. A minimum of 2 cm is necessary to accommodate the SMDS legs. Contact between the legs and the baffle should be avoided. Therefore, the legs are placed directly adjacent to the mirrors' edge, leaving a margin of 1.4 mm between the legs and the baffle's interior.

The total length of the baffle is 33 cm in the deployed configuration. The baffle is expected to be divided into three segments with heights of 12, 12, and 11 cm. The first two segments are 1 cm longer than the last to allow for overlap between the sections. This results in an effective length of each baffle section of 11 cm when viewed from the outside. The height of the baffle is thus 12 cm in the stowed configuration. This leaves 0.22 m in the "height" dimension. It is assumed that the top of the baffle does not use the envelope (only the sides).

The design of the baffle is shown in Figure 4.1. It can be seen that the baffle is constructed of three concentric pieces, 12, 12, and 11 cm high. Due to the overlap, the total height is 33 cm. The outer diameter of the first section is 350 mm. The inner diameter of the second section is also 350 mm and the outer diameter is 357.012 mm. The third section has an inner and outer diameter of 357.012 and 364.024 mm, respectively.

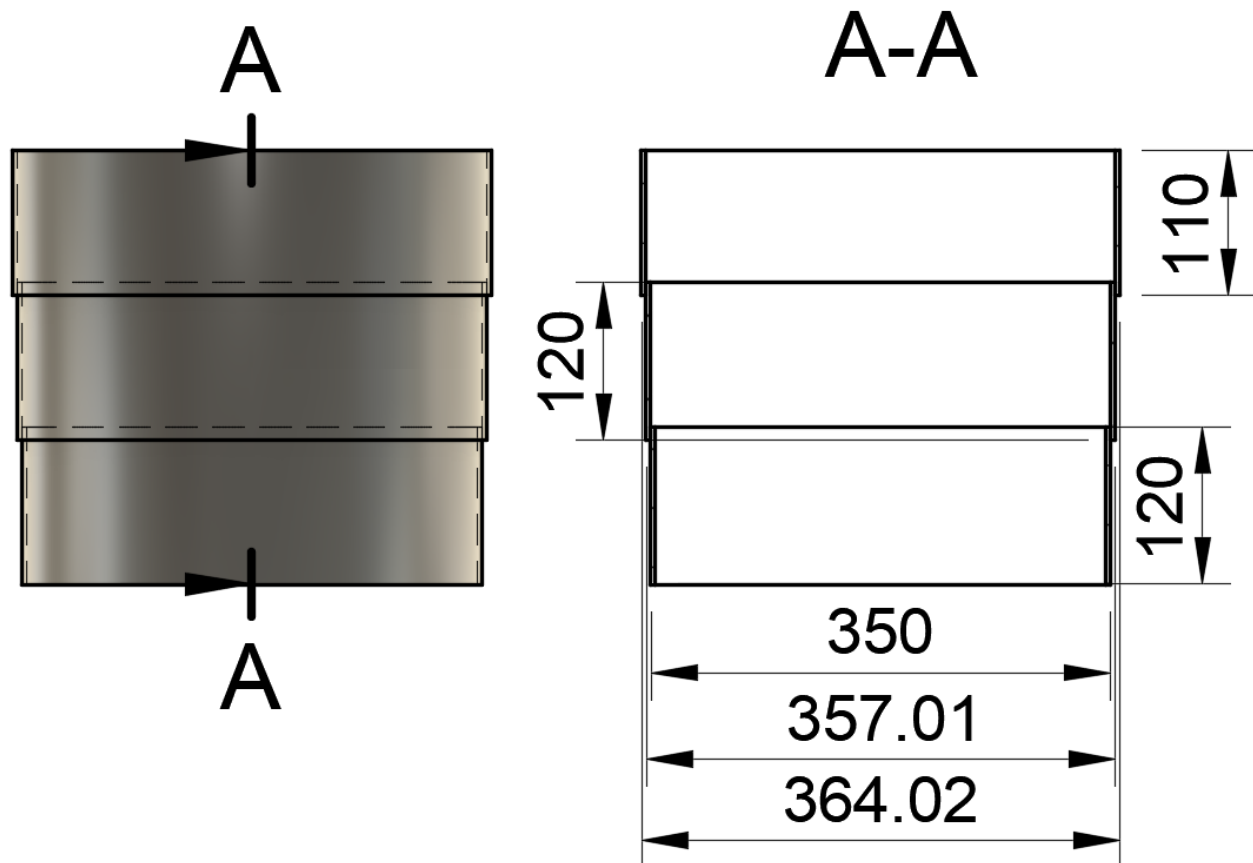


Figure 4.1: The design of the baffle with its dimensions, on the right a section view of the baffle

Baffle Segments and Insulation

As is visible in this section, the baffle's dimensions are close to the allowable limits for a 27U CubeSat. At this point, it can be said that the baffle has become the main design driver for the DST demonstrator. Choices may be made for more baffle segments to increase available bus space or leave more clearance around the mirror. However, the baffle is not the main objective of this thesis, and thus further investigation is not done. An analysis of the baffle's potential coating and MLI arrangement is done in Section 6.6. The main reason for the small clearance is the MLI. It is assumed that the baffle will essentially be thin shells on which the coating(s) are applied. MLI is thicker than other coatings like paint or an OSR. Although applying an OSR may yield other problems with deployment, it may allow gains in other areas.

4.2. The optics

The optical chain can be seen in Figure 4.2. The optical chain functions as the cornerstone of the design. The optical chain consists of 3 mirrors, 3 optical components, and the detector. The third mirror, optical components, and detector reside in the instrument box. The M1 has a diameter of 0.3 m. The curvature of the M1 is 17 mm, and the thickness is assumed to be 1 cm. This yields a mirror height of 2.7 cm, rounded to 3 cm. Furthermore, while it would be optimal to model the entire optical chain in ESATAN as they have been designed, due to the way the CAD converter (CADbench) works, this yields a geometry that functions poorly. The M1 and M2, as well as the optical elements all consist of curved sections, which CADbench, and by extension ESATAN, cannot handle. Therefore, the optical path will not be modeled. Instead, the mirrors are simplified and certain optical elements are removed.

The M1 is changed from its appearance in Figure 4.2 to a simple flat disc. The hole in the center is also removed. The heat that would otherwise enter the instrument box is accounted for by the detector and filter heat loads, calculated in Section 3.1.2. Furthermore, M2 is also replaced by a disc for the same reasons as M1. The optical elements inside the instrument box are all removed, as they also consist of many triangular

elements when converted. The detector is replaced by a disc with a diameter of 1 cm and a thickness of 5 mm. The filter is included in the instrument box as a disc with a radius of 2 cm and a thickness of 5 mm. The detector and filter heat loads are modeled as total volume heat loads.

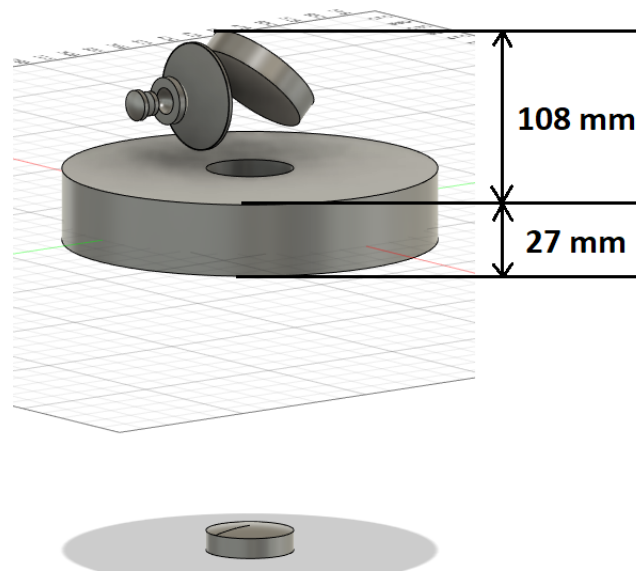


Figure 4.2: The CAD design of the optics, the primary mirror thickness is not to scale

4.3. Nadir-Facing surface

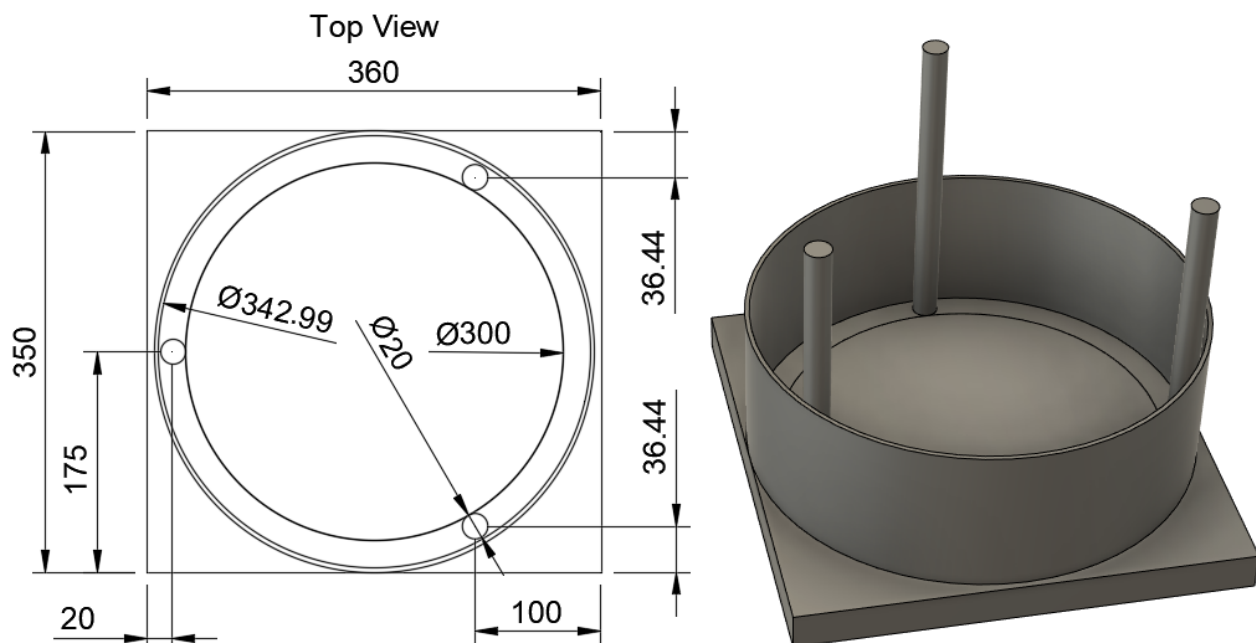


Figure 4.3: The CAD design of the nadir-facing surface, with an isometric view of the components shown in the drawing, with the top two baffle sections removed

The Nadir-facing surface carries the primary mirror, the M2 deployment mechanism, and the deployable baffle. Since the mirror's diameter is 30 cm, this leaves little room for the other components. Therefore, the choice is made to use the maximum dimensions, 35x36 cm, for the nadir-facing surface. On this surface, the center point of the mirror is located on the center of the rectangular surface. This leaves 2.5 cm available space

at each edge for the baffle and SMDS legs in one direction and 3cm in the other. The 2.5 cm direction is considered leading in this case.

The legs of the secondary mirror deployment system (SMDS) will be modeled as rods with a diameter of 2 cm, as determined by Hobijn [33]. The available space between the mirror and the baffle is 2.14 cm. The choice is made to place the legs directly on the edge of the mirror. This leaves 0.14 cm between the inner edge of the baffle and the SMDS legs. The legs will be mounted on the nadir-facing surface with a standoff. This standoff is approximately 1.5 cm wide, leaving a small margin. The legs of the SMDS are placed with an angle of 120° in between the inner diameter of the baffle and the outer diameter of the mirror. The nadir-facing surface is given a thickness equal to the mirror thickness, 3 cm. This leaves 0.19 m of available space below the nadir-facing surface where the instrument box and the bus are housed. The nadir-facing surface is assumed to be made of aluminum.

A technical drawing of the nadir-facing surface with the bottom baffle segment and each of the SMDS legs is shown in Figure 4.3. An isometric view is added that displays all the components shown in the drawing.

4.4. Instrument Box

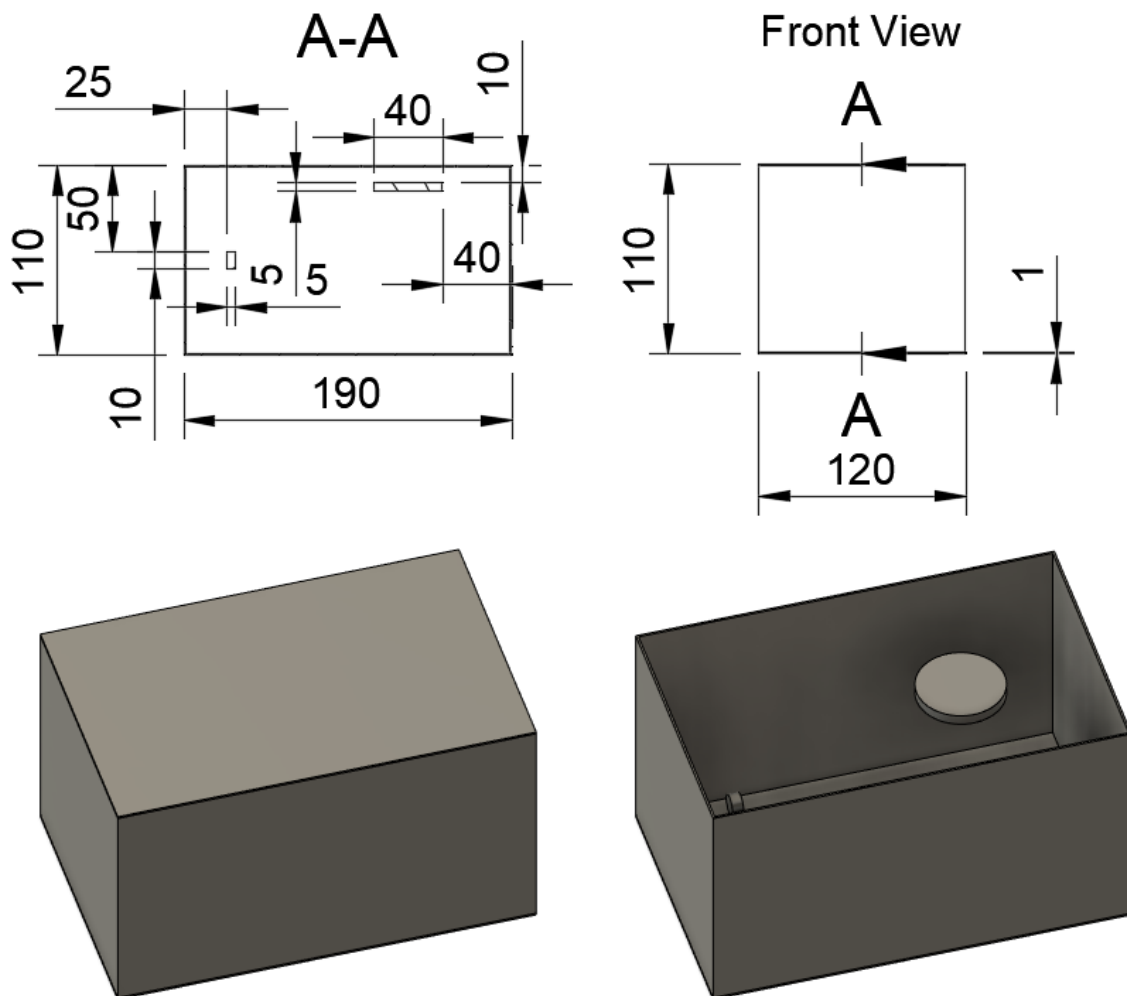


Figure 4.4: The CAD design of the instrument box, with an isometric view of the closed box and the top surface removed showing the two optical elements

The instrument box is designed such that there is available space for future changes to its design. The wall thickness influences the thermal behavior of the instrument box strongly. For the optics, it is of utmost im-

portance that the walls of the instrument box are uniform in temperature. If there is a temperature gradient in the instrument box walls, the instruments will suffer adverse effects from thermal expansion. Therefore, the instrument dimensions are taken at a distance of 1 cm from the internal optical components. If there is a need to increase the wall thickness, it can be done without any impact on the internal optics. The instrument box's external dimensions are a height of 11 cm, a width of 12 cm, and a length of 19 cm. In Figure 4.4, the instrument box is shown schematically with a wall thickness of 1 mm.

The components surrounding the instrument box (primarily the bus) have a much higher heat generation than the heat input on the components in the instrument box. This results in a much higher equilibrium temperature of the instrument housing if not managed. The bus is covered in MLI such that the instrument box is isolated from the heat generated by the bus. The instrument box is assumed to be constructed of aluminum.

4.5. The Bus

The bus is allocated all of the remaining space, which will not be used by the instrument box, the sandwich panels, or the nadir-facing surface. This yields a rectangle with dimensions of 0.34x0.18x0.32 cm. A hole is made in the bus to accommodate the instrument box, which has dimensions of 14x13.1x23.4 cm. A 1 cm margin is left between the radiator panel and the bus's sides. This is done to eliminate any conduction to the radiator panel and to allow for optical coatings or insulation to be applied. This will be done on the radiator panel inside and the bus surfaces. This yields a bus volume of 0.016152 m³, or 16.152 U.

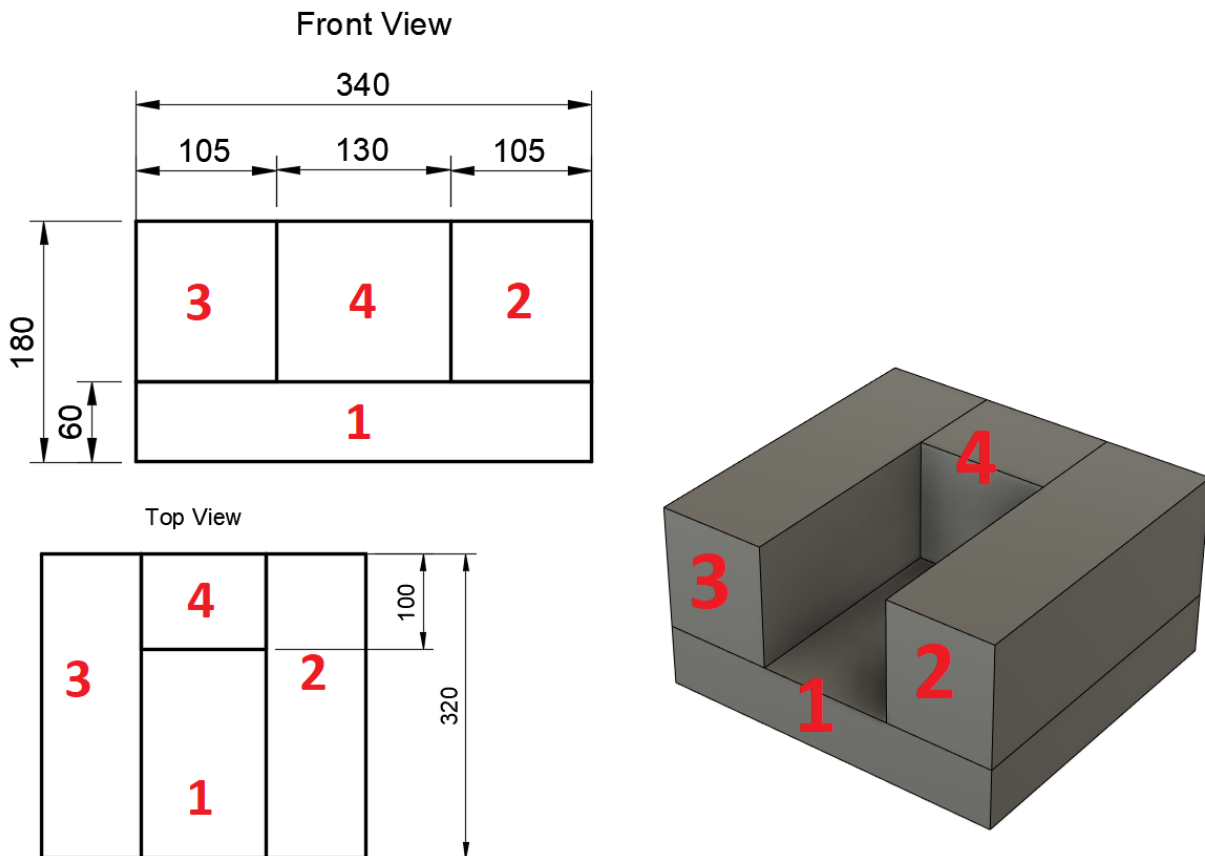


Figure 4.5: The CAD design of the bus, with labeled subdivisions

The design of the bus can be seen in Figure 4.5. It can be seen that the bus is divided into four parts. This is done because the geometry generation function of ESATAN does not allow the subtraction of solids. The dimensions of the first bus subdivision are 0.34x0.32x0.06 m for a volume of 6.528 U. The dimensions of the second and third bus subdivisions are identical and are 0.105x0.32x0.12 m, for a volume of 4.032 U each. The

dimensions of the fourth bus subdivision are 0.13x0.1x0.12 m, for a volume of 1.56 U. The thermal analysis will apply the heat load proportionally across each subdivision based on their respective percentages. For subdivision 1 this is 40 %, for subdivisions 2 and 3 this is 25 % each, and 10 % for subdivision 4.

4.6. CubeSat Structure

The primary requirement of the CubeSat structure is to provide stiffness to the spacecraft. There are various methods for the design of a CubeSat structure. Smaller CubeSats (1U - 8U) can have their stiffness requirements fulfilled by their thin-walled box design. Larger CubeSats (12U or larger) may need a dedicated structure, such as a beam frame supported by thin-walled plates or by using sandwich panels. [63] Sandwich panels consist of two thin aluminum sheets that contain an aluminum honeycomb "sandwiched" in between. By raising one of the aluminum sheets, the sandwich panel provides much greater bending strength and stiffness relative to its mass. [41] Figure 4.6 shows a sandwich panel with a honeycomb core.

The structure's stiffness requirements are derived from the launch vehicles' longitudinal and lateral frequencies during launch. The Ariane 5 and the Falcon 9 launch vehicles have a lateral and longitudinal frequency requirement of 10 and 31/25 Hz respectively. [7], [64] Which of these frequency requirements applies to the DST depends on the launch configuration, as it is expected that the DST will not be the primary spacecraft, but will "ride-share."

The structural design requires an in-depth simulation to determine the actual frequency response. Due to the current design knowledge, such a simulation is currently impossible. Therefore, the assumption is made that sandwich panels will be used. It is assumed that panels with a face-sheet thickness of 1 mm and a total thickness of 10 mm will provide sufficient stiffness to the DST demonstrator. The Larcore panels from Alucoil, [5], are used as reference values. They provide a density of $519 \frac{kg}{m^3}$ and a thermal resistance of $0.0074 \frac{m^2 K}{W}$, or a thermal conductivity of $1.35 \frac{W}{m K}$. The specific heat ($\frac{J}{kg K}$) value will be the same as normal aluminum, as the lower density compensates for the honeycomb section. The total structural mass will amount to approximately 4 kg. There are 5 panels on the DST, the zenith panel, side panels 1-3, and side panel R, which is the side panel that shares a side with the radiator.

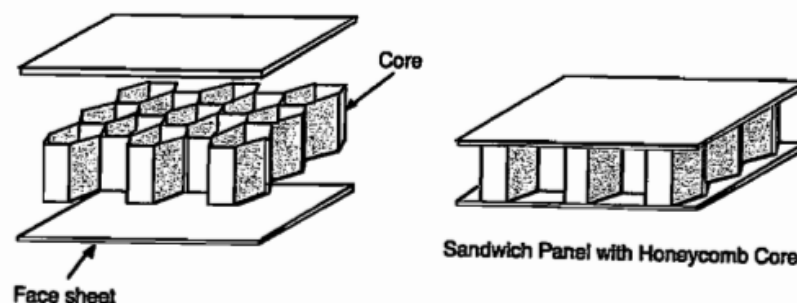


Figure 4.6: A depiction of a sandwich panel, taken from [41]

4.7. The Solar Array

The required surface area of the solar array was determined in Section 3.2.5. For the thermal model of the spacecraft, it is assumed that they are conductively decoupled from the spacecraft. Furthermore, the radiative influence of the solar panels will have a minimal contribution to the spacecraft's temperatures. For this reason, they are left out of consideration for the analysis. Thus, they are not included in the (thermal) model.

4.8. Chapter Summary

In this section, the components of the DST demonstrator have been designed. The baffle is constructed in three segments, 12, 12, and 11 cm long. With a 1 cm overlap between the sections, the total baffle length is 33 cm, 8 cm higher than the top of the secondary mirror. Each baffle section has a thickness of 3.506 mm. The baffle's bottom section has an outer diameter equal to the minimum dimension of the 27U CubeSat, 35

cm. The outer diameter of the top section is 364.024 mm. The baffle sections are coated with 2-layer MLI on the outside and Acktar ultra-black paint on the inside.

The baffle is mounted on the nadir-facing surface. The dimensions of the nadir-facing surface are 35x36 cm. The primary mirror is centered on this rectangular area and has a diameter of 30 cm. This leaves 2.5 cm to the edge in one direction and 3 cm in the other. The bottom section of the baffle reduces the available space to 2.14 cm. The SMDS legs have a diameter of 2 cm. They are placed directly adjacent to the mirror's edge to prevent interference. The SMDS legs have a length of 25 cm, equal to the height at the top of the M2. The legs are placed symmetrically, all at 120° seen from the center.

The optical chain has been simplified. The M1 and M2 are replaced by circular disks. This is done because the analysis program cannot handle curvatures well. The optical elements inside the instrument housing are removed and replaced by two disks, the detector, and the filter. The detector is the primary focus of the thermal analysis, loaded by a heat input that represents the thermal load. The filter represents the heat input into the instrument box due to visual light.

The instrument box has a height of 11 cm, a width of 12 cm, and a length of 19 cm. Its wall thickness at this point of the thesis is 1 mm. The thermal analysis will show whether an increase in the wall thickness is required to ensure thermal stability.

The structural needs of the DST demonstrator can not be determined accurately at this point. Thus, it is assumed that the sandwich panels are sufficiently stiff. Commercial sandwich panels provide reference values for the density and conductivity.

The bus encompasses all space below the nadir-facing surface and between the side panels. A margin of 1 cm is left between the radiator panel and the bus to allow for surface coating or internal MLI placement. The bus also has a margin of 5 mm to the instrument box for the same reason. The bus is subdivided into four components, as ESATAN does not allow cuts in solids.

Figures 4.7 and 4.8 show the CAD model and a section view of the CAD model of the DST demonstrator. It can be seen that there is a clearance between the bus and the radiator panel, and the bus and the instrument box. The optics inside the instrument box are also "hanging" in the air. The fixture of these components to the instrument box and of the instrument box to the other components will not be modeled by geometry but by a conductive coupling in the thermal analysis program.

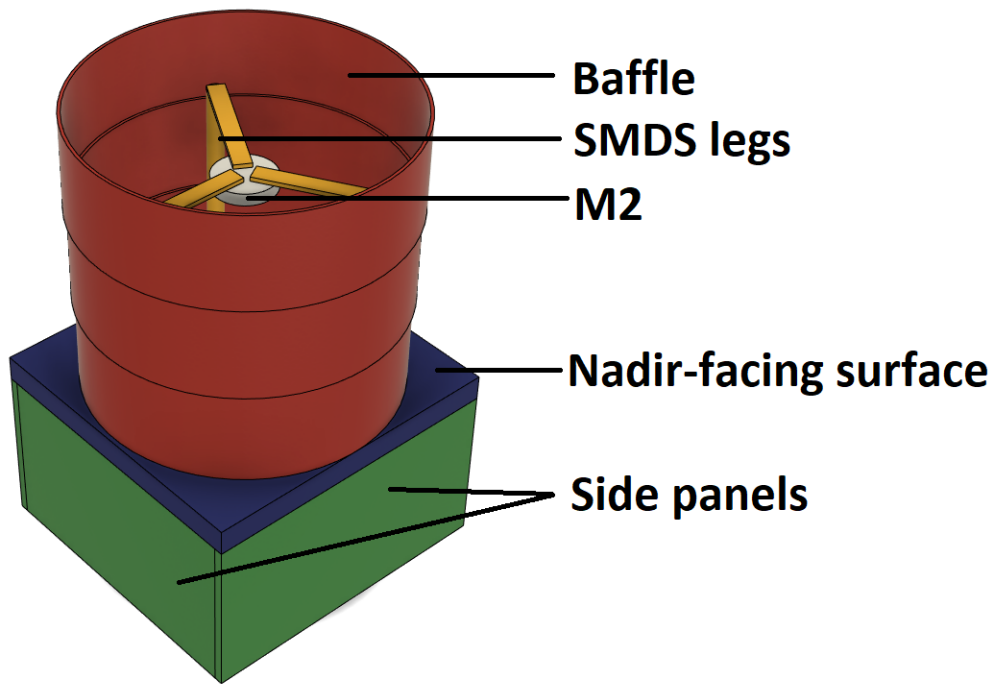


Figure 4.7: The CAD model of the DST demonstrator

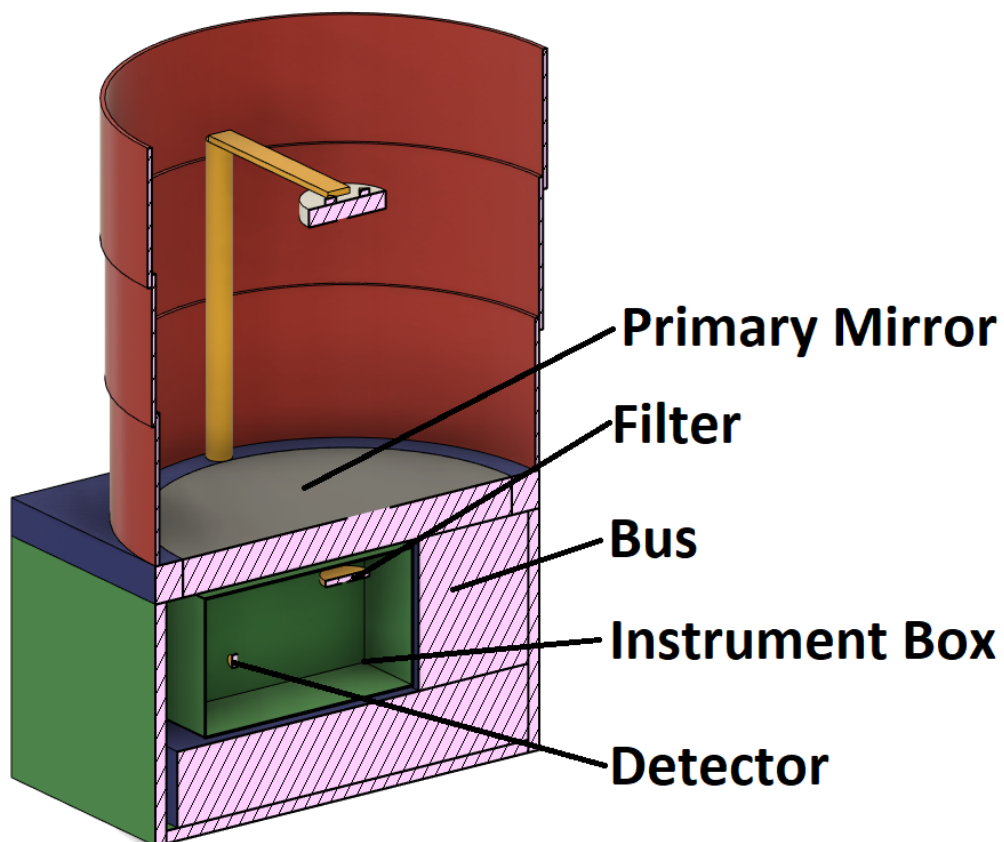


Figure 4.8: A section view of the DST demonstrator CAD model

5

The Thermal Model and Analysis

In this section, the design of the radiator and optimizations to reduce its heat inputs are detailed. The thermal model bulk materials and coatings are defined. The model assumptions are investigated, and it is determined that the radiator must be divided into two separate stages. The conductive interfaces and conductive couplings are determined. The radiative and analysis case definition is elucidated, and some of the important settings are discussed. The initial thermal model is analyzed and found to not meet the required detector and instrument box temperatures of 150 K and 200 K, respectively. The external heat input from the Earth and the Sun is reduced by the addition of the Earth shade door. The external heat input is further reduced, by adding side covers to the Earth shade door. A portion of the radiator side (R-side) is completely occulted by the Earth shade door, therefore an investigation into the potential temperatures of the R-side is done, assuming only external heat input. This results in the final design of the cryo- and cold-stage radiators, and the R-side as a whole.

The radiator design is investigated in several steps. The first step is an initial sizing of the radiator. The initial sizing is based on the expected internal heat loads, excluding external heat input from the Earth and the sun. Next, the incoming external heat loads are investigated. These heat loads result in much higher radiator temperatures than the initial radiator design. Subsequently, the reduction of the external heat flow is investigated, using an Earth shade door. The Earth shade door creates an optimization case, where a specific area of the radiator side is nearly completely occulted. This analysis then leads to a redesign of the radiator area. Following this redesign, the final radiator area is determined.

- Initial sizing of the radiator
- Analysis of the incoming internal and external heat flow
- Reduction of incoming external heat flow
- Analysis of potential ideal radiator surface area
- Redesign of radiator surface area
- Final radiator design

5.1. Thermal Model Bulk Materials and Coatings

Table 5.2 shows the materials and coatings used for each component. The density, specific heat, and conductivity are taken from the references specified in Tables 5.2 and 5.3. The value for the specific heat of "BusMat" is calculated in Section 4.5. The conductivity is assumed to be the average of the conductivity of aluminum and PCB, rounded down. These values are $247 \frac{W}{mK}$ and $80 \frac{W}{mK}$, which is averaged and rounded down to $100 \frac{W}{mK}$. The density is calculated by dividing the bus mass by the available volume. As was determined in Section 4.6, the mass of the sandwich panels will be 4 kg. The solar panels are expected to weigh approximately 1-1.5 kg. Thus, it is assumed that the bus itself will have a mass of 19 kg. With a volume of $0.016152 m^3$, this yields a density of $1176.3 \frac{kg}{m^3}$, rounded to $1180 \frac{kg}{m^3}$.

The aluminum honeycomb panels are represented as one singular panel. The bulk material properties have been established in Section 4.6. The values that will be used in the model are a density of $519 \frac{kg}{m^3}$ and a thermal conductivity of $1.35 \frac{W}{mK}$. The specific heat ($\frac{J}{kgK}$) value will be the same as normal aluminum, as the lower density compensates for the honeycomb section.

The optical elements in the instrument box are modeled as optical glass. There is a wide variety of possible density, specific heat, and conductivity values. Thus, an average value will be used. The data is taken from [60]. This yields a density of $4000 \frac{kg}{m^3}$, a specific heat of $450 \frac{J}{kgK}$, and a conductivity of $1 \frac{W}{mK}$. The detector will be coupled to the radiator with a thermal strap. The heat input to the detector will be modeled as a separate heat input, as was specified in Section 3.1.2. The decision is made to make the emissivity and absorptivity of the filter equal to 1, with a coating called "optical element". The detector will have an emissivity and absorptivity of 0, as the enclosure heat load has already been included in the detector heat load.

The instrument box is coated internally with Acktar ultra-black coating. This is done to prevent any stray light reflectance inside the instrument box, that might negatively affect detector performance. The outer surface of the instrument box is still considered "TBD". All components marked with a "TBD" in the coatings column are components for which the coating must be determined. This will be done by an iterative modeling process in this and the following sections, as different cases are examined.

Component	Material	Coating(s)	Origin
M1	Boostec SiC	Protected Silver	[70], section 6.1.2
M2	Boostec SiC	Protected Silver	[70], section 6.1.2
Filter	Optical Glass	Optical Element	Section 5.1
Detector	Optical Glass	Optical Element	Section 5.1
Baffle	CFRP	Inner surface: Acktar ultra black Outer surface: 2-layer MLI	[35], Section 8.5.1
Bus	BusMat	TBD	Section 4.5
Instrument box	Aluminum	Inner surfaces: Acktar ultra black Outer surfaces: TBD	Sections 4.4, 5.1
Nadir facing surface	Aluminum	TBD	Section 4.3
Radiator	Aluminium	TBD	Section 4.6
Side panel R	AluHoneycomb	TBD	Section 4.6
Side panel 1	AluHoneycomb	TBD	Section 4.6
Side panel 2	AluHoneycomb	TBD	Section 4.6
Side panel 3	AluHoneycomb	TBD	Section 4.6
Zenith panel	AluHoneycomb	TBD	Section 4.6
SMDS legs	CFRP	Acktar ultra black	[33], Section 6.3
SMDS spider	CFRP	Acktar ultra black	[33], Section 6.3

Table 5.1: The different components of the spacecraft and their corresponding materials and coatings.

Material	Density	Specific Heat	Conductivity	Reference
Boostec SiC	3100	750	120	[37]
Optical Glass	4000	450	1	[60]
CFRP	1820	800	24	[43]
BusMat	1023.6	800	100	Section 4.5
Aluminum	2700	900	247	[45]
AluHoneycomb	1080	900	1.188	[48]

Table 5.2: The materials and their accompanying properties in ESATAN-TMS

Coating	Emissivity (IR)	Absorptivity (Solar)	Reference
Optical Element	1	1	Assumption, see text
Detector Coating	0	0	Assumption, see text
Protected Silver	0.02	0.02	[70]
2-layer MLI	0.0260	0.0260	[40]
Acktar Ultra Black	0.93	0.93	[4]

Table 5.3: The "known" coatings

5.1.1. Modeling of the MLI

The MLI of the baffle is modeled using a shell. The shell consists of two surfaces, both of which have the optical coating "Kapton Foil 0.08" applied to them, which has an emissivity and absorptivity of 0.24 and 0.23, respectively. The bulk material of the MLI is set using a dual-material model. Both surfaces are assigned bulk MLI values, with a thickness of 0.5 mm. The bulk MLI has a density of $146 \frac{kg}{m^3}$, $1117.5 \frac{J}{kgK}$, and a conductivity of $0.1275 \frac{W}{mK}$, as calculated by Arink, [40]. The isolative behavior of the MLI is represented by the emittance and the conductance. The emittance represents the effective emissivity, whereas the conductance represents the cross-conductance, caused by the spacers. The MLI is modeled as a separate surface above the component it covers.

5.2. Model Assumptions

The thermal model contains several assumptions that must be elucidated. Most of these assumptions relate to the conductive heat transfer between bodies. The conductive heat transfer can cause significant heat inputs, depending on the materials used. The most important conductors are the detector and instrument box mounting equipment. The instrument box is mounted inside the spacecraft, and the detector is mounted inside the instrument box. This results in conduction between said components. Since a final design for the instrument box and the internal arrangement of the spacecraft is not available, a rough calculation will be done to determine the conductor values for the detector and instrument box mounting.

The materials used for mounting the components must have a low conductivity but high stiffness. ESATAN requires the user to specify multiple parameters to define a "user-defined conductor" (UDC). The conduction, $\frac{W}{mK}$, the cross-sectional area, m^2 , and the path length, m , must be defined. Alternatively, the conduction and the shape factor, m , or just the conductor, $\frac{W}{K}$, can be defined. The conductor replaces the terms $\frac{kA}{x}$ in Equation 1.3.

To quantify the conductor, several materials will be investigated. The material choices that will be examined are steel for its high stiffness, titanium for its much lower conduction while maintaining high stiffness, and G10 fiberglass for its very low conduction.[13] The detector and instrument box mounting equipment is assumed to be rectangular in the majority of its length. Therefore, it is assumed that they compare to leaf springs in appearance. A simple calculation to compare effective stiffnesses will be used to determine what is lost in stiffness to achieve low thermal conduction. The comparison will be made over leaf springs dimensions of 2 mm thickness, 1 cm width, and 5 cm length. A representative stiffness, EI is determined that represents the multiplication of the Youngs modulus and the moment of inertia. This results in the values shown in Table 5.4. The temperature difference is calculated for an assumed instrument box temperature of 200 K and a detector temperature of 80 K.

Material	Youngs Modulus [GPa]	Conductivity [$\frac{W}{mK}$]	Conductor [$\frac{W}{K}$]	EI	Conduction for $dT = 120$ K [W]
Steel	210	45	0.018	1.4	2.16
Titanium	120	11.4	0.00456	0.8	0.5472
G10 Fiberglass	16.5	0.288	0.0001152	0.11	0.013824

Table 5.4: A comparison of the conductivity and stiffness of detector mounting material

As can be seen, titanium is a better choice than steel, as the stiffness is less than half as low, while the conduction is one-quarter that of steel. Using G10 fiberglass results in much lower conduction to the detector. However, it is also much less stiff. Considering that the equivalent stiffness of the fiberglass is approximately seven times lower and the conductor is almost 40 times lower, it is apparent that fiberglass is the superior option. Should it be necessary to increase the thickness to account for launch loads, this can be done while maintaining very little conduction. While the effective stiffness is lower, it is assumed that the detector causes almost no load and that this leaf spring can support this easily. The clearance between the instrument box and the nadir-facing surface is smaller. Therefore, for the length a value of 1 cm is used. This provides a conductor value of $0.000576 \frac{W}{K}$. The instrument box is assumed to be mounted to the nadir-facing surface using 2 separate conductors, as well as the bus with 2 separate conductors. The detector is mounted to the instrument box using one conductor. The conductors and their values have also been tabulated in Table 5.5.

The conductive coupling between the radiator and the spacecraft would ideally be omitted, but this is impossible as the radiator must be mounted to the spacecraft somehow. To determine the conductive coupling, the same method as before is used. First off, it is assumed that the mounting bracket(s) will be made of G10 fiber-glass epoxy, with a conductivity of $0.288 \frac{W}{mK}$. [13] The bolts/nuts are assumed to be made of polyether ether ketone (PEEK), with a conductivity of $0.25 \frac{W}{mK}$. [74] It is assumed that the conductivity of the bracket-bolt system can be considered as a parallel arrangement, such that the total conductivity is $0.538 \frac{W}{mK}$. Assuming then that the bracket is 3 mm thick, 1 cm wide, and has a total path length of 6 cm. This yields a conductor of $0.000269 \frac{W}{K}$. The assumption is that two brackets are sufficient to securely mount the radiator, ensuring stability. These conductors will be applied to both radiator panels.

5.3. Initial Radiator Sizing and Design

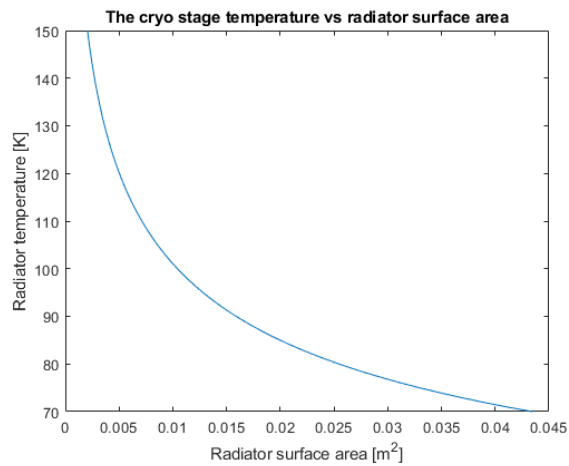
The initial thermal model will perform the first analysis of the DST demonstrator. In the previous sections, the estimated heat load on the detector and the filter has been determined. The initial size and design for the radiator are detailed, which will be used in the analysis. The most important aspect of the radiator's design is that the radiator is as thermally isolated as possible from the other components of the spacecraft. The inside surface of the radiator will be coated in MLI with an effective emissivity and absorptivity of 0.01.

The initial radiator design will be divided into two stages. A high-conductivity thermal strap will connect the detector to the cryo stage. The cold stage will be attached to the instrument box with a high-conductivity thermal strap. The thermal straps will ensure high heat flow from the components to the radiators.

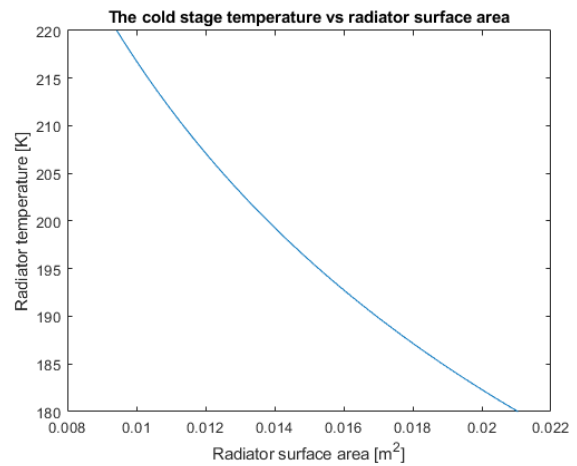
The cryo stages' initial dimensions are calculated using Equation 1.6. The emissivity is 0.93, and the heat input is 0.02 W (heat load) + 0.013824 W (conduction from the instrument box) for a total of 0.033824 W. To account for the calculation inaccuracies and assumptions, this value is rounded up to 0.04 W. It is important to note that this value will not be used in the simulations. The value that will be used in the simulations is the detector heat load as calculated in Section 3.1.2, 0.02 W. This results in the graph seen in Figure 5.1a. It should be noted that these results exclude any heat input from the earth or sunlight.

The cold stages' initial dimensions are again calculated using Equation 1.6. The heat input by conduction is calculated similarly as before, except that the nadir-facing surface is expected to be around 270 K. This results in a conductive heat load of $4 \cdot 0.000576 \cdot 70 W$, or 0.16128, rounded up to 0.165 W. The radiative heat load on the instrument box is estimated using Equation 1.6. The surface area of the instrument box is 4 panels of 19 by 10 cm, and 2 panels of 10 by 10 cm, for a total surface area of $0.096 m^2$. The temperatures of the surroundings and the instrument box are assumed to be 270 and 200 K, respectively. The emissivity of the surroundings is a mixture of 0.03 emissivity 425-3m tape, 0.01 emissivity MLI, and 0.93 emissivity white paint. Considering that a significant amount of reflection takes place inside the internal space of the spacecraft, a value of 0.05 is used for the emissivity. This results in a radiative heat load of 1.01 W, rounded to 1 W. This yields a total heat load of 1.165 W for the instrument box. This results in the graph seen in Figure 5.1b. Again, these results exclude any heat input from the earth or sunlight.

The surface area available on the side panel is $0.36 \cdot 0.19 = 0.0684 m^2$. As can be seen in Figure 5.1a, the 80 K desired temperature requires a surface area of approximately $0.02 m^2$. This will be the initial cryo stage radiator size. It is placed in the top-center location on the R-side panel, as it is assumed that this is the optimal location to reduce external heat input. Its initial dimensions are 20 by 10 cm. For the cold stage, it can be seen that the 200 K can be achieved using a radiator surface area of $0.014 m^2$. Increasing the surface area reduces the temperature further. For the initial case, the cold stage radiator area is also taken to be $0.02 m^2$, which would theoretically achieve a temperature of approximately 185 K. In the following sections, the initial analysis will be performed, and the improvements in the radiator's design are investigated, as described in the road map at the beginning of this section. Since the external heat input has not been accounted for in this analysis, its influence and mitigation of its influence are imperative.



(a) The cryo stage radiator temperature plotted against the surface area



(b) The cold stage radiator temperature plotted against the surface area

Figure 5.1: The cryo and cold stage radiator temperatures plotted against the surface area

Since the cryo stage occupies the "central" 20 by 10 cm rectangle, the decision is made to design the cold stage surrounding the cryo stage. This results in a slight increase of the surface area to 0.22 m^2 . This leaves a sliver of the R-side panel on the left and right sides of the cold stage radiator. The initial design can be seen in Figure 5.2. The yellow panels surrounding the radiator will be referred to as the "R-side" panel(s), short for radiator side panel(s).

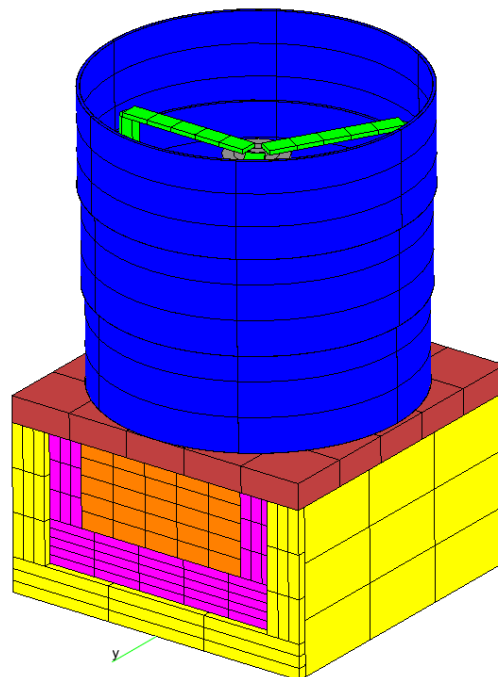


Figure 5.2: The geometry of the DST in ESATAN

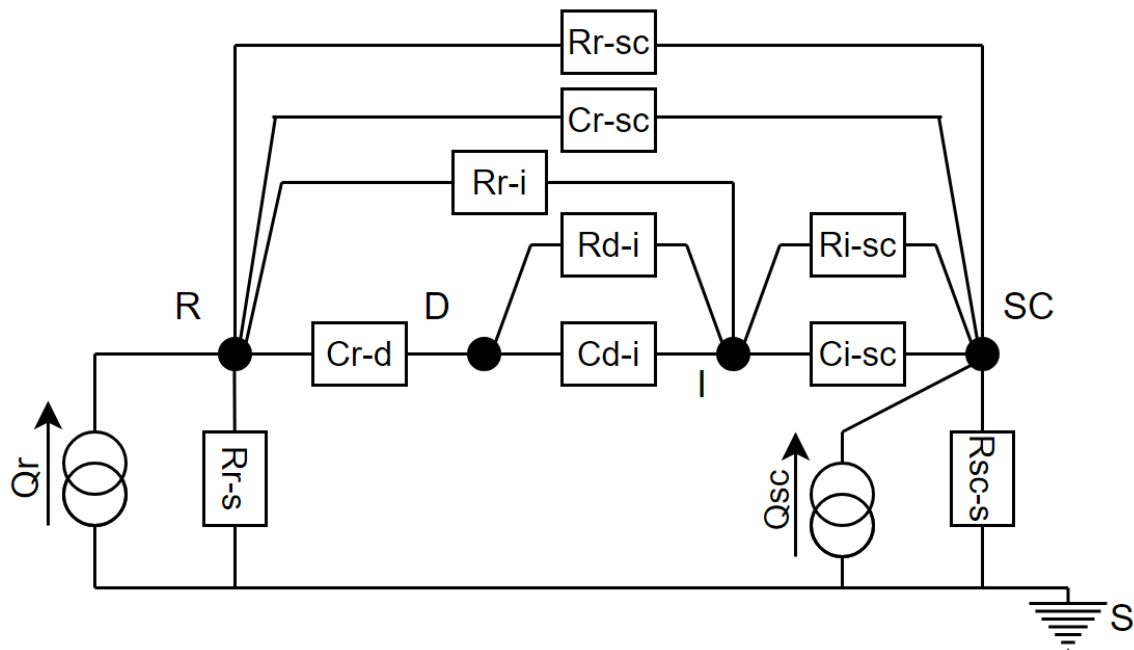


Figure 5.3: Simplified thermal network diagram of the DST demonstrator

Figure 5.3 shows the thermal network diagram of the DST demonstrator. The nodes represent the components. Node R represents the radiator, D the detector, I the instrument box, SC all the other parts of the spacecraft, and S represents space or the environment. All rectangles represent thermal couplings. Couplings with an R represent radiative couplings, and couplings with a C represent conductive couplings. Coupling Cr-d represents the conductive coupling between the radiator and the detector. Coupling Rr-sc represents the radiative coupling between the radiator panel and the spacecraft components (the bus, side panels, and nadir-facing surface).

5.4. Conductive interfaces and conductors

After the geometry has been constructed, the conductive interfaces between the different components allow for conductive heat transfer over said interfaces. ESATAN provides the user with a simple function that allows the user to generate conductive interfaces with one click. ESATAN recognizes the interfaces and assigns them to be fused. This provides the thermal model with a single continuous surface with no contact resistance across the interface. The contact resistance can be due to different materials, impurities, or improper contact between the two bodies. It is assumed that fused contacts can represent all conductive interfaces. Figure 5.4 shows the conductive interfaces as determined by ESATAN. ESATAN only generates conductors for visible components. Thus, the user must click "show" on the model before generating conductive interfaces. Otherwise, certain conductors may be neglected unintentionally.

Almost all conductive interfaces are correctly generated, except for each surface/component that is in contact with any side of the nadir-facing surface. This includes the side panels, the primary mirror, and the SMDS. These conductive interfaces are not generated automatically because the nadir-facing surface consists of multiple shells. The nadir-facing geometry was created this way since solid surfaces can not be cut, which was required to create the hole in which the M1 is located. The contact between shells and solids is not identified, and thus the conductive interface is not generated. It is not possible to have a surface-type conductive interface between a shell and a solid.

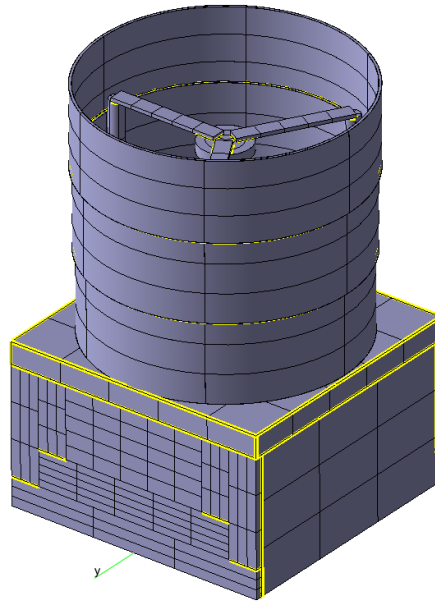
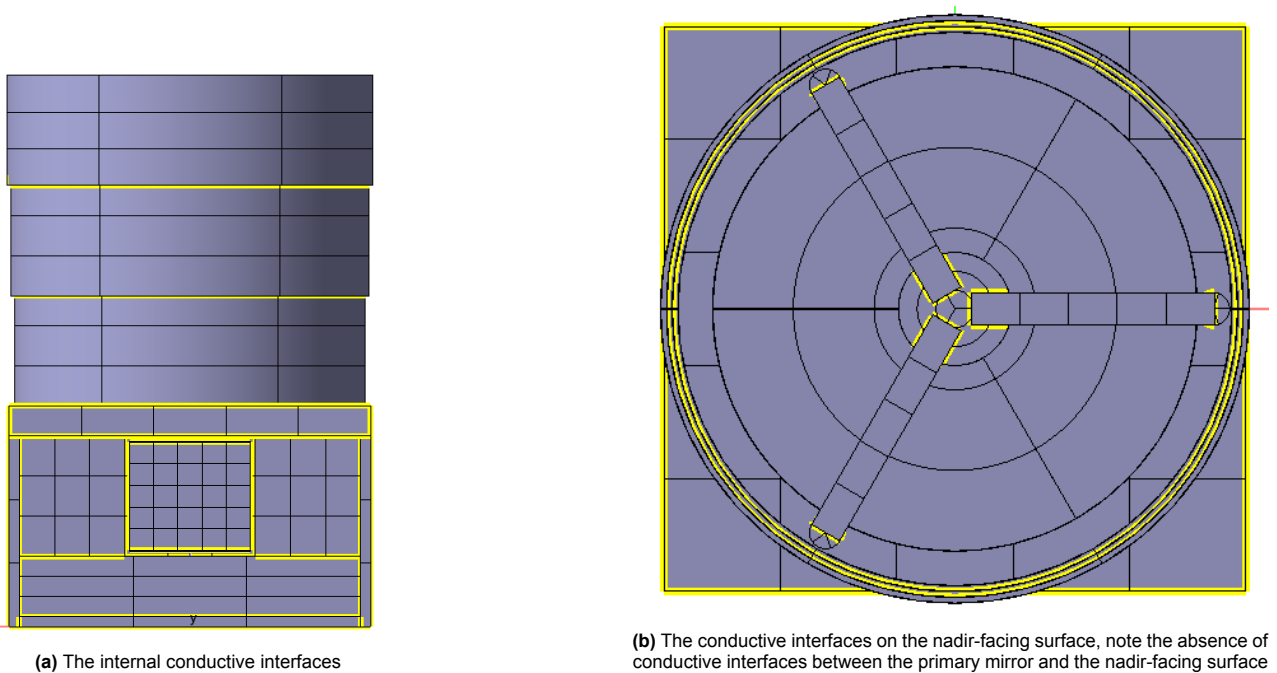


Figure 5.4: The automatically generated conductive interfaces, the conductive interfaces between the cryo- and the cold-stage have been removed, as well as between the cold stage and the R-side panel

The conductive interfaces between the nadir-facing surface and the side panels, the mirror, and the SMDS legs are thus represented by a user-defined conductor. These conductors' values are calculated by the thermal resistance method:

$$\frac{1}{k_{eq}} = \frac{1}{k_1} + \frac{1}{k_2} \quad (5.1)$$

For the interface of the nadir-facing surface ($k = 247 \frac{W}{mK}$) with the side panels ($k = 1.35 \frac{W}{mK}$), this yields a thermal conductivity of $1.343 \frac{W}{mK}$, rounded to $1.35 \frac{W}{mK}$. For the interface of the nadir-facing surface and the mirror ($k = 120 \frac{W}{mK}$), this yields a thermal conductivity of $80.76 \frac{W}{mK}$. The interface of the nadir-facing surface and the SMDS legs ($k = 24 \frac{W}{mK}$) yields a thermal conductivity of $21.875 \frac{W}{mK}$. This yields the conductors as shown in Table 5.5. The conductors calculated in Section 5.2 are included in this table.



(a) The internal conductive interfaces

(b) The conductive interfaces on the nadir-facing surface, note the absence of conductive interfaces between the primary mirror and the nadir-facing surface

Figure 5.5: A more in-depth view of the conductive interfaces

Conductor	Source	Destination	Value [W/K]
Baffle1_Nadirfacing_(1-6)	Baffle 1	Nadir-facing Surface	1 (6 in total)
Bus2Nadirfacing	Bus 2	Nadir-facing Surface	100
Bus3Nadirfacing	Bus 3	Nadir-facing Surface	100
Bus4Nadirfacing	Bus 4	Nadir-facing Surface	100
DetectorMount	Detector	Instrument Box	0.0001152
FilterMount	Filter	Instrument Box	0.0001152
InstrumentMount_(1&2)	Instrument Box	Nadir-facing Surface	0.000576
InstrumentMount_(3&4)	Instrument Box	Bus segment 4	0.000576
RadCryoMount_(1&2)	Cryo stage	Nadir-facing Surface	0.000269
RadColdMount1_(1&2)	Cold stage	Nadir-facing Surface	0.000269
Radiator_side_2_nadirfacing	R-side panel	Nadir-facing surface	1.35
Radiator_side_3_nadirfacing	R-side panel	Nadir-facing surface	1.35
SMDS1_nadirfacing	SMDS leg 1	Nadir-facing surface	21.875
SMDS2_nadirfacing	SMDS leg 2	Nadir-facing surface	21.875
SMDS3_nadirfacing	SMDS leg 3	Nadir-facing surface	21.875
Side1_nadirfacing	Side panel 1	Nadir-facing surface	1.35
Side2_nadirfacing	Side panel 2	Nadir-facing surface	1.35
Side3_nadirfacing	Side panel 3	Nadir-facing surface	1.35
ThermalStrap_ColdStage	Instrument Box	Cold stage radiator	300
ThermalStrap_CryoStage	Detector	Cryo stage radiator	300
nadirfacing_mirror_conductor	M1	Nadir-facing surface	80

Table 5.5: The conductors for the initial thermal model

5.4.1. MLI

Special attention is paid to the modeling of the MLI. Several surfaces will be covered in MLI. The baffle's outside surface is covered with MLI, as well as the radiator and bus surfaces facing the satellite's insides (and each other). The MLI is modeled as described in Section 5.1.1. Two different versions of MLI will be applied, the 2-layer MLI as defined by Arink, and MLI with an effective emissivity of 0.01. They will be named "2-layerMLI" and "MLI" respectively. The effective conductivity was calculated by Arink and has a value of 0.165. For each surface covered by MLI, the MLI and its conductor must be calculated. This represents the conduction through the spacers. Table 5.6 shows the area of each MLI component and the accompanying conductor. The thickness of each MLI blanket is assumed to be 3 mm. For the baffle, the conductor is calculated for the total surface area and then divided by 6, as the geometry is divided into 6 faces. The total conduction can not be applied to just one face, as this would create unrealistic thermal gradients. The conductors for the MLI applied to the other components are created by applying them to the center of the MLI and the respective component.

Source	Destination	Surface Area m^2	$\frac{kA}{x} \frac{W}{K}$
Baffle 1	Baffle Segment 1 MLI	$2\pi \cdot 0.175 \cdot 0.12$	7.2 (1.2 per face)
Baffle 2	Baffle Segment 2 MLI	$2\pi \cdot 0.1786 \cdot 0.12$	7.4 (1.23 per face)
Baffle 3	Baffle Segment 3 MLI	$2\pi \cdot 0.1822 \cdot 0.12$	6.9 (1.15 per face)
Rad Cold 1	Rad Cold 1 MLI	$0.28 \cdot 0.05$	0.77
Rad Cold 2	Rad Cold 2 MLI	$0.04 \cdot 0.1$	0.22
Rad Cold 3	Rad Cold 3 MLI	$0.04 \cdot 0.1$	0.22
Rad Cryo	Rad Cryo MLI	$0.2 \cdot 0.1$	1.1
Bus 3	Bus MLI 1	$0.1 \cdot 0.12$	0.693
Bus 2	Bus MLI 2	$0.1 \cdot 0.12$	0.693
Bus 1	Bus MLI 3	$0.34 \cdot 0.06$	1.122
Bus 4	Bus MLI 4	$0.128 \cdot 0.118$	0.83
Bus 3	Bus MLI 5	$0.118 \cdot 0.219$	1.42
Bus 2	Bus MLI 6	$0.118 \cdot 0.219$	1.42
Bus 1	Bus MLI 7	$0.128 \cdot 0.219$	1.54

Table 5.6: The conductors for the MLI in the initial thermal model

5.5. Radiative Cases

The radiative case definition allows the user to define the thermal environment, the orbital parameters, and the satellite pointing. The radiative case performs the calculation only for the current iteration of the model. For any changes to the model geometry, optical properties definition, or radiative case definition, the radiative case must be recalculated. For example, changing the optical properties of the cryo stage radiator results in the invalidation of the previous radiative results of the entire model, and it must thus be run again.

5.5.1. Environment

The thermal environment will be unchanged in the initial analysis. The thermal environment can vary depending on local earth and sun conditions. The albedo and the solar constant may be changed, resulting in higher temperatures on the DST. In Section 6.2 the worst-case scenarios are investigated where both maximum and minimum cases are considered.

5.5.2. Orbit Parameters

The orbit parameters define how the DST demonstrator will orbit around the Earth. The orbit parameters have been determined in Section 3.1.3. The orbit parameters are defined for each radiative case, after which the case is run.

5.5.3. Satellite Pointing

The thermal model is defined with respect to the Model Coordinate System (MCS) and must be oriented to the Inertial Coordinate System (ICS). The pointing method that will be used in this thesis is the pointing vectors and directions method. This requires the user to specify a primary pointing vector and direction, and a secondary pointing vector and direction. The primary pointing vector represents the fixed components of the spacecraft. The secondary pointing vector represents the rotating/moving components of the spacecraft. [39] The pointing of the spacecraft will be done such that the M1 points nadir, and the radiator panel is in the shadow as much as possible.

5.6. The Analysis Case

The analysis case definition allows the user to specify various aspects of the thermal analysis that ESATAN will perform. Settings such as the step time and the maximum analysis duration can be altered. The analysis of the initial thermal model will be done using transient analysis. The option "cyclic solution" is selected. The analysis case settings as those used by Hu, [35], are used for this analysis. The analysis case has an output interval of 50 seconds and an orbit duration of 5428 seconds.

Boundary Conditions

The boundary conditions are also applied in the analysis case definition. The boundary conditions represent the thermal constraints on the model. The boundary conditions have been established in the previous sections. Depending on the case examined, the boundary conditions have different values. The detector and filter boundary conditions do not change and always have 0.2 and 0.032 W as their values, respectively. The bus heat input is 50 W, as determined in Section 3.2.4. These boundary conditions will be set as total volume heat loads, which imply that this heat load is acting on the entire volume. Since the geometry is reduced to smaller bodies by the mesh, this allocates the equivalent amount of heat to each sub-body.

5.6.1. Analysis case results

ESATAN provides various results from the analysis case. The primary results that are of interest are the temperatures of the components and the heat inputs. The heat inputs will be used to determine whether the applied coatings are sufficient or if they need to be changed. The heat inputs are divided into two categories, the external heat sources, and the incoming conductor heat flow. The external heat sources consist of the Earth's IR, the albedo, and the incoming solar radiation. The external heat sources are all radiative heat transfer. The incoming conductor heat flow consists of all incoming heat flow from the components of the satellite. This heat flow consists of both radiation and conduction. Unfortunately, it is not possible to separate the incoming conductor heat flow into its conductive and radiative portions.

5.7. The Initial Thermal Model Results

The initial thermal is built as described in the previous sections. The initial thermal model will examine the 6 PM SSO at an altitude of 300 km, using ESATAN's standard settings. In actuality, this represents a 3 PM orbit at the vernal equinox. The orbit analysis in Section 6.1 will set the orbit conditions to the vernal equinox. This analysis will focus on the radiator's design. A margin of 1 cm is left between the bus and the R-side panel to prevent any conduction. The bus components have been covered with MLI, and the inside-facing surface of the nadir-facing surface and the M1 have been covered with highly reflective 425-3m tape, with an emissivity of 0.03 and an absorptivity of 0.2.[47] The analysis will provide the detector temperature results, the instrument box temperature and temperature gradient results, and the external and conductor heat flow for the cryo- and cold-stage radiators. To measure the temperature gradient on the instrument box, the two faces as highlighted in Figure 5.6 are used as data points.

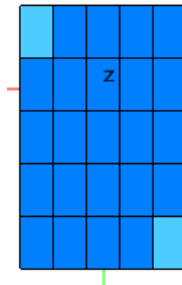


Figure 5.6: The two measurement points on the instrument box, viewed from the top

The analysis results can be seen in Figure 5.7 and 5.8. The detector temperature is approximately 196 K, and the instrument box hovers around 213.5 K. These temperatures are higher than predicted. The reason for this is shown in Figure 5.8. As can be seen, the conductor heat flow is comparable to the values used to calculate the initial surface area of the radiator. However, the external heat flow, which was purposefully not taken into account, is much higher. The additional unaccounted-for heat input ranges from 1.5 to 1.9 W for the cold stage, and between 1.4 and 1.7 W for the cryo stage. Q_r represents the heat flows in the thermal network diagram in Figure 5.3.

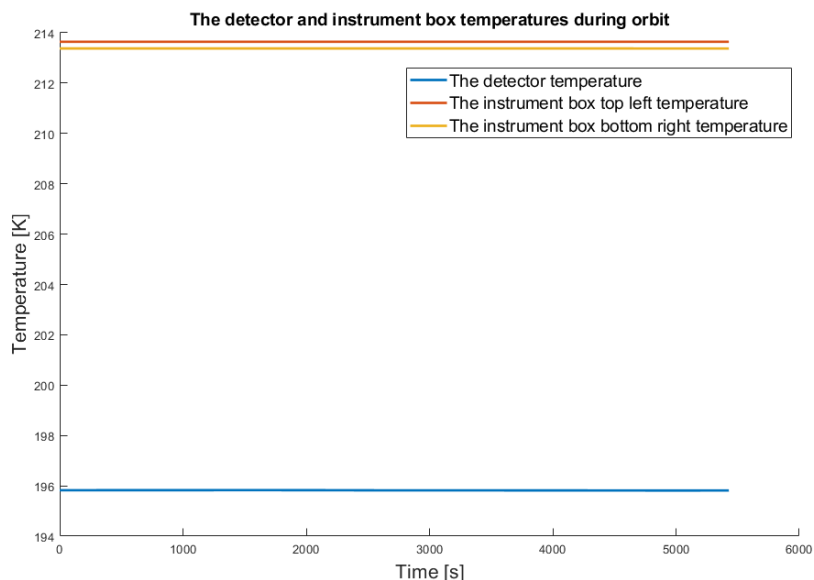


Figure 5.7: The detector and instrument box temperatures for the initial thermal model

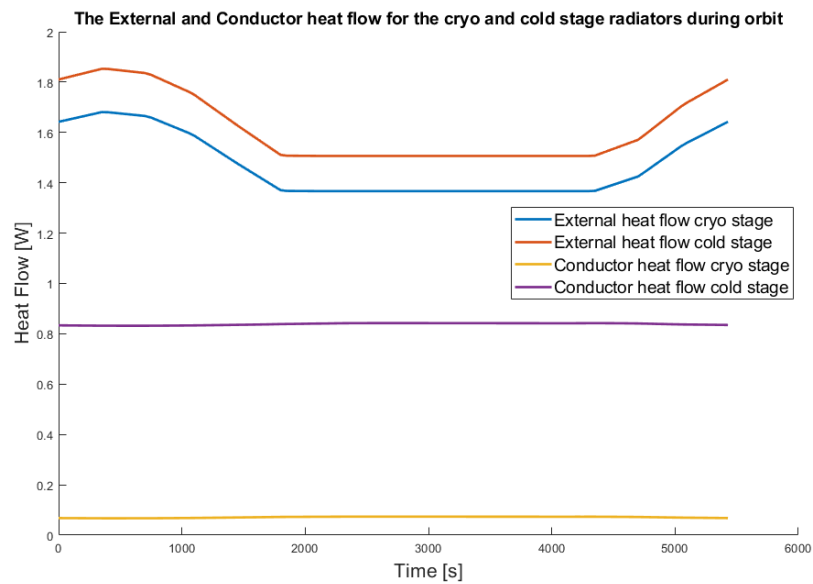


Figure 5.8: The external and conductor heat flow for the initial thermal model

An important observation for these images is the difference in temperature between the detector and instrument box. This temperature difference can be attributed to two factors. First, the detector heat load is much lower than the instrument box heat load, as shown in Figure 5.8. The conductor heat flow for the cryo-stage radiator is approximately 0.1 W, while it is approximately 0.85 W for the cold-stage radiator. This will inevitably result in a higher temperature for the instrument box. Theoretically, this should pull the detector temperature up, closer to the instrument box temperature. However, this is not the case due to the low conductor value. Due to the low conduction between the instrument box and the detector, the temperature of the detector is much lower. The conduction between the detector and the instrument box is a portion of the conductor heat flow of 0.1 W.

5.8. Earth shade

As was determined in the previous section, the external heat flow is very high, resulting in the detector not reaching the desired temperature. To remedy this, an Earth shade door analysis will be done. The Earth shade door, shown in cyan in Figure 5.9, reduces the incoming earth IR and albedo by creating an artificial (partial) shadow. Reducing the heat input like this greatly reduces the detector temperature. The Earth shade door length is varied to 30 cm. Initially, the Earth shade was analyzed up to 19 cm, the same length as the radiator side. However, it was observed that the temperatures did not reach an asymptotic value at 19 cm. Increasing the length of the Earth shade door further shows a further reduction in the temperature, but is also expected to make it more difficult to deploy. If it is the same length as the side panel, then a simple unfolding mechanism will suffice. Making it longer will require a more complex unfolding mechanism. The TROPOMI mission is used as inspiration for the Earth shade door's optical design, where a polished aluminum coating with an emissivity of 0.02, a specular reflectivity of 0.95, and an absorptivity of 0.1 is used. It is assumed that the reflectivity in the solar spectrum is fully specular. [75]

The analysis results are shown in Figures 5.10 and 5.11. As can be seen, with an increasing Earth shade door length, the detector and instrument box temperature decrease. The detector temperature reaches a value of 125 K for an Earth shade door length of 19 cm, meeting the requirements. Increasing the length further shows that the temperature graph starts behaving asymptotically at around 120 K. The instrument box temperature reaches 188 K, meeting the requirements as well.

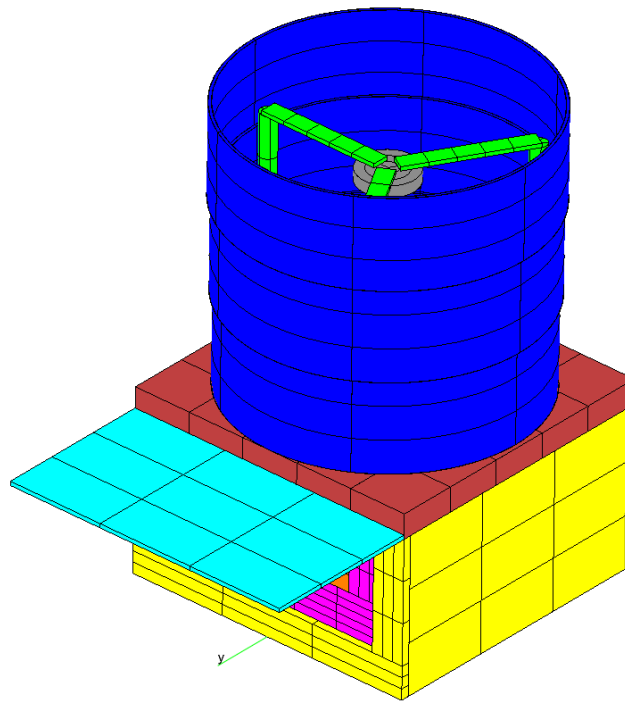


Figure 5.9: The geometry of the DST in ESATAN, with the Earth-shade door added

The influence of the Earth shade door on the external and conductor heat flow is visible in Figure 5.11. As the Earth shade door's length increases, the external heat input drops significantly. This results in a temperature decrease in the detector and instrument box. In turn, this causes a larger temperature difference between the nadir-facing surface and the instrument box, as well as between the instrument box and the detector. Due to this higher temperature difference, the magnitude of the conductive and radiative heat transfer is increased. As the temperatures are reduced less with the increase of the Earth shade door, the conductor heat flows also increase less. The radiative heat transfer between the Earth shade door and the cryo and cold stage also increases the conductor heat flow.

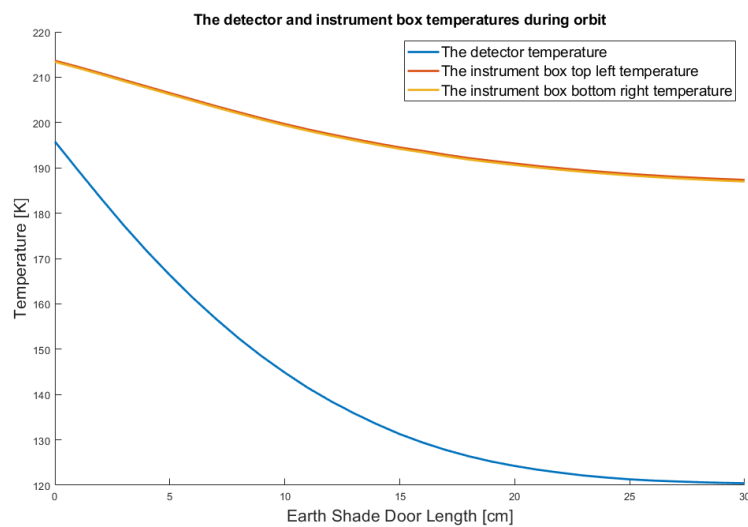


Figure 5.10: The average detector and instrument box temperatures plotted against the Earth Shade door length

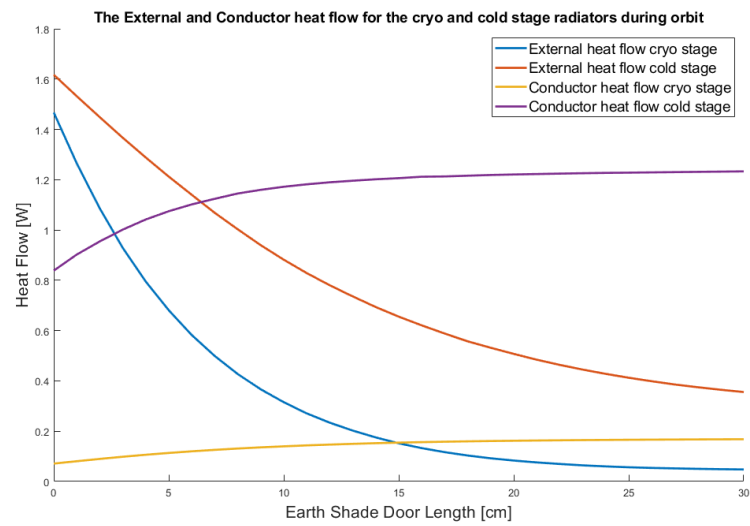


Figure 5.11: The average external and conductor heat flow plotted against the Earth Shade door length

5.9. Earth shade Sides

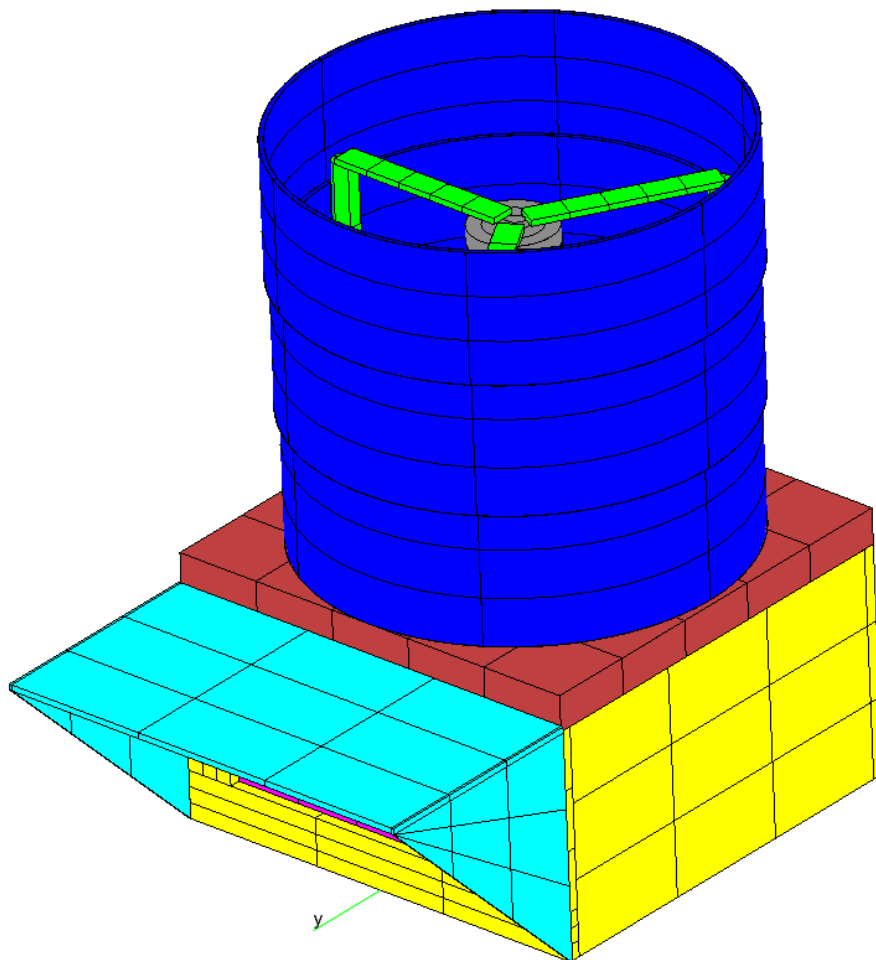


Figure 5.12: The geometry of the DST, with the Earth-shade door and its sides added, in cyan

The previous section shows that the addition of the Earth shade door provides a significant improvement to the detector and instrument box temperature. However, the temperatures can be reduced further. Therefore, in this section, the external heat flow on the radiator is reduced further by adding sides to the Earth shade door, as shown again in cyan in Figure 5.12. These sides are again varied from 0 until the total length of the side panel, 19 cm. The results are shown in Figures 5.13 and 5.14. As can be seen, the temperature decreases slowly but not as significantly as before. The addition of the sides reduces the heat flow on the cryo and cold stage radiators but simultaneously increases the conductor heat flow. Figure 5.15 shows the net heat flow of the cryo and cold stages. It can be seen that a side length of 10 cm results in a negative heat balance for the cryo-stage radiator. This means that the reduction of external heat was less than the increase in conductor heat flow. However, it can also be seen that the change in net heat flow for the total area of the radiator is still positive. Therefore, in the following section, an optimization analysis of the cryo- and cold-stage radiator surface area will be done.

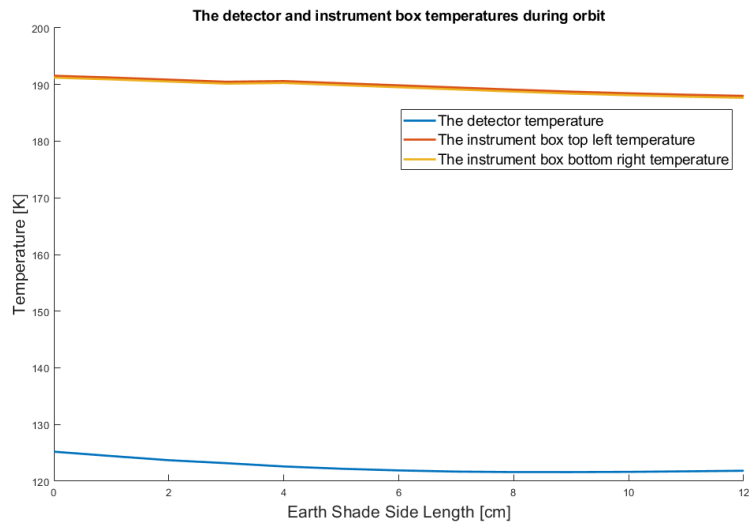


Figure 5.13: The average detector and instrument box temperatures plotted against the Earth Shade side length

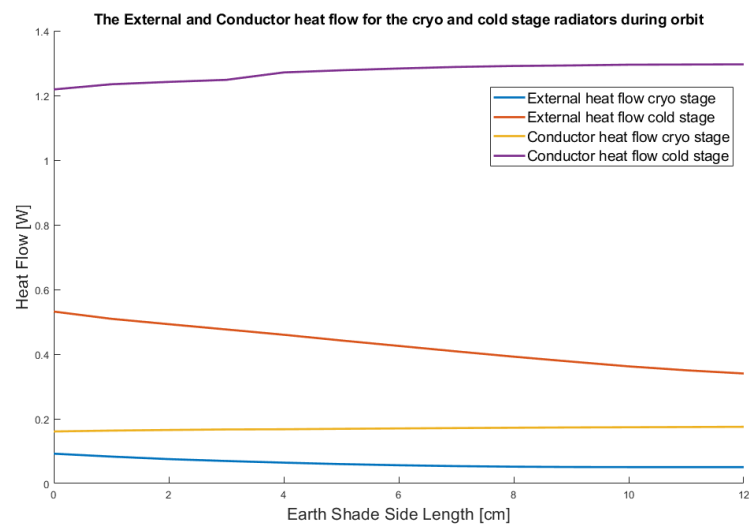


Figure 5.14: The average external and conductor heat flow plotted against the Earth Shade side length

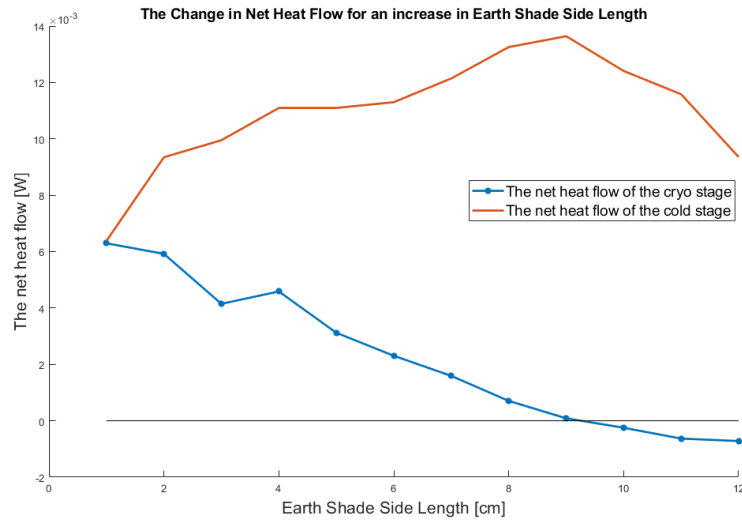


Figure 5.15: The net heat flow

5.10. Radiator Area Optimization

As was determined in the previous section, the change in net heat input on the cryo stage radiator for an Earth shade side length of 10 cm was negative, resulting in a higher detector temperature. This provides meaningful input for the investigation of the optimal radiator sizing/design. The Earth shade sides analysis will be continued until 19 cm. The radiator and R-side panels are given a mesh size of 1 cm. Figure 5.16 shows the net heat change over the entire radiator surface for an increase of 1 cm for the Earth shade sides. As long as the graph is above the y-axis, the increase in the Earth shade side size reduces the heat input on the R-side panel more than it increases the heat input via radiative heat transfer to the panel. As can be seen, each iteration reduces the heat input further until iteration 19. This implies that Earth shade sides with a length of 18 cm are the optimal Earth shade side length to reduce the heat input on the radiator as much as possible.

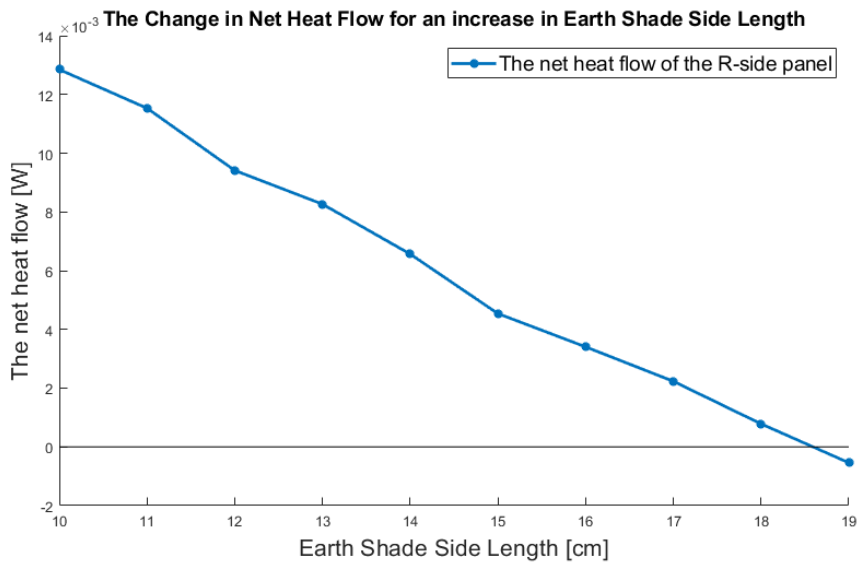


Figure 5.16: The net heat flow for the R-side panel

To determine the optimal cryo- and cold-stage radiator area, the potential temperature of each 1 cm by 1cm square is investigated. This is done by extracting the external heat on each square. Subsequently calculating the heat transfer for every 10 degrees, from 200 K to 50 K. The results of this analysis are shown in Appendix A.

Figure 5.17 shows the results for a side length of 18 cm, assumed to be the optimal case. Several conclusions can be made from this analysis. First, the combination of the Earth shade door and its sides provides an area that is almost completely shaded, represented by the yellow area. Additionally, the heat seems to be weakly parabolic, with most horizontal bands having the same temperature.

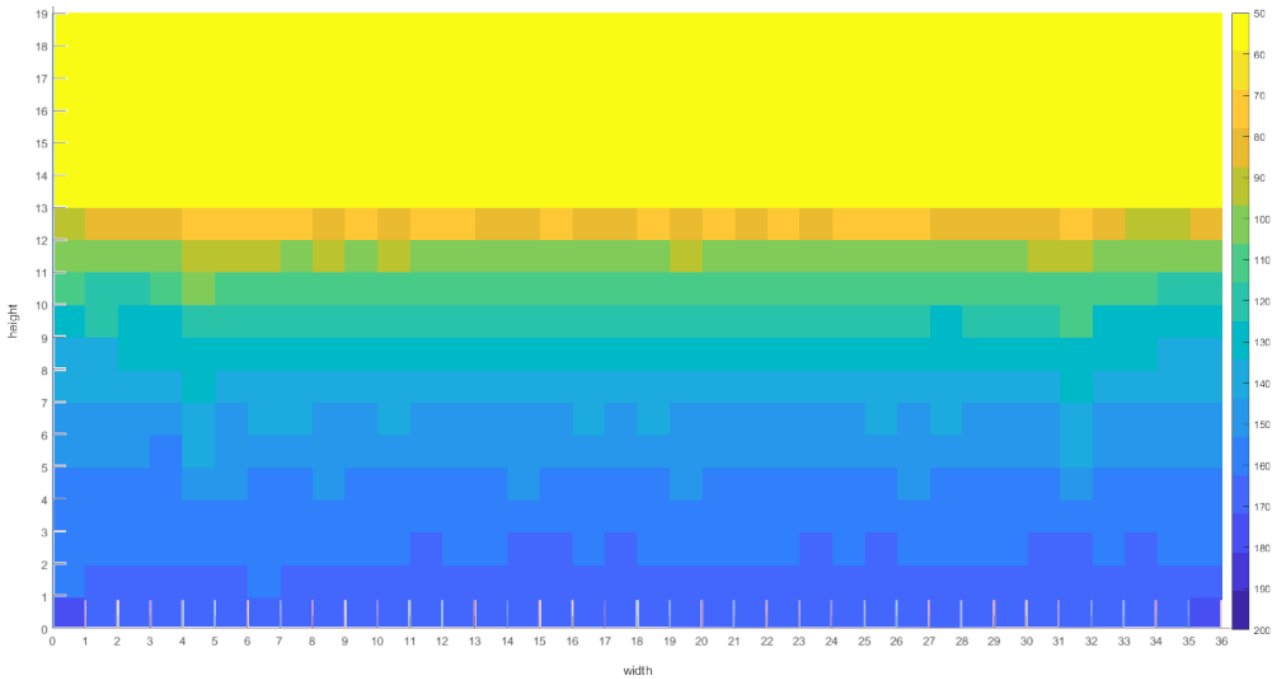


Figure 5.17: The potential temperatures for an Earth shade side size of 18 cm, using only the external heat input

The optimal radiator design will thus be investigated by making the cryo and cold stages the full width (36 cm). The cold stage height will initially be set at 6 cm, for a total surface area of 0.0216 m^2 , comparable to its size in the initial analysis. The cryo stage radiator is then varied from 1 cm until an optimum size is found. The results of this analysis are shown in Figure 5.18.

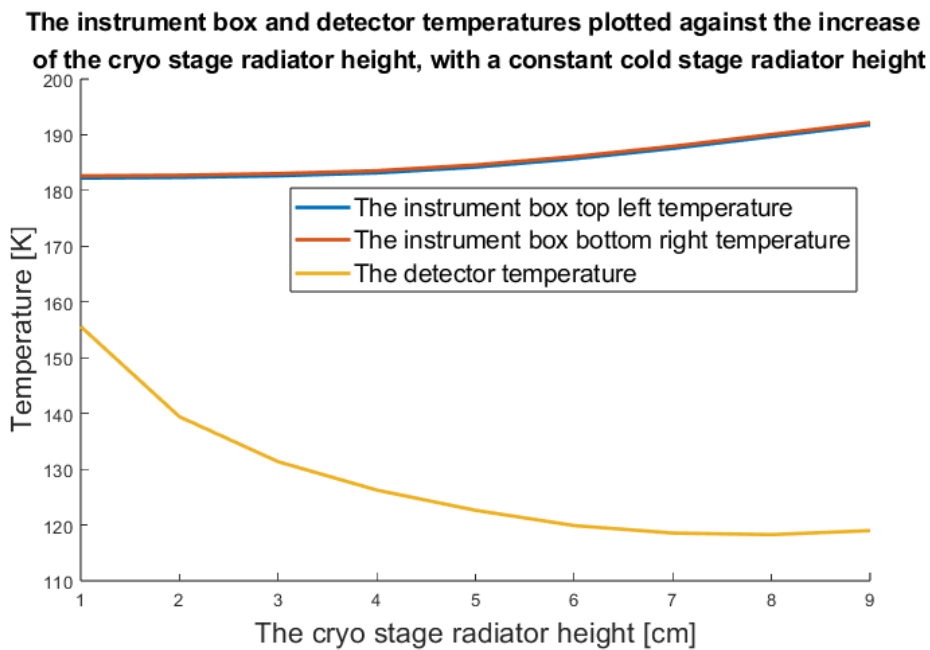


Figure 5.18: The instrument box and detector temperatures for an increasing cryo stage radiator height

As can be seen, initially the detector temperature strongly decreases with an increasing cryo-stage radiator area. The detector temperature reaches an asymptotic value of approximately 118.5 K for a cryo-stage height of 7 cm. The temperature is reduced by approximately 0.2 by increasing the length to 8 cm, but this also increases the instrument box temperature by 2 degrees. Further increasing the cryo-stage length to 9 cm increases the detector and instrument box temperatures. Therefore, the decision is made to set the cryo-stage height at 7 cm. The heat flows into the cryo- and cold-stage radiators are shown in Figure 5.19. As can be seen, as the cryo stage's size is increased, the detector temperature drops, and the conduction from the instrument box increases. After a certain point, increasing the size of the cryo stage radiator results in an increase of the external heat flow, as the shaded area, shown in yellow in Figure 5.17, is exceeded.

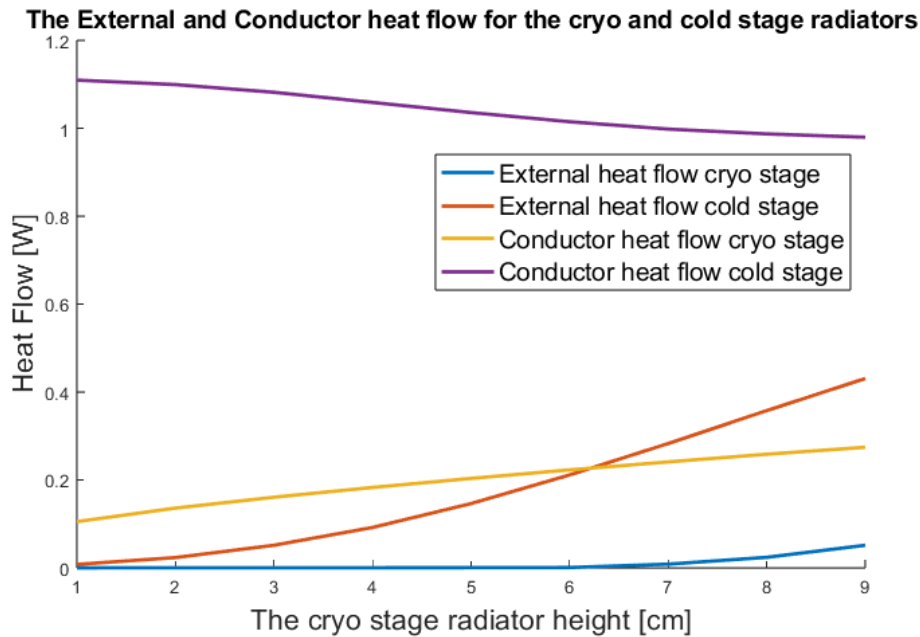
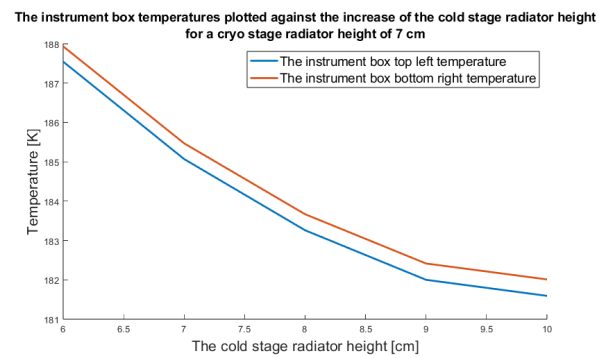
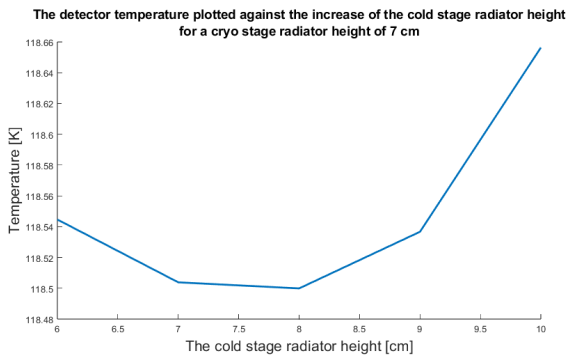


Figure 5.19: The external and conductor heat flows for the cryo and cold stage radiators

With the cryo-stage height determined, the cold-stage height is investigated. The analysis is done comparably, with the 7, 8, and 9-cm cryo stage radiators used for the analysis. The results of the cold-stage radiator analysis are shown in Appendix B. The baseline height for the cold-stage radiator is set at 6 cm, as was used in the cryo-stage analysis. The height is increased until an optimal combination is found. Figures 5.20a and 5.20b show the cold-stage radiator area analysis for the chosen cryo-stage height. The detector temperature hovers around 118.5 K, with a minimum at a cold stage height of 7/8 cm. Afterward, the detector temperature increases again, due to an increased conductor heat flow into the cryo stage radiator. The instrument box temperatures decrease more significantly. However, the overall temperature changes are small in magnitude. For this reason, the choice is made to set the cold-stage radiator at a height of 7 cm.

It is important to note that the detector temperature decrease does not incorporate the reduced radiative heat transfer. Due to the uncertainty regarding the detector's dimensions, this is not incorporated into the design. The observation can be made that the detector temperature will be slightly lower than in the current analysis. However, since the radiative heat transfer to the detector is very low compared to the conduction, this will not result in significant temperature changes.



(a) The detector temperature for a cryo stage radiator height of 7 cm, with a varied cold stage height

(b) The instrument box temperatures for a cryo stage radiator height of 7 cm, with a varied cold stage height

Figure 5.20: The detector and instrument box temperatures for a cryo-stage radiator height of 7 cm

The design of the DST’s R-side can be seen in Figure 5.21. The temperature values are within the defined limits of the DST. The instrument box temperature is 15 K lower than the desired temperature, and the detector temperature is 31.5 K below the requirement. The external heat flow has been reduced significantly. The external heat flow could be reduced further, however, this would require a longer Earth shade door which adds significant complexity to the design. The current Earth shade door design can be unfolded easily, increasing its size may require an additional mechanism to achieve deployment. The conductor heat flow has been optimized partially, as the radiator surface is coated with MLI, and the components are mounted using very-low conductivity materials.

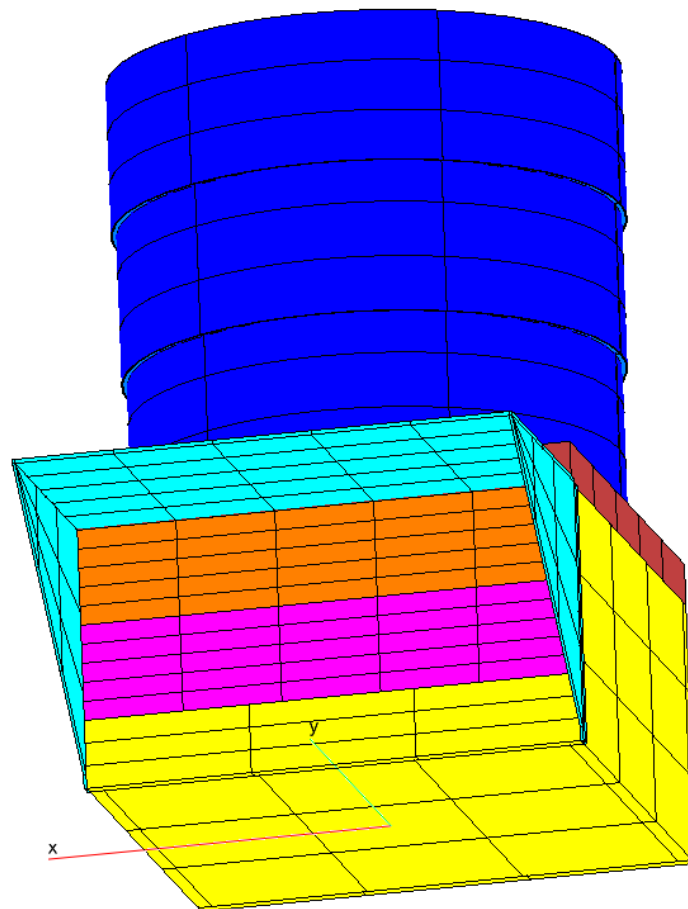


Figure 5.21: The design of the cryo and cold stage radiators

5.11. Chapter Summary

In this chapter, the initial thermal model and its improvements have been detailed. The bulk material definition and coatings have been defined. The model assumptions have been detailed. The initial cryo- and cold-stage radiator sizes have been calculated, assuming an idealized scenario where there is no external heat. The theoretical conductor values for the detector and filter mounts have been determined, as well as the mounting equipment of the radiator to the spacecraft, focusing on low conductivity. The conductive interfaces between components that were not automatically generated by ESATAN have also been defined, as ESATAN does not recognize contact between shells and solids. The conductors between the MLI and the components which are covered in MLI have also been determined. The radiative case and analysis case definition are shortly investigated, as the analysis results depend on the settings of the analysis and radiative case definition.

Following this, the initial thermal model is sufficiently set up to perform the first analysis. The first analysis showed that the temperatures were above the set limits, 200 K for the instrument box and 150 K for the detector. This was attributed to the high external heat flow. The Earth shade door was introduced to reduce the external heat flow. The Earth shade door provides (partial) shading to the radiator, allowing the temperature to be dropped significantly for both radiator stages. This allowed the detector and instrument box to reach below 150 K and 200 K, respectively. To further reduce the heat flow, and create an area that is nearly completely shaded, side covers were added to the Earth shade door. This dropped the temperature further, but not significantly. Furthermore, it was determined that the net heat flow on the cryo stage radiator increased after increasing the size of the side covers further.

Thus, it became apparent that radiator optimization was necessary. The R-side was divided into a 1 cm by 1 cm mesh to determine the optimal radiator dimensions. Then, the external heat flux per square was determined, and the equilibrium temperature was determined as if the square received no other heat. This showed that there is an area on the R-side that can be cooled to very low temperatures. To determine the dimensions of the cryo stage radiator, its height was varied from 1 to 9 cm, using a constant cold stage height of 6 cm. This showed an optimal cryo-stage radiator height of 7/8 cm, where the 7 cm cryo-stage resulted in lower instrument box temperatures. Thus, the cryo-stage height was set at 7 cm. The cold-stage radiator was then analyzed in the same way. The detector temperature did not show significant changes, the instrument box temperature decreased more strongly. The final choice was made to set the cold-stage dimensions at the point of minimum detector temperature, thus also 7 cm high. Once the structural requirements are known, the results of the analysis show the accompanying temperatures that can be expected. Thus, the final design of the DST demonstrators' radiator is a 7 cm high cryo-stage radiator, a 7 cm high cold-stage radiator, and the remaining 5 cm consists of a (structural) sandwich panel. This configuration then yields a detector temperature of 116.76 K and an instrument box temperature of approximately 183 K, both values meeting the requirements.

Full system level Thermal Analysis

In this chapter, the other aspects of the thermal analysis are investigated. Various additional analyses of the DST's design are done, to bring the behavior at full system level into context. The orbit analysis investigates the applicability of the radiator and Earth shade door design. An optimal orbit is determined that provides the lowest detector temperatures. After finding the optimal orbit, the worst-case analysis determines the minimum and maximum temperatures that the DST demonstrator may encounter. Subsequently, the instrument box thermal gradient is investigated to determine its influence on the alignment of the optical elements inside the instrument box. The influence of changing the conductor material is explored. Subsequently, the sensitivity analysis is performed to alleviate concerns regarding the approximations made when calculating the bus heat dissipation. Finally, the baffle's coating arrangement and material definition are explored, which also serve as input for further design and analysis of the baffle.

6.1. The orbit analysis

The orbits analyzed in the orbit analysis have been specified in Section 3.1.3. Table 6.1 shows the orbits that will be examined again. From this section on, the orbits are defined relative to the vernal equinox, where the solar declination and right ascension are both equal to zero. The orbit analysis will determine the thermal results of choosing a different orbit on the detector temperature to determine whether the current radiator and Earth shade door design is functional for different (Sun-synchronous) orbits. The orbit that yields the lowest detector temperature will be used for the remaining analyses in this chapter so that a final, lowest possible temperature is determined.

Orbit	Semi-major axis (a) [km]	Inclination (i) [deg]	Right ascension (RAAN) [deg]
Sun-synchronous 12 PM	300 (+6371)	96.648	0
Sun-synchronous 2 PM	300 (+6371)	96.648	30
Sun-synchronous 4 PM	300 (+6371)	96.648	60
Sun-synchronous 6 PM	300 (+6371)	96.648	90
Sun-synchronous 8 PM	300 (+6371)	96.648	120
Sun-synchronous 10 PM	300 (+6371)	96.648	150
Sun-synchronous 12 AM	300 (+6371)	96.648	180

Table 6.1: The orbits that will be used to analyze the thermal environment on the spacecraft.

The pointing of the satellite is defined such that the inside surface of the Earth shade door and the radiator surfaces receives as little solar radiation as possible. The orbits ranging from 12 PM to 12 AM (12:01 PM until 11:59 PM) are all defined in the same manner. The pointing definition for the orbits ranging from 12 AM until 12 PM (00:01 AM until 11:59 AM) would be flipped. These orbits are not included in the analysis. Figure 6.1 shows the pointing definition for the 10 AM and 2 PM orbits, which are both 30° off of the 12 PM orbit, with the 10 AM SSO on the left and the 2 PM SSO on the right. The yellow dot in the center is the sun vector, viewed head-on. As can be seen, the satellite's Earth shade door and radiator are flipped for the 10 AM orbit compared to the 2 PM orbit. It can also be seen that the satellite maintains the same push-broom scanning configuration, independent of the pointing configuration.

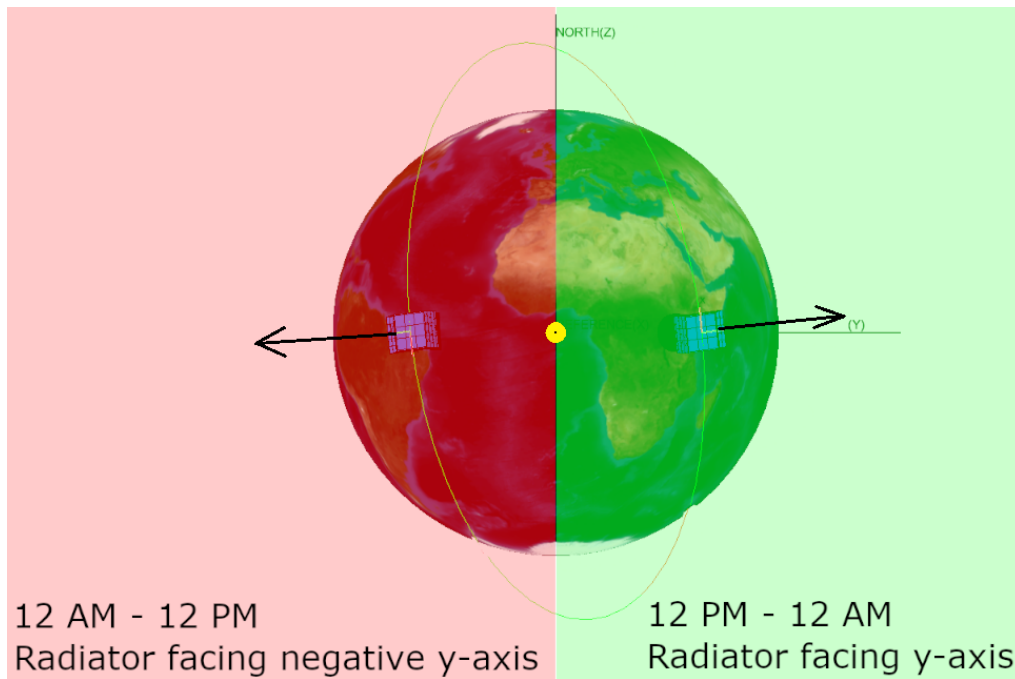


Figure 6.1: The pointing configuration for the 10 AM (left) and 2 PM (right) orbits

The results of the orbit analysis are shown in Figure 6.2. The 12 AM and 12 PM orbits have the highest detector temperature since they have periods where the interior surface of the Earth shade door is in full view of the Sun. This is unavoidable; however, the radiator surfaces do not receive direct sunlight. The 4 and 8 PM SSOs have nearly the same temperature, as they have nearly the same orbit, but mirrored. The same holds for the 2 and 10 PM SSOs. Finally, it can be seen that the 6 PM SSO has the lowest temperature. This is explained by the fact that the 6 PM SSO is perpendicular to the Sun vector. This allows the Earth shade door and the radiator surfaces to be in full shadow from the Sun. Since the 6 PM SSO yields the lowest detector temperature, it is used for the remaining analyses of this chapter.

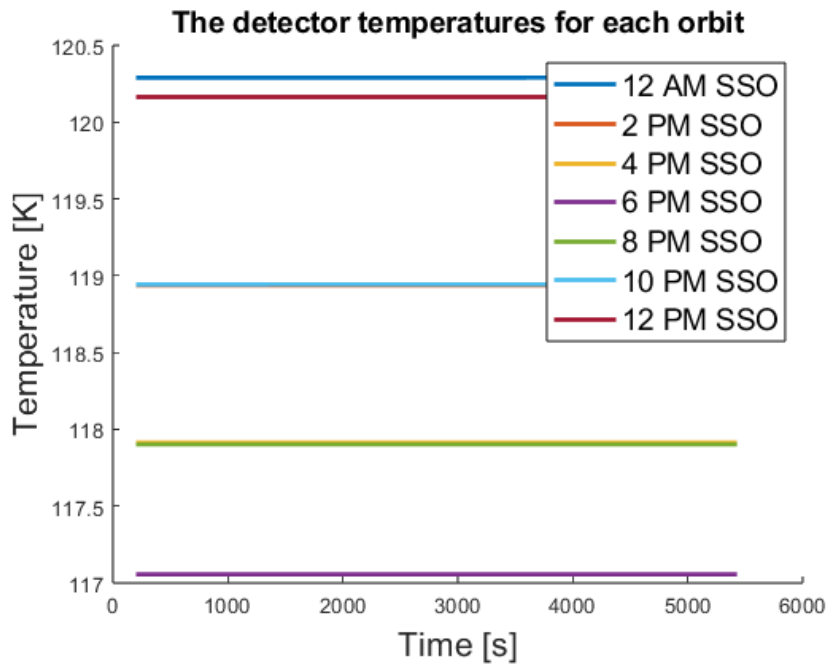


Figure 6.2: The detector temperature per orbit

The 6 PM SSO thus yields the lowest detector temperatures. Because it is perpendicular to the sun, it also has the most constant thermal environment. This also applies to the internal components. The worst-case analysis, done in Section 6.2, is done to determine the temperature range of the components of the satellite. The worst-case analysis will analyze the coldest and warmest possible environmental circumstances for the spacecraft. This analysis is done for the 6 and 12 PM SSOs, as it is assumed that they will show the largest difference. The 12 PM (and AM) have the longest eclipse times and thus should show the largest variation in temperatures. This can be seen in Figures 6.3a and 6.3b. As can be seen, the 6 PM SSO has a relatively stable heat input on its sides, while the 12 PM SSO has much more variation, showing both peaks and valleys as multiple surfaces are hit by the sun and the satellite goes into eclipse.

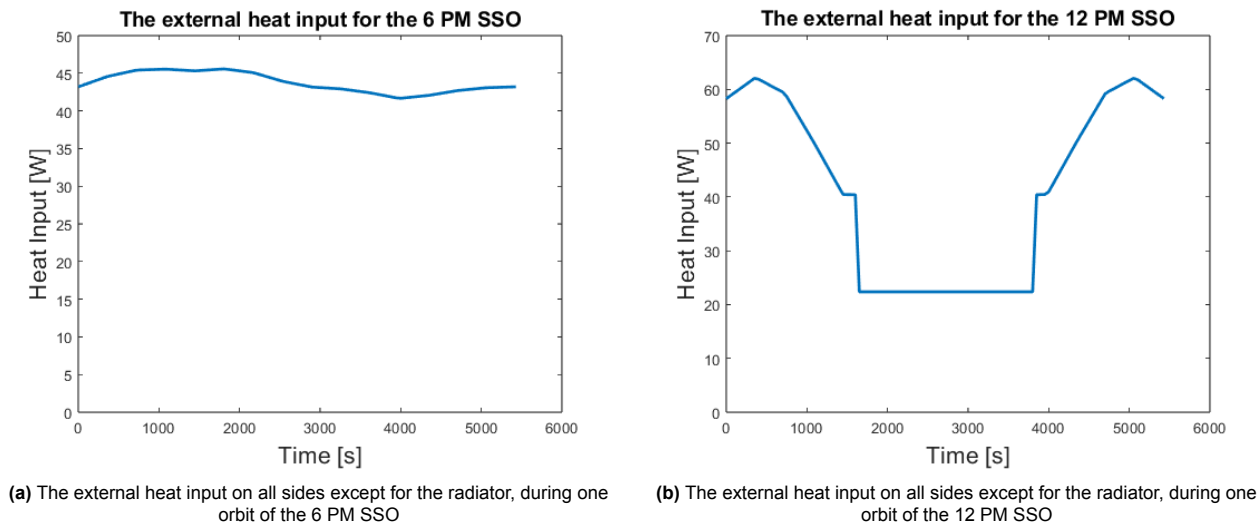


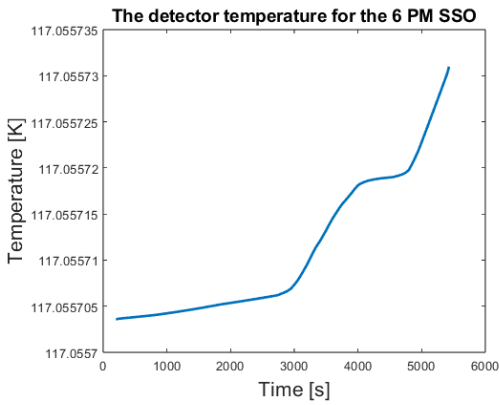
Figure 6.3: The external heat input on the sides of the spacecraft, during one orbit for the 6 and 12 PM SSOs

6.1.1. Simulation Tolerances and Long-term Temperature Evolution

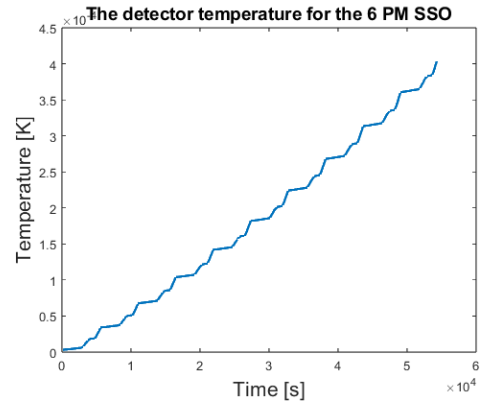
During the simulations, it was determined that the temperature graph of the 6 PM SSO did not yield a true repeating pattern, as can be seen in Figure 6.4a. If it were a true repeating pattern, then the graph would start and end at the same point. The analysis time is increased to 10 orbits to determine whether this pattern repeats itself. Additionally, the temperature at time point 1 is subtracted from all results, so that the total variation over the orbits is shown. Figure 6.4b shows that the pattern repeats itself. As can be seen, the total variation over ten orbits is 0.0004 degrees. To investigate the potential cause, the relaxation condition, or the allowable error, is made smaller, 0.001 and 0.0001 to be exact. The simulation time duration is not changed.

This yields the graphs seen in Figure 6.5a and Figure 6.5b. First, it can be seen that the behavior persists. A seemingly repeating pattern still appears but is smoothed out, as the analysis has a lower error tolerance. For the relaxation condition of 0.001, the total temperature variation over ten orbits is 0.01 degrees and for the relaxation condition of 0.0001, the total temperature variation over ten orbits is 0.015 degrees. Since this effect would compound over many orbits, the analysis is re-run but for the entire mission duration of 5 years, approximately 30000 orbits. The time step is increased to save computation time. The relaxation condition is returned to its original value of 0.01. Figure 6.6 shows the result of this analysis. As can be seen, the total temperature variation trends up over the first $1e7$ seconds, or approximately 115 days. Eventually, an equilibrium is reached, which is, on average, 0.18 degrees above the initial temperature, with an amplitude of approximately 0.01. The variation in the results afterward is explained by variations due to Sun cycles and the seasons.

The results in Figures 6.5a and 6.5b showed greater amplitudes over a period of 10 orbits and likely would have reached the equilibrium value in a shorter amount of (simulation) time. This leads to the conclusion that it would not take as long to reach the equilibrium temperature in real life, as there is no relaxation condition or simulation error tolerance in physical processes like heat transfer.

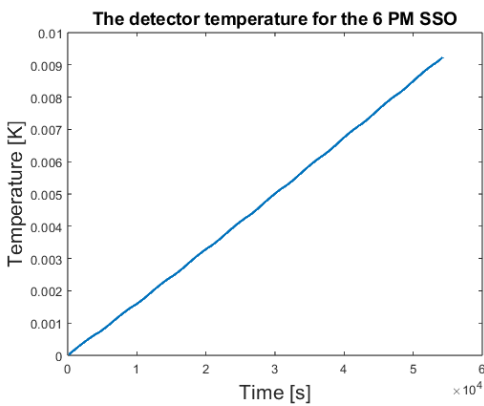


(a) The detector temperature for the 6 PM SSO

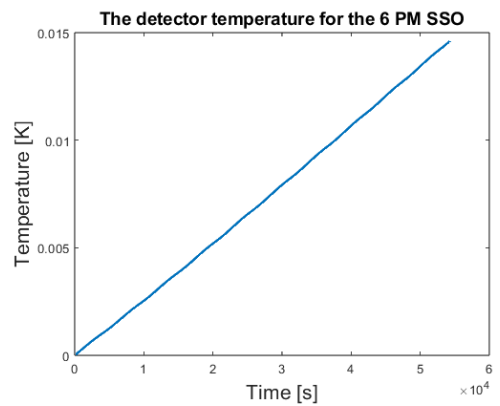


(b) The detector temperature for 10 orbits of the 6 PM SSO

Figure 6.4: The detector temperature for the 6 PM SSO, for one and ten orbit durations



(a) The detector temperature for the 6 PM SSO, with relaxation condition of 0.001



(b) The detector temperature for the 6 PM SSO, with relaxation condition of 0.001

Figure 6.5: The detector temperature for the cases where the relaxation condition is tightened

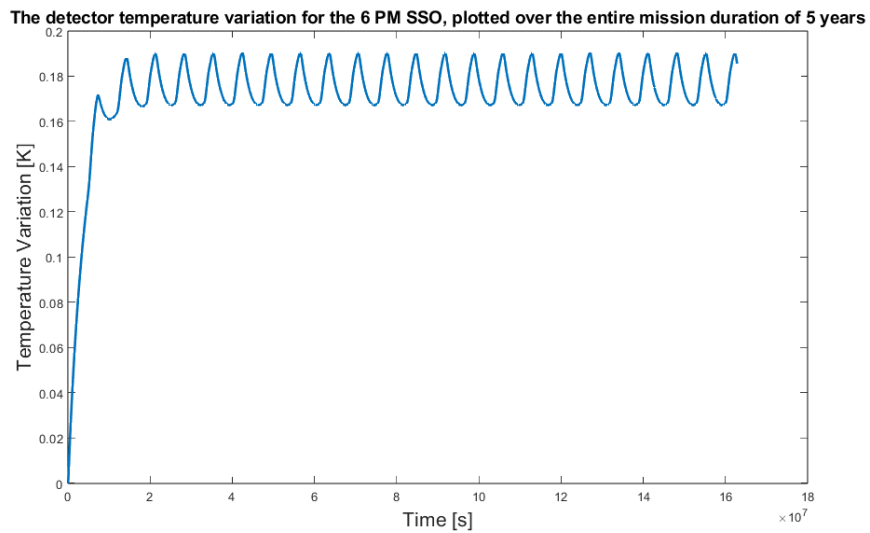


Figure 6.6: The detector temperature for the SSO 6 pm orbit, during the entire mission timeline of 5 years

6.2. Worst Case Analysis

In the worst-case analysis, the combination of environmental properties that will yield the highest and lowest temperatures will be applied to the 6 and 12 PM SSOs. The impact of the environmental parameters on the temperature of the satellite's components is detailed. The hot and cold cases will be run, and they will be compared to the "nominal" average case.

6.2.1. Solar Constant

The hot and cold cases will examine the absolute extremes of the possible hot and cold cases. Several values can be changed to simulate the hot and cold cases. The solar constant can vary depending on the solar cycle and the Earth's position in its orbit, as the elliptical orbit of the Earth results in a varying distance to the sun. ESATAN allows the user to define a separate solar constant, which will override the solar constant calculated by ESATAN, where the sun's temperature is used as the input. The standard solar constant is $1367 \frac{W}{m^2}$, for a sun temperature of 5778 K. Table 6.2 shows the solar constants that will be used in the hot and cold cases.

	Solar Constant [$\frac{W}{m^2}$]	Reference
Hot Case	1414	[6]
Cold Case	1322	[6]
Nominal Case	1367	ESATAN

Table 6.2: The solar constants for the hot, cold, and nominal cases

6.2.2. Albedo and OLR

The other environmental parameters that are of interest are the planet's albedo and the outgoing longwave radiation (OLR). The planet's albedo depends on the local conditions over which the satellite is flying. The albedo values vary wildly if the satellite flies over an ocean as opposed to cloud cover, for example. Therefore, for the minimum and maximum cases, the minimum and maximum albedo values are taken from [6]. It is not realistic to assume that the albedo is constant throughout the orbit, however, the focus is on the warmest and lowest temperature that the DST demonstrator may encounter. The OLR represents a combination of radiation emitted in infrared wavelength bands by atmospheric gases and radiation emitted by the Earth's surface and cloud tops. OLR is mainly influenced by the temperature of the Earth's surface and the amount of cloud cover. A warmer region of the Earth's surface emits more radiation than a colder area. [6] The OLR typically has a higher impact on high-inclination orbits. The OLR is represented by the Earth's temperature in ESATAN, thus for each OLR value the temperature is calculated according to the following equation:

$$T_E = \left(\frac{OLR}{\sigma} \right)^{\frac{1}{4}} \quad (6.1)$$

Where σ is the Stefan-Boltzmann constant. This yields the values as shown in Table 6.3.

	Albedo	OLR [$\frac{W}{m^2}$]	Earth Temperature [K]	Reference
Cold Case - Minimum Albedo	0.06	273	263.4	[6]
Cold Case - Minimum OLR	0.40	108	208.9	[6]
Hot Case - Maximum Albedo	0.50	180	237.4	[6]
Hot Case - Maximum OLR	0.22	332	276.6	[6]
Nominal Case	0.306	237	254.3	ESATAN

Table 6.3: The albedo and OLR values for the hot and cold cases

The results of the worst-case analysis are shown in Appendix C. The minimum and maximum OLR cases produce the minimum and maximum temperature results. The coating that is currently applied on a majority of the surfaces (MS74 white paint) has a high emissivity in the IR spectrum, and thus a high absorptivity in the IR spectrum. Therefore, the satellite is more sensitive to changes in the IR heat load from the earth, than from

the minimum and maximum albedo cases. The emissivity and absorptivity in the solar spectrum are much lower for this coating. Tables 6.4 and 6.5 show the maximum temperature changes that can be expected for the 6 PM and 12 PM SSO, respectively.

Component	Minimum Temperature [K]	Maximum Temperature [K]	Maximum Temperature Change
Baffle Segment 1	246.1	278.6	32.5
Baffle Segment 2	244.9	284.7	39.8
Baffle Segment 3	243.9	307.6	63.7
Bus	247.3	271	23.7
Detector	112.9	120	7.1
Filter	179.9	196.7	16.8
Instrument Box	171.1	190.6	19.5
Radiator - Cold	168.3	186.4	18.1
Radiator - Cryo	112.1	119.2	7.1

Table 6.4: The minimum and maximum temperatures and total temperature change for the 6 PM SSO

Component	Minimum Temperature [K]	Maximum Temperature [K]	Maximum Temperature Change
Baffle Segment 1	256.5	285.2	28.7
Baffle Segment 2	256.3	304.5	48.2
Baffle Segment 3	255.2	326.8	71.6
Bus	255.1	275.4	20.3
Detector	116.7	122.7	6
Filter	184.8	199	14.2
Instrument Box	176.6	193.1	16.5
Radiator - Cold	173.5	188.8	15.3
Radiator - Cryo	116	121.9	5.9

Table 6.5: The minimum and maximum temperatures and total temperature change for the 12 PM SSO

For the 6 PM SSO, the minimum temperature change for the hot and cold case is 7.1 degrees for the detector and the cryo stage radiator, and the maximum change is 63.7 degrees for the third baffle segment. It is assumed that the direct sunlight that the 12 PM SSO receives during its orbit will result in it having the highest temperature. Table 6.5 shows that the maximum temperatures are several degrees higher for all components compared to Table 6.4. It is assumed that the other orbits will fall between the values determined for these two orbit configurations.

6.2.3. Operating temperatures

Returning to the operating temperatures of the spacecraft components in Table 3.8, it can be seen that the BIT-3 Electric Propulsion System, which was the assumed propulsion system for the DST, has an operating temperature range of -15 to +45 ° C, or 258 to 318 K. Thus, it can be seen that for the coldest (for the detector) orbit results in a bus temperature that is below the temperature limit. The maximum temperature of +40 ° C, for the lithium-ion batteries is not exceeded. The 6 PM SSO minimum OLR cold case is rerun, with altered coatings to bring the bus temperatures within the specified limits. The nominal and maximum OLR cases are also rerun. This provides reference values and the maximum temperatures expected of the new coating design.

The zenith-facing surface mainly views deep space, with a slight side view of the sun. The zenith panel is currently covered in MS74 white paint, which allows it to radiate away a significant amount of heat. For this reason, the coating is changed to a 0.08 mil thick Kapton film with aluminum backing. This coating has a solar absorptivity of 0.23 and an emissivity in the IR spectrum of 0.24, taken from [47]. Replacing the coating on the zenith-facing panel yields the temperature results as seen in Table 6.6. The minimum bus temperature for

the minimum OLR cold case is 259 K, within the temperature limit. The nominal case detector temperature is increased slightly, to 120.2 K in the nominal case, increased from 117.1 K.

Component	Minimum OLR Temperature [K]	Nominal Temperature Minimum [K]	Nominal Temperature Maximum [K]	Maximum OLR Temperature [K]
Baffle Segment 1 (max)	261.2	271.2	274.6	286.1
Baffle Segment 2 (max)	262.7	270.6	279.9	292.2
Baffle Segment 3 (max)	282.2	269.6	300	313.6
Bus	259.2	272.2	275.8	284.6
Detector	115.9	120.2	120.2	123.2
Filter	185.7	195.9	195.9	202.7
Instrument Box	177.6	188.9	189.7	197.2
Radiator - Cold	174.3	185.2	185.2	192.3
Radiator - Cryo	115.1	119.5	119.5	122.4

Table 6.6: The updated coating configuration temperatures

Table C.11 in Appendix C shows the bus temperature range for the minimum OLR cases of all orbits. As can be seen, there is a significant variation in bus temperatures. This can be improved by changing the way this problem has been fixed. Currently, since the internal distribution of the components of the bus is not known, thermal insulation can not be applied to the components that must be warmer/colder. Once the internal design is known, the thermal design can then be adapted by placing insulation within the bus, allowing the bus to be within the temperature range without needing a specific external coating arrangement for each orbit.

6.3. Instrument box thermal gradient

The instrument box holds all internal optical components. It is of vital importance that the optical components contained in the instrument box are correctly aligned, as any misalignment will result in imperfect images. Requirements for the allowable alignment mismatch have not been defined yet. Therefore, at this moment, a characterization of the expected thermal gradient and the accompanying alignment length difference is the best option to determine the effects of the temperature difference. Future work on the design of the instrument box can then be done using these values as references. The thermal gradient will be investigated by taking the average temperature of each instrument box component. For reference, the instrument box's geometry is shown in Figure 6.7.

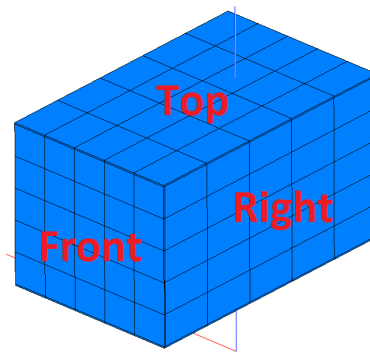


Figure 6.7: The detector temperature per orbit

The analysis of the thermal gradient will be done by changing the wall thickness of the instrument box sides. At this moment, the instrument box wall thickness is 1 mm. The coating configuration as determined in Section 6.2 is used for the thermal gradient analysis. The largest thermal gradient is between the front and the back sides of the instrument box, with a gradient of approximately 0.8 degrees. Since the centers of these components are aligned with the center of the optical chain, it is assumed that this is inconsequential for the optical alignment. The temperature gradient between the left and right sides is negligible, as their current design is symmetric. The gradient for the left and right sides is in the order of 0.001 degrees. The top and

bottom, however, have a slightly larger gradient. This is due to the location of the instrument box mounting. The (representative) mounting brackets are all placed near the top surface of the instrument box, resulting in a slightly higher temperature for the instrument box top. The temperature difference between the top and bottom is 0.125 degrees. The thermal expansion for aluminum is around $20 \times 10^{-6} \frac{m}{m^{\circ}C}$. With an instrument box length of 19 cm this results in an alignment mismatch of $4.75 \times 10^{-7} m$, or $0.475 \mu m$.

Increasing the instrument box wall thickness to 2 mm shows the same distribution of results. The largest thermal gradient is again between the front and back sides, with a gradient of 0.43 degrees. The left and right sides are again practically equal, while the top and bottom have a gradient of 0.065 degrees. The temperature difference was approximately halved in both cases. The halving of the temperature difference can be explained by the fact that the thermal conductor value is doubled since the cross-sectional area of the walls of the instrument box was doubled. Therefore, further increasing the wall thickness will show diminishing returns. With an increased wall thickness the length of the instrument box is increased to 19.2 cm, which results in a thermal alignment mismatch of $2.5 \times 10^{-7} m$, or $0.25 \mu m$.

Increasing the instrument box wall thickness to 3 mm again shows the same distribution of results. The maximum thermal gradient is between the front and the back, with a difference of 0.28 degrees. The gradient between the top and bottom is 0.042 degrees. As can be seen, further increasing the wall thickness shows diminishing returns. For the 3 mm case, the length is increased to 19.4 cm, which results in a thermal alignment mismatch of $1.63 \times 10^{-7} m$, or $0.163 \mu m$.

At this point, it can be seen that further increasing the instrument box wall thickness will not yield meaningful changes in the results. Combined with the fact that the thermal alignment mismatch is already very low, the conclusion can be made that the thermal gradient will likely not pose a problem for the DST demonstrator. The caveat to this conclusion is the conductors that represent the mounting equipment. These conductors are currently designed to have a very low conductivity. As the actual internal components and mounting configuration have not been determined yet, a conclusion can not be made. If it is determined for example, that more mounting brackets or stronger mounting brackets are required to meet natural frequency requirements, then the conduction into the top surface of the instrument box may increase, if the same mounting configuration is kept. This will in turn increase the thermal gradient. Section 6.4 will examine the impact of replacing all current (assumed) fiberglass conductors with titanium and steel conductors.

6.4. Conductor Material Investigation

In this section, the feasibility of the conductors used in the thermal model will be investigated. The current conductor design is based purely on the desire for low detector and instrument box temperatures. To compare the conductors, the nominal 6 PM SSO is used, with the standard bus heat input of 50 W. The results of these analyses are shown in Table 6.7. The temperature values are averaged, as was done in the sensitivity analysis.

Conductor Material	Conductor Value	Detector Temperature [K]	Instrument Box Temperature [K]
Fiberglass	Detector: 0.0001152 Instrument box: 0.000576 Radiators : 0.000269	120.2	189.3 ± 0.4
Titanium	Detector: 0.00456 Instrument box: 0.0228 Radiators : 0.0106	199.8	239.55 ± 2.2
Steel	Detector: 0.018 Instrument box: 0.09 Radiators : 0.042	235.6	256.15 ± 2.4

Table 6.7: The detector and instrument box temperatures for the different conductor materials

As can be seen, for both titanium and steel both the detector and instrument box temperatures do not meet the temperature requirements. This is not surprising as the conduction of titanium and steel is much higher than fiberglass, resulting in a higher heat input on the instrument box and subsequently the detector. This analysis highlights the importance of accurately determining the structural requirements for the instrument box, detector, and radiators. These requirements can then be used to determine the actual requirements for

the mounting equipment, allowing for a more thorough and accurate conductor definition.

6.5. Sensitivity Analysis

A sensitivity analysis is done over the bus heat generation, to alleviate concerns regarding the uncertainty of the bus heat input, determined in Section 3. The sensitivity analysis will be done from 0 W, up to a maximum value of 150 W, in iterations of 10 W. The simulations are performed over the nominal 6 PM SSO, with an instrument box wall thickness of 1 mm.

Table 6.8 shows the bus heat load values as well as the detector, bus, and instrument box temperatures. The temperatures represent the minimum and maximum temperatures on any component of the respective geometries. The temperature is shown as the median value, with the range depicting the minimum and maximum temperatures encountered. It can be seen that, even at a bus heat load of 150 W, the detector is still below the requirement of 150 K. This can be attributed to the well-insulated design of the detector and radiator mounting. The bus temperature is much more significantly affected. It can be seen that the current bus design is no longer within the allowable temperature limits for a bus heat load of 130 W. The instrument box temperature passes the 200 K limit at a bus heat input of 90 W, 40 W higher than the assumed bus heat input of 50 W.

Bus Heat Load [W]	Detector Temperature [K]	Bus Temperature [K]	Instrument Box Temperature [K]
0	111.4	236.95 ± 1.05	171.35 ± 0.25
10	113.4	245.7 ± 1	175.4 ± 0.3
20	115.3	253.5 ± 1.1	179.15 ± 0.35
30	117	260.7 ± 1.3	182.7 ± 0.4
40	118.7	267.45 ± 1.45	186.1 ± 0.4
50	120.2	274 ± 1.8	189.3 ± 0.4
60	121.7	280.2 ± 2.2	192.35 ± 0.45
70	123.1	286.1 ± 2.6	195.4 ± 0.5
80	124.4	291.7 ± 2.9	198.2 ± 0.5
90	125.7	297.05 ± 3.35	200.95 ± 0.55
100	127	302.2 ± 3.7	203.65 ± 0.55
110	128.2	307.15 ± 4.05	206.3 ± 0.6
120	129.3	311.85 ± 4.45	208.85 ± 0.65
130	130.4	316.5 ± 4.8	211.3 ± 0.7
140	131.5	320.9 ± 5.2	213.7 ± 0.7
150	132.5	325.2 ± 5.5	216.05 ± 0.75

Table 6.8: The bus heat load and accompanying temperature results for the sensitivity analysis

6.6. Baffle (Re)design

Section 4.1 determined that the baffle may become design driving due to the expected thickness of its segments. The baffle design is not considered part of this thesis' objectives, however further work on the baffle's deployment and segmentation will be done. To facilitate this work, in this section, the baffle components' temperatures will be determined for various coatings, and the MLI for different insulation values. The baffle's meshing will be refined, such that the temperatures are more accurately represented. Several additional coatings will be used in this analysis. A highly emissive MS74 White Paint, a reflective 425-3M aluminum foil tape, and a highly reflective and emissive Optical Solar Reflector. All of these coatings are taken from [47], and have emissivities and absorptivities of 0.92 & 0.17, 0.03 & 0.2, and 0.8 & 0.06, respectively.

The baffle re-design is split into two subsections, the coating analysis and the MLI analysis. The baffle will be converted into one continuous geometry, from the previously used three segments. This will allow for more accurate characterization of the heat fluxes it will experience during orbit. Its thickness will be set to 1 mm, and its material changed to aluminum. The coating analysis will analyze how the different coatings influence the temperatures of the baffle. There will be no MLI applied in the coating analysis, and thus the inside and outside temperatures of the baffle will be the same. In the MLI analysis, the MLI's effective emissivity and

cross-conductance will be varied. Both these analyses should provide insights into the baffle's behavior and provide a basis on which future work can be done on the baffle.

6.6.1. Coating Analysis

The coating analysis is done using a simple solid geometry, with the outer coating being varied for the different applied coatings. A separate case will be examined where the emissivity and absorptivity will be set at 0, which will be used as a verification case for the MLI analysis. A perfectly insulating MLI blanket should yield (nearly) identical results.

Coating	ϵ	α	Minimum Temperature[K]	Maximum Temperature [K]	Temperature Difference	Detector Temperature [K]
ϵ & $\alpha = 0$	0	0	273.2	284.5	11.3	121
MS74 White Paint	0.92	0.17	246.7	261.4	16.7	117.4
OSR	0.86	0.1	243.2	257.3	14.1	116.8
425-3M Tape	0.03	0.2	287.1	300.4	13.3	123.7
Kapton Foil (0.08 mil thick)	0.24	0.23	275.8	286.8	11	121.7

Table 6.9: The baffle temperature range during one orbit for the specified coating

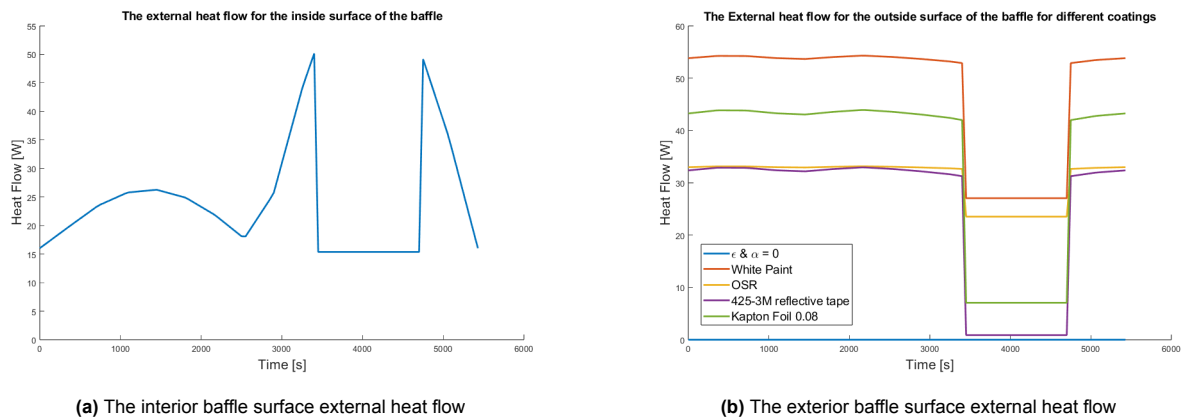


Figure 6.8: The external heat flow for the baffle surfaces for different exterior surface coatings

Table 6.9 shows the temperature range of the entire baffle for one orbit, and the associated detector temperature for the various applied coatings. As can be seen, the high emissivity coatings result in a lower baffle temperature. The OSR yields the lowest temperatures, for both the baffle and the detector. This can be attributed to its low absorptivity and high emissivity. The heat inputs on the inside and outside surface are shown in Figures 6.8a and 6.8b. As can be seen, the heat input on the baffle's internal surface is unchanged, as this coating is not changed. The peaks represent the heat input just before the eclipse. The heat input on the baffle's external surface is significantly impacted by the coating applied

From this analysis, it can be concluded that the optimal coating if a coated baffle is used would be an OSR. It is important to note that OSRs have a meaningful thickness. This can range from 0.05 to 0.5 mm, less than the thickness used for the analysis.[2] However, due to the current geometry of the baffle this may also require the OSR to be bendable. If this proves to be unnecessarily complex, then white paint proves itself to be a suitable alternative.

6.6.2. MLI Analysis

The MLI is modeled as described in Section 5.1.1. The underlying component (in this case the baffle) is assigned a polished aluminum outer coating, with an emissivity and absorptivity of 0.03 and 0.14, respectively.

MLI Insulation	Effective emissivity & Cross-Conductance	Minimum Temperature [K]	Maximum Temperature [K]	Temperature Difference	Detector Temperature [K]
2-layer	0.026 0.1651	274.4	284.6	10.2	120.2
Maximum Conduction	0.026 10000000	275.1	284.9	9.8	120.3
Full Isolation	0 0	273.6	284.8	11.2	120.2
case - 0.01	0.01 0.01	274	284.8	10.8	120.2
case - 0.005	0.005 0.005	273.8	284.8	11	120.2

Table 6.10: The baffle temperature range during one orbit for the different insulation values

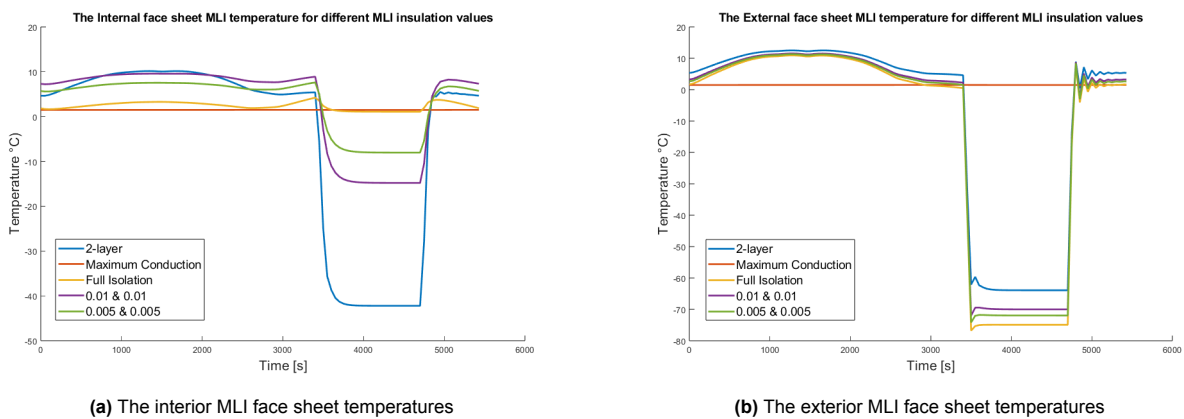


Figure 6.9: The interior and exterior MLI face sheet temperatures for different MLI insulation values

Table 6.10 shows the temperature range and detector temperature of the internal baffle surface. 2-layer represents the MLI as used for the baffle throughout this thesis. As can be seen, the temperature range is lower than for the coating analysis. However, the temperatures are higher for both the baffle and the detector. It can also be seen that the average internal baffle surface temperature does not change significantly with a change in insulation value. For the MLI itself, this is however not the case. Significant temperature swings are observed during the eclipse. Increasing the cross conductance to the max results in the same temperatures for both faces. If the MLI insulates better, the internal face sheet thermal fluctuations decrease, as can be seen in Figure 6.9a. The opposite is true for the external face sheet, as it transfers less heat to the internal face sheet, as can be seen in Figure 6.9b. It can also be seen that the temperatures for the perfect isolation are almost the same as for the ϵ & $\alpha = 0$ case in the coating analysis. The slight temperature difference can be attributed to the slightly increased area as the MLI is placed with an offset off of the underlying material.

The baffle coating and MLI analysis have shown several things. First of all, the coatings with high emissivity and low absorptivity provide optimal temperatures as far as detector performance is concerned. However, their thermal range is also higher. A key design parameter for the internal surface of the baffle will be the conductivity. In prior analyses, the baffle material was set as CFRP, which has a lower conductivity. This resulted in much higher temperature gradients over the baffle’s length. Therefore, an in-depth analysis of the baffle’s structural requirements should be done to determine the optimal material selection, where density and conductivity play the most important roles.

6.7. Final Design

The final design of the DST demonstrator’s TCS is shown in Figure 6.10a, in the deployed configuration. Figure 6.10b shows the TCS in the stowed configuration. Table 5.1 is repeated here, with the coatings as determined filled in. Inside refers to all surfaces facing toward the inside of the spacecraft, and outside refers

to all surfaces facing toward space. For the instrument box, inside refers to the surfaces facing the optical components, and outside refers to the surfaces facing the bus/nadir-facing surface and the R-side.

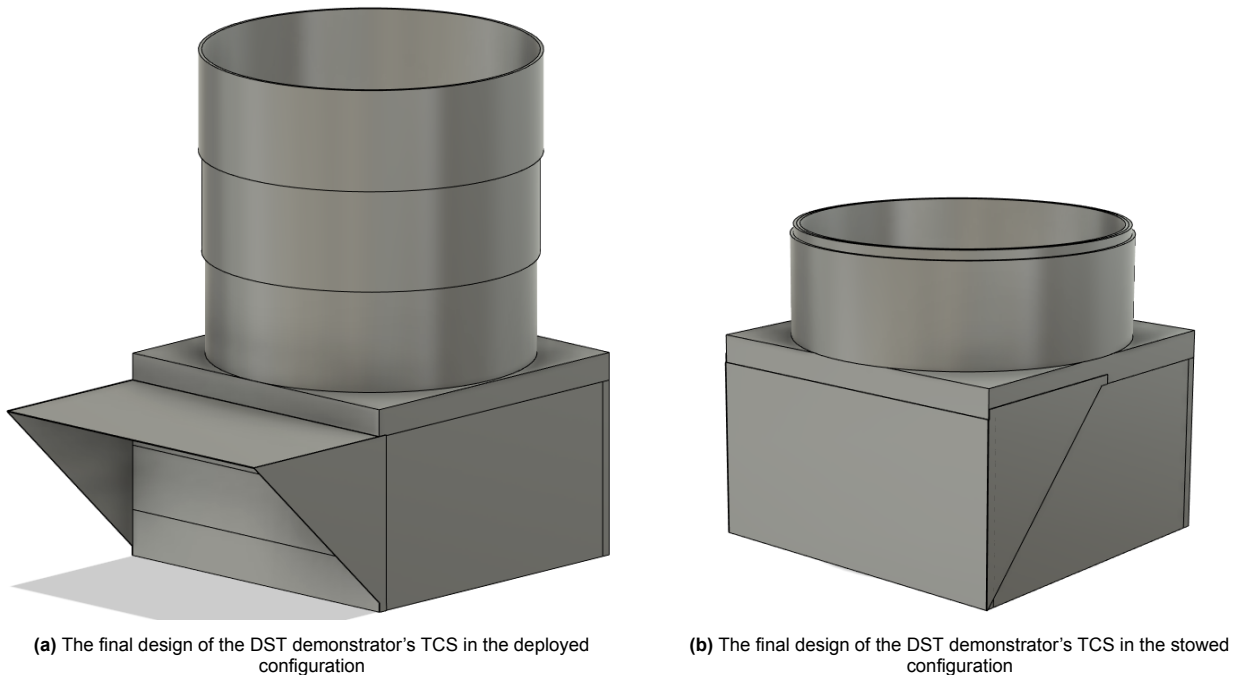


Figure 6.10: The interior and exterior MLI face sheet temperatures for different MLI insulation values

Component	Material	Coating(s)
M1	Boostec SiC	Protected Silver
M2	Boostec SiC	Protected Silver
Filter	Optical Glass	Optical Element
Detector	Optical Glass	Optical Element
Baffle	CFRP	Inside: Acktar ultra black Outside: 2-layer MLI
Bus	BusMat	MLI ($\epsilon = 0.01$)
Earth shade door	Aluminum	Polished aluminum
Instrument box	Aluminum	Inner surfaces: Acktar ultra black Outside: White Paint MS74
Nadir facing surface	Aluminum	Inside: 425-3M Aluminum Foil Tape Outside: White Paint MS74
Radiator (cryo)	Aluminium	Inside: MLI ($\epsilon = 0.01$) Outside: White Paint MS74
Radiator (cold)	Aluminium	Inside: MLI ($\epsilon = 0.01$) Outside: White Paint MS74
Side panel R	AluHoneycomb	White Paint MS74
Side panel 1	AluHoneycomb	White Paint MS74
Side panel 2	AluHoneycomb	White Paint MS74
Side panel 3	AluHoneycomb	White Paint MS74
Zenith panel	AluHoneycomb	Inside: White Paint MS74 Outside: Aluminum backed Kapton foil (0.08 mil thick)
SMDS legs	CFRP	Acktar ultra black
SMDS spider	CFRP	Acktar ultra black

Table 6.11: The different components of the spacecraft and their corresponding materials and coatings.

6.8. Chapter Summary

In this chapter, several additional analyses of the DST's design have been done. The orbital analysis has found that the 3 PM SSO yields the lowest detector temperature, owing to its orbital orientation, allowing for the near-complete occultation of the radiators. The worst-case analysis has shown the extremes of the temperature range to which the DST may be subjected. The zenith panel has been slightly redesigned, as the bus became too cold during the cold-case analyses. It is now covered in 0.08 mil thick Kapton foil with aluminum backing, to reduce the heat that it radiates away. The potential alignment mismatch of the optical elements due to the thermal gradient of the instrument box has been investigated and found to be close to negligible. However, since the alignment requirements of the optical elements are not known, this can not be said with full certainty, therefore several reference values have been determined. The sensitivity analysis has shown that the detector temperature is below the requirements even for a bus heat load triple the current amount. The bus and instrument box temperatures do not meet the requirements, and thus, for the current design, the bus heat load should not exceed 90 W. The influence of changing the conductor materials on the detector and instrument box temperatures is investigated, and it is determined that stiffer materials will result in unsatisfactory results. Finally, the baffle temperatures are determined for different coatings, as it is found that the baffle may become design-driving due to its width. The baffle analysis shows that the baffle may function better if it is made of highly conductive material with a high-emissivity low-absorptivity material on the outside.

7

Conclusion and Future Work

7.1. Conclusion

The thesis goal has been accomplished through the design of the radiators and the Earth shade door. The Earth shade door and its sides limit the incident heat on the radiators. The detector and instrument box temperature requirements, 150 K and 200 K, have been met and reduced further to 120.2 K and 189.7 K, respectively. This was achieved by answering the research questions.

The main research question was:

"How can the Thermal Control System of Earth observation satellites in a constellation be optimized to meet operational requirements?"

The TCS is optimized by minimizing the internal and external heat inputs. Isolation of the radiators from the internal heat sources significantly reduces the radiator temperatures, and shielding the radiators from the external heat input reduces the temperatures further.

The reduction of the internal and external heat inputs and the determination of the importance of the orbit choice was answered in the research sub-questions. The sub-research questions were:

"Where do the limits of radiators lie?"

The limits of a radiator depend on several factors. These factors can be grouped into two groups. First, the limits of a radiator depend on the environment. The external circumstances impacting the radiator have the potential to cause significant heat inputs on the radiator. Through the design of the Earth shade door and optimization of the radiator surface area, the influence of the environment on the radiator is significantly reduced, but not eliminated. This allowed the detector temperature to be reduced from 196 K to 120.2 K. Comparing this to the theoretical detector temperature of 116.2 K, it is apparent that the influence of the environment has been significantly reduced (this value includes the incoming heat transfer through the instrument box and the internals of the satellite). The second aspect of the limits of a radiator depends on the internal heat input. The conduction through mounting brackets and radiation from (warmer) internal components negatively affects the potential temperature that can be reached. This was mitigated by using low-conductivity materials and MLI on the inside surface of the radiator, as well as covering the bus with MLI.

"To what extent is the orbit choice a design driver for the thermal control system of a satellite?"

The orbit choice creates different patterns of heat input for a satellite. The extent to which the orbit is a design driver then depends on the TCS design. The orbit analysis examined the 12 pm, 2 pm, 4 pm, 6 pm, 8 pm, 10 pm, and 12 am orbits. The orbit analysis was done after the radiator had been thoroughly investigated, and an Earth shade door and sides were added to the design. This resulted in a relatively robust design that showed a variation of approximately 4 degrees in the detector temperature. The only caveat to this point is that the satellite must be flipped horizontally for the orbits ranging from 12 AM to 12 PM (00:01 AM - 11:59 AM) when compared to the orbits ranging from 12 PM to 12 AM (12:01 PM - 11:59 PM) The pattern of the heat input results in changes in the internal temperatures of the satellite. Some orbits have longer eclipse times. The bus temperatures varied strongly for different orbits, for example, and fell below the temperature limits. However, this problem can be solved by applying insulation surrounding the bus subsystems.

7.1.1. Design Conclusions

The thermal analysis of the DST has shown that the radiator must be subdivided into cryo- and cold-stage radiators, which cool the detector and instrument box, respectively. This is necessary because the heat input from the instrument box dwarfs that of the detector, which naturally results in the detector and the instrument box reaching (close to) the same temperature. A design that uses only one radiator will result in instrument box temperatures that are lower (see the results for a cryo stage radiator height of 1 cm in Figure 5.18), but will result in detector temperatures that do not meet the requirements (as can also be seen in Figure 5.18). The external heat input on the radiator's surfaces increased the temperatures of the radiators significantly. Therefore, an Earth shade door is added, which reduces the external heat input. Subsequently, side covers were added to the Earth shade door, which provides near-complete shading to a portion of the radiator-side panel. The cryo- and cold-stage radiators were varied in dimensions until optimal dimensions of 7 cm by 36 cm (the width of the satellite) for both the cryo- and cold stage appeared. The cryo stage occupies the 7 cm high band closest to the Earth shade door, and the cold stage occupies the 7 cm band beneath it.

The Earth shade door's design has been investigated, and its dimensions have been determined. The Earth shade door is assumed to be stowed flush with the radiator surface in the stowed configuration. It is assumed that the Earth shade door will be mounted using a hinge that attaches it to the nadir-facing surface. With its current dimensions of 19 cm by 36 cm, a simple deployment mechanism will suffice to release the Earth shade door to its operational position. This may be done using a torsional spring and a release mechanism, ensuring that the Earth shade door stays in its deployed position. The sides of the Earth shade door limit the available space on the side panels. The location of the deployment tabs must likely be on the unoccupied half of the side panels. This will also limit the placement of (deployable) solar panels, for which no design is available yet.

An analysis of the baffle design was performed. At the start of this thesis, it was assumed that the baffle is covered with MLI. The baffle analysis showed that it may be beneficial to use a solid baffle coated with an OSR or white paint instead. This coating arrangement yields better results since the external surface is now also used for cooling. When MLI is applied to the outside, the external surface does not participate in the heating up of the baffle, but also not in the cooling down. When the outside surface is covered white and has a relatively high conductive path to the internal side of the baffle, it radiates much more heat away. Additionally, since the baffle's internal surface has a view of itself, the radiation that impinges on the internal surface of the baffle is radiated away with more difficulty if the outside is not used to radiate heat away.

7.2. Recommendations and Future Work

In this thesis, it was determined that passive cooling of the DST demonstrator is possible and feasible. However, the calculated temperatures are dependent on several assumptions. These assumptions were calculated to represent the real situation as accurately as possible, however, in many assumptions uncertainty lingers. Therefore, some aspects of the design considered vital for the assumptions on the TCS should be further investigated in future work.

7.2.1. The Spacecraft Structure and Bus

The most important assumptions are related to the radiator, instrument box, and detector mounting. The conduction through the mounting brackets to these components heavily impacts their thermal performance. In this thesis, the conductor values of the mounting equipment have been calculated with the assumption that the structural requirements would be met by the design as proposed. The structural requirements of the entire satellite should be determined so that more accurate conductor values can be determined. Especially important are the instrument box and detector structural requirements. To thermally isolate the instrument box from the rest of the environment, it is essentially a second-order structure (it is relatively disconnected from the other internal components). As a result, it will have its stiffness requirements to maintain alignment with the incoming light from the secondary mirror but will also be subject to parasitic motion from the satellite's main structure. For the detector, this is again the case as it is attached to the instrument box. This implies that the detector is subject to parasitic motion from the main structure and the instrument box, as well as its own structural requirements.

The structural requirements of the spacecraft cannot be decided without knowing the arrangement of the internal components. In this thesis, the internal components have been approximated and assumptions re-

garding their power and dimensions have been made. These assumptions should be re-examined and further investigated so that an internal design of the DST demonstrator can be made from which the structural design is then developed.

7.2.2. Baffle (Re)design

The thickness of the baffle segments results in a baffle that becomes too wide for the 27U CubeSat maximum dimensions. The baffle's coating arrangement was investigated, and it was determined that the baffle's temperatures were reduced by employing a thinner solid baffle with a high-emissivity external coating. However, the temperature stability is slightly inferior to that of the MLI-covered baffle. If the coldest (OSR-covered) baffle is taken as an example, it has a temperature variation of 14.1 degrees, whereas the temperature variation is 10.2 degrees for the MLI that was used throughout this thesis. The baffle redesign then depends on several factors. The structural requirements of the baffle, the temperature of the baffle, and the mass of the baffle. Increasing the baffle's thickness will increase the temperature stability, but also the mass, and will also decrease the amount of available space in the stowed configuration. This ties into the deployment mechanism, which must still be designed. The baffle's stowed height has become design driving, as its length now constrains the available space for other components. By increasing the number of segments, the stowed height can be reduced, so more space is available for the bus and other internal components. Increasing the number of segments increases the effective thickness of the baffle.

7.2.3. The Earth Shade door

The Earth shade door has been added as a new component in this thesis. The addition and interfacing of this component should be investigated. This refers to both the mechanical interfacing and the stiffness and operational requirements of the Earth shade door. The deployment mechanism is a key aspect of the design. The deployment should be simple enough that it cannot fail during deployment, but it should not be rattled loose during launch and deployed prematurely.

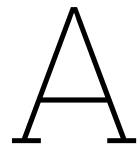
References

- [1] Mar. 2018. URL: [https://landsat.gsfc.nasa.gov/article/tirs-2-testing-a-landsat-9-instrument-takes-shape/#:~:text=There%20will%20be%20two%20radiators,%2F%20%2D88%C2%B0%20C\)..](https://landsat.gsfc.nasa.gov/article/tirs-2-testing-a-landsat-9-instrument-takes-shape/#:~:text=There%20will%20be%20two%20radiators,%2F%20%2D88%C2%B0%20C)..)
- [2] 2019. URL: <https://www.excelitas.com/product/optical-solar-reflectors>.
- [3] 2020. URL: https://www.esa.int/Enabling_Support/Space_Engineering_Technology/Shaping_the_Future/New_low_dark_current_detector_to_improve_noise_targets.
- [4] ACKTAR Ltd. *Ultra Black Coating*. 2023. URL: <https://acktar.com/product/ultra-black/>.
- [5] Alucoil. *Larcore Aluminum Honeycomb Panel*. 2021. URL: https://alucoil.com/wp-content/uploads/2021/06/CATALOGO_TRANSPORTE_INDUSTRIA_2021_INGLES_v1.0.pdf.
- [6] B. Anderson, Carl Justus, and G. Batts. "Guidelines for the Selection of Near-Earth Thermal Environment Parameters for Spacecraft Design". In: (Nov. 2001).
- [7] Arianespace. *Ariane 5 User's Manual*. 2016. URL: https://www.arianespace.com/wp-content/uploads/2011/07/Ariane5_Users-Manual_October2016.pdf.
- [8] Rodrigo Avila de Luis. *Standardized Thermal Control Solutions for PocketQubes*. URL: <http://resolver.tudelft.nl/uuid:2ef2af77-188b-4b1e-831e-d7fa31693b5c>.
- [9] AZO materials. *Titanium Alloys - Ti6Al4V Grade 5*.
- [10] Pradeep Bhandari. *Effective Solar Absorptance of Multilayer Insulation*. 2009. DOI: <https://doi.org/10.4271/2009-01-2392>.
- [11] Karl Bilimoria and Rogier Krieger. "Slot Architecture for Separating Satellites in Sun-Synchronous Orbits". In: *AIAA SPACE 2011 Conference & Exposition*. DOI: 10.2514/6.2011-7184. eprint: <https://arc.aiaa.org/doi/pdf/10.2514/6.2011-7184>. URL: <https://arc.aiaa.org/doi/abs/10.2514/6.2011-7184>.
- [12] Ronald J. Boain. "A-B-Cs of sun-synchronous orbit mission design". In: (Feb. 2004). URL: <http://hdl.handle.net/2014/37900>.
- [13] Boedeker Plastics. *G-10 Fiberglass Epoxy Laminate Sheet*. 2023. URL: https://www.matweb.com/search/datasheet_print.aspx?matguid=8337b2d050d44da1b8a9a5e61b0d5f85.
- [14] Lars Boer. *Personal consultation & Literature Study*. 2022.
- [15] J. Bouwmeester and J. Guo. "Survey of worldwide pico- and nanosatellite missions, distributions and subsystem technology". In: *Acta Astronautica* 67.7 (2010), pp. 854–862. ISSN: 0094-5765. DOI: <https://doi.org/10.1016/j.actaastro.2010.06.004>. URL: <https://www.sciencedirect.com/science/article/pii/S0094576510001955>.
- [16] Tom van Boxtel. *Thermal modelling and design of the DeFFi satellites*. URL: <http://resolver.tudelft.nl/uuid:a77149c9-4fd0-4cdc-ade9-6c5aca719a64>.
- [17] Ratnakumar Bugga et al. "Lithium Ion Batteries for Space Applications". In: *2007 IEEE Aerospace Conference*. 2007, pp. 1–7. DOI: 10.1109/AERO.2007.352728.
- [18] Busek Space Propulsion Systems. *BIT-3 RF Ion Thruster*. URL: https://satcatalog.s3.amazonaws.com/components/980/SatCatalog_-_Busek_-_BIT-3_CubeSat_System_-_Datasheet.pdf?lastmod=20211014051836.
- [19] Andrew F. Cheng et al. "AIDA DART asteroid deflection test: Planetary defense and science objectives". In: *Planetary and Space Science* 157 (2018), pp. 104–115. ISSN: 0032-0633. DOI: <https://doi.org/10.1016/j.pss.2018.02.015>. URL: <https://www.sciencedirect.com/science/article/pii/S0032063317304579>.
- [20] Fred G. Cunningham. *CALCULATION OF THE ECLIPSE FACTOR FOR ELLIPTICAL SATELLITE ORBITS*. URL: <https://ntrs.nasa.gov/api/citations/19630000622/downloads/19630000622.pdf>.

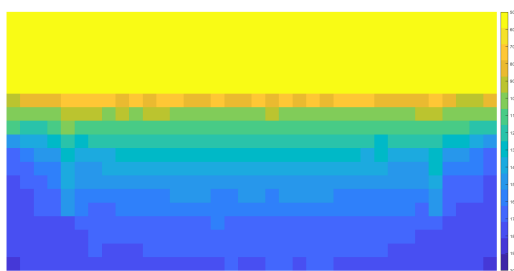
- [21] H.D. Curtis. "Orbital Mechanics for Engineering Students". In: *Orbital Mechanics for Engineering Students* (Oct. 2013), pp. 1–751.
- [22] Dennis Dolkens. "A Deployable Telescope for Sub-Meter Resolutions from MicroSatellite Platforms". In: (Feb. 2015). URL: <http://resolver.tudelft.nl/uuid:8f73b31c-4306-4b44-9937-3b4d23a4a53f>.
- [23] Eelco Doornbos et al. "The Need for a Standard for Satellite Drag Computation to Improve Consistency Between Thermosphere Density Models and Data Sets". In: 2013.
- [24] Engineers Edge. *Specific Heat Capacity of Metals Table Chart*. 2023. URL: https://www.engineerseedge.com/materials/specific_heat_capacity_of_metals_13259.htm.
- [25] eoPortal. *CubeSat - Deployer Standards*. 2012. URL: <https://www.eoportal.org/other-space-activities/cubesat-deployer-standards#payload-specification-for-6u-12-u-and-27u-configurations>.
- [26] eoPortal. *CubeSat - Deployer Standards*. 2012.
- [27] eoPortal. *CubeSat Concept and the Provision of Deployer Services*. 2012. URL: <https://www.eoportal.org/other-space-activities/cubesat-concept#isipod-isis-payload-orbital-dispenser>.
- [28] ESA - eoPortal. *DST (Dobson Space Telescope)*. URL: <https://www.eoportal.org/satellite-missions/dst#dst-8-development-on-a-cubesat-platform>.
- [29] European Space Agency - C. Siemes. *Swarm satellite thermo-optical properties and external geometry*. 2019. URL: <https://earth.esa.int/eogateway/documents/20142/37627/swarm-thermo-optical-properties-and-external-geometry.pdf>.
- [30] F. Zhu. *A Guide to CubeSat Mission and Bus Design - 5.5 Power Generation*. URL: <https://pressbooks-dev.oer.hawaii.edu/epet302/chapter/5-5-power-generation/>.
- [31] Max Gulde et al. "Reliable, Fast, and Flexible: A Thermal Modeling Approach for Small Satellites". In: (July 2018). URL: <https://digitalcommons.usu.edu/smallsat/2018/all2018/426/>.
- [32] A. M. Head. "High Efficiency Optical Solar Reflectors for Spacecraft". In: *SAE Transactions* 98 (1989), pp. 734–737. ISSN: 0096736X. URL: <http://www.jstor.org/stable/44471674> (visited on 01/17/2023).
- [33] Christiaan Hobijn. *Design, Construction and Validation of a secondary mirror deployment mechanism for a thermal infrared space telescope*. URL: <http://resolver.tudelft.nl/uuid:e0f486ff-bab6-4d6f-9c9b-44bc359f102c>.
- [34] <https://www.jpl.nasa.gov>. *Oblique Shot of Earth*. Sept. 2008. URL: <https://www.jpl.nasa.gov/images/pia11066-oblique-shot-of-earth>.
- [35] Fabbio Hu. *Thermo-Optical System Design of the Delft Deployable Space Telescope Baffle*. URL: <http://resolver.tudelft.nl/uuid:9956be48-3aaf-40e7-b85d-2941384a4294>.
- [36] Iberisa. *Heat Transfer from a Chip to PCB with GLUE Surface-to-Surface Thermal Coupling*. URL: http://www.iberisa.com/soporte/femap/termico/Heat_Transfer_from_Chip_to_PCB.htm.
- [37] Imetra. *SILICON CARBIDE MATERIAL PROPERTIES*. 2023. URL: <https://www.imetra.com/silicon-carbide-material-properties/>.
- [38] Ispispace. *Small Satellite - Cubesat Solar Panels*. URL: <https://www.ispispace.nl/product/isis-cubesat-solar-panels/>.
- [39] ITP Engines UK Ltd. *ESATAN-TMS Workbench User Manual*. 2021.
- [40] J. W. Arink. "Thermal Mechanical Design of a Baffle for the Deployable Space Telescope". In: (Oct. 2019). URL: <http://resolver.tudelft.nl/uuid:4ff37e5f-f155-44bb-8fee-408f6d799053>.
- [41] J.R. Wertz, Wiley J. Larson. *Space Mission Analysis and Design*. Microcosm, 2005. ISBN: 1881883108.
- [42] Paul Jerram and James Beletic. "Teledyne's high performance infrared detectors for Space missions". In: *International Conference on Space Optics — ICSO 2018*. Ed. by Zoran Sodnik, Nikos Karafolas, and Bruno Cugny. Vol. 11180. International Society for Optics and Photonics. SPIE, 2019, p. 111803D. DOI: 10.1117/12.2536040. URL: <https://doi.org/10.1117/12.2536040>.
- [43] Ronald Joven. "Thermal properties of carbon fiber/epoxy composites with different fabric weaves". In: Jan. 2012.

- [44] Robert D. Karam. *Satellite Thermal Control for Systems Engineers*. 1998. URL: <https://ebookcentral-proquest-com.tudelft.idm.oclc.org/lib/delft/detail.action?docID=3111611#>.
- [45] Ilkka Korhonen and Jero Ahola. "Estimating the specific heat capacity and heating of electronic sensors and devices". In: *IEEE Instrumentation & Measurement Magazine* 21.1 (2018), pp. 54–62. DOI: 10.1109/MIM.2018.8278813.
- [46] Kuiper, H., Dolkens, D. *A cutting edge 6U CubeSat ADCS design for Earth observation with sub-meter spatial resolution at 230–380 km altitude*. URL: <https://link.springer.com/article/10.1007/s12567-020-00323-7#citeas>.
- [47] L. Kauder. *Spacecraft Thermal Control Coatings References*. 2005. URL: <https://core.ac.uk/download/pdf/42754764.pdf>.
- [48] Lun Liu et al. "Thermal-structural analysis for flexible spacecraft with single or double solar panels: A comparison study". In: *Acta Astronautica* 154 (2019), pp. 33–43. ISSN: 0094-5765. DOI: <https://doi.org/10.1016/j.actaastro.2018.10.024>. URL: <https://www.sciencedirect.com/science/article/pii/S0094576518306337>.
- [49] Takeshi Miyakita et al. "Evaluation of Thermal Insulation Performance of a New Multi-Layer Insulation with Non-Interlayer-Contact Spacer". In: (July 2015). URL: <http://hdl.handle.net/2346/64487>.
- [50] NASA. *Specific Impulse*. URL: <https://www.grc.nasa.gov/www/k-12/rocket/specimp.html>.
- [51] NASA smallsat institute - S. Caldwell. "Thermal Control". In: (Nov. 2021). URL: <https://www.nasa.gov/smallsat-institute/sst-soa/thermal-control>.
- [52] J. Michael Owen et al. "Spacecraft Geometry Effects on Kinetic Impactor Missions". In: *The Planetary Science Journal* 3.9 (Sept. 2022), p. 218. DOI: 10.3847/PSJ/ac8932. URL: <https://dx.doi.org/10.3847/PSJ/ac8932>.
- [53] AGNE PASKEVICIUTE. *Preliminary Lander CubeSat Design for Small Asteroid Detumbling Mission*. URL: <https://kth.diva-portal.org/smash/get/diva2:1303001/FULLTEXT01.pdf>.
- [54] Qioptic. *Optical Solar Reflectors*. URL: https://www.excelitas.com/file-download/download/public/58606?filename=Qioptiq_Space-Qualified_Solar_Reflectors_Datasheet.pdf.
- [55] R. A. Schowengerdt. *RADIOMETRY OF LAMBERTIAN SOURCES*. 2000. URL: <https://uweb.engr.arizona.edu/~dial/ece425/notes7.pdf>.
- [56] R. A. Schowengerdt. *SECTION II – OPTICAL TOOLS*. 2000. URL: <https://uweb.engr.arizona.edu/~dial/ece425/notes6.pdf>.
- [57] A Rogalski. "HgCdTe infrared detector material: history, status and outlook". In: *Reports on Progress in Physics* 68.10 (Aug. 2005), pp. 2267–2336. DOI: <https://doi.org/10.1088/0034-4885/68/10/r01>.
- [58] Satsearch. *CubeSat propulsion module 1U*. URL: <https://satsearch.co/products/dawn-aerospace-cubesat-propulsion-module-1u>.
- [59] Arrun Saunders, Graham G. Swinerd, and Hugh G. Lewis. "Deriving Accurate Satellite Ballistic Coefficients from Two-Line Element Data". In: *Journal of Spacecraft and Rockets* 49.1 (2012), pp. 175–184. DOI: 10.2514/1.A32023. eprint: <https://doi.org/10.2514/1.A32023>. URL: <https://doi.org/10.2514/1.A32023>.
- [60] SCHOTT North America, Inc. "TIE-31: Mechanical and thermal properties of optical glass". In: 2010.
- [61] Shanmugasundaram Selvadurai et al. "Passive Thermal Control Design Methods, Analysis, Comparison, and Evaluation for Micro and Nanosatellites Carrying Infrared Imager". In: *Applied Sciences* 12.6 (2022). ISSN: 2076-3417. DOI: 10.3390/app12062858. URL: <https://www.mdpi.com/2076-3417/12/6/2858>.
- [62] Sheldahl. *Sheldahl Product Bulletin*. URL: <https://www.sheldahl.com/sites/default/files/2017-09/IT0%5C%20-%5C%20GE.pdf>.
- [63] Sonja Caldwell - National Aeronautics and Space Administration. *6.0 Structures, Materials, and Mechanisms*. 2023. URL: <https://www.nasa.gov/smallsat-institute/sst-soa/structures-materials-and-mechanisms>.
- [64] SpaceX. *Falcon User's guide*. 2021. URL: https://www.engineersedge.com/materials/specific_heat_capacity_of_metals_13259.htm.

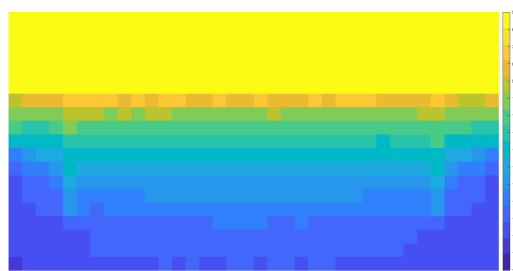
- [65] TU Delft. "Lecture slides AE4S20: Satellite Thermal Control". In: (2020).
- [66] Vacco Industries. *9 CubeSat propulsion systems & Modules to Review*. URL: <https://cubesat-propulsion.com/vacco-systems/>.
- [67] Vacco Industries. *Lunar Flashlight Propulsion System*. URL: <https://www.cubesat-propulsion.com/wp-content/uploads/2017/08/X16029000-01-data-sheet-080217.pdf>.
- [68] W. Holemans, R. Williams. *CANISTERIZED SATELLITE DISPENSER (CSD) AS A STANDARD FOR INTEGRATING AND DISPENSING HOSTED PAYLOADS ON LARGE SPACECRAFT AND LAUNCH VEHICLES*. 2014.
- [69] Kei Watanabe. *Concept Design and Development of 30kg Microsatellite HIBARI for Demonstration of Variable Shape Attitude Control*. URL: <https://digitalcommons.usu.edu/smallsat/2019/all2019/118/>.
- [70] Tim van Wees. "Thermal Modelling & Analysis of the Deployable Space Telescope". In: (Apr. 2019). URL: <http://resolver.tudelft.nl/uuid:f698fca7-205b-487d-b521-83d7f85e6fef>.
- [71] J.R. Wertz, D.F. Everett, and J.J. Puschell. *Space Mission Engineering: The New SMAD*. Space technology library. Microcosm Press, 2011. ISBN: 9781881883159. URL: <https://books.google.nl/books?id=VmQmtwAACAAJ>.
- [72] Wikipedia. *Longitude of the ascending node*. URL: https://en.wikipedia.org/wiki/Longitude_of_the_ascending_node.
- [73] Wikipedia. *Tsiolkovsky rocket equation*. URL: https://en.wikipedia.org/wiki/Tsiolkovsky_rocket_equation.
- [74] Wikipedia contributors. *Polyether ether ketone* — *Wikipedia, The Free Encyclopedia*. 2023. URL: https://en.wikipedia.org/w/index.php?title=Polyether_ether_ketone&oldid=1155740989.
- [75] Paul Zevenbergen et al. "Thermal Design of the Sentinel 5 precursor TROPOMI Instrument". In: 2012. DOI: <https://doi.org/10.2514/6.2012-3580>.



Optimal radiator surface area results

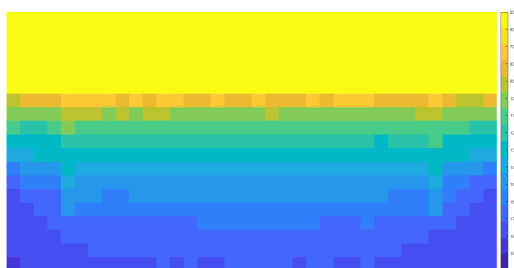


(a) The potential temperature for an Earth shade side size of 9 cm, using only the external heat input

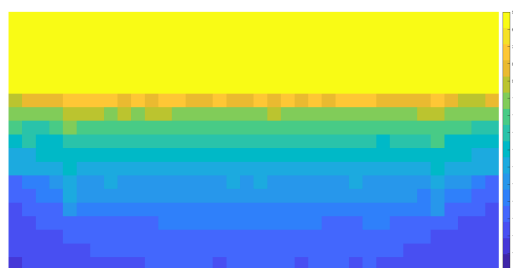


(b) The potential temperature for an Earth shade side size of 10 cm, using only the external heat input

Figure A.1: The potential temperatures for an Earth shade side size of 9 and 10 cm

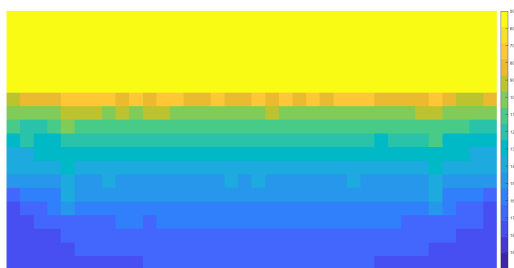


(a) The potential temperature for an Earth shade side size of 11 cm, using only the external heat input

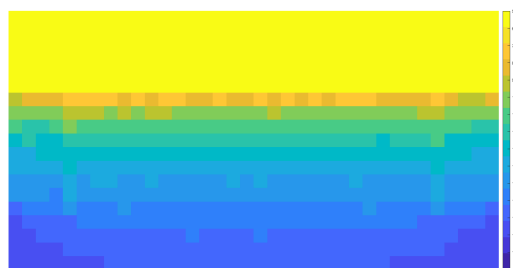


(b) The potential temperature for an Earth shade side size of 12 cm, using only the external heat input

Figure A.2: The potential temperatures for an Earth shade side size of 11 and 12 cm

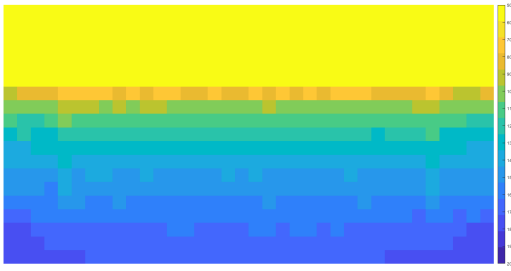


(a) The potential temperature for an Earth shade side size of 13 cm, using only the external heat input

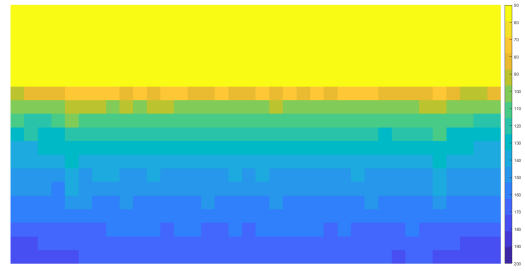


(b) The potential temperature for an Earth shade side size of 14 cm, using only the external heat input

Figure A.3: The potential temperatures for an Earth shade side size of 13 and 14 cm

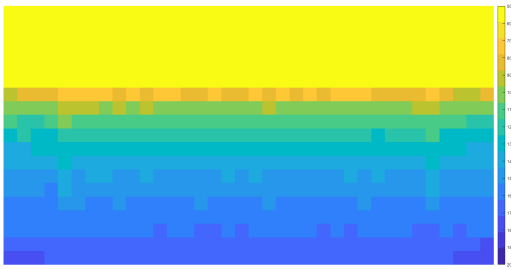


(a) The potential temperature for an Earth shade side size of 15 cm, using only the external heat input

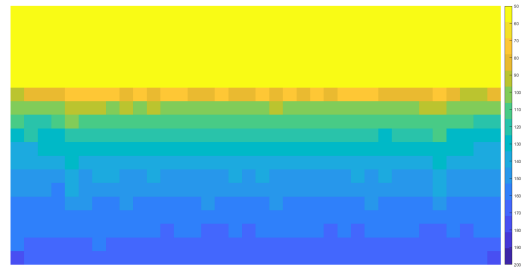


(b) The potential temperature for an Earth shade side size of 16 cm, using only the external heat input

Figure A.4: The potential temperatures for an Earth shade side size of 15 and 16 cm



(a) The potential temperature for an Earth shade side size of 17 cm, using only the external heat input



(b) The potential temperature for an Earth shade side size of 18 cm, using only the external heat input

Figure A.5: The potential temperatures for an Earth shade side size of 17 and 18 cm

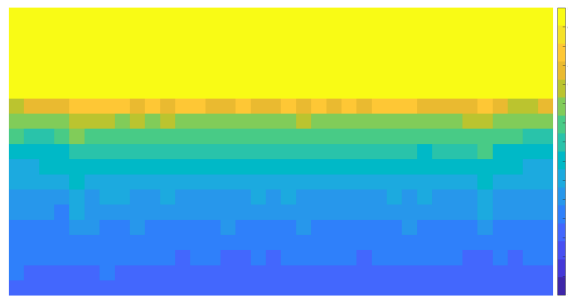
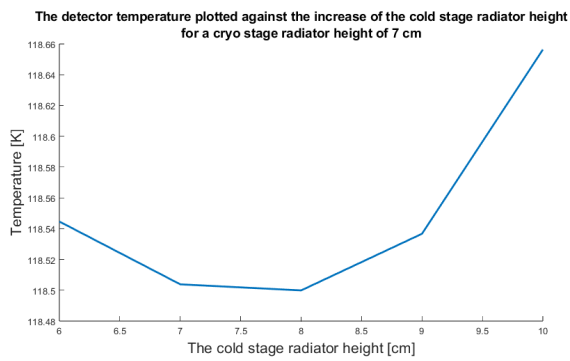


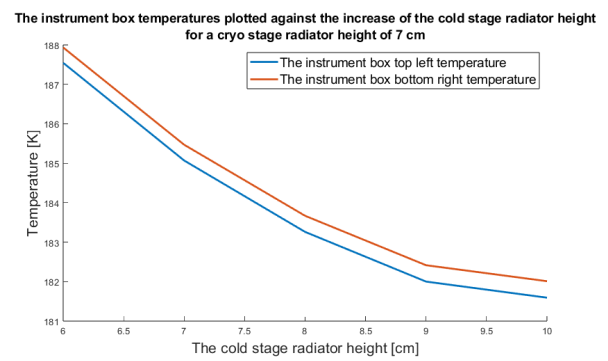
Figure A.6: The potential temperatures for an Earth shade side size of 19 cm, using only the external heat input

B

Cold Stage Analysis

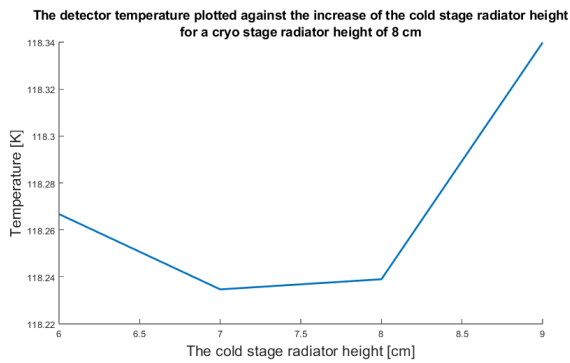


(a) The detector temperature for a cryo stage radiator height of 7 cm, with a varied cold stage height

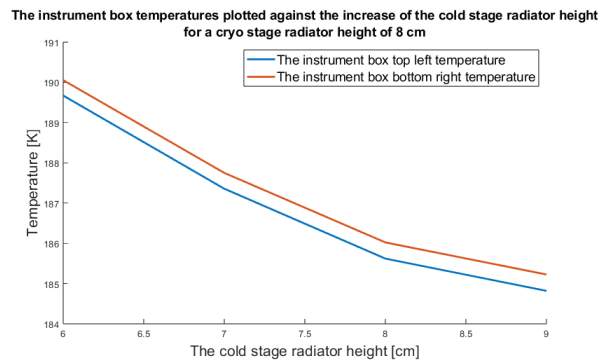


(b) The instrument box temperatures for a cryo stage radiator height of 7 cm, with a varied cold stage height

Figure B.1: The detector and instrument box temperatures for a cryo-stage radiator height of 7 cm

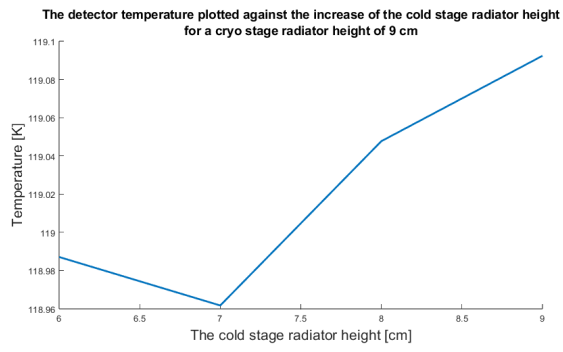


(a) The detector temperature for a cryo stage radiator height of 8 cm, with a varied cold stage height

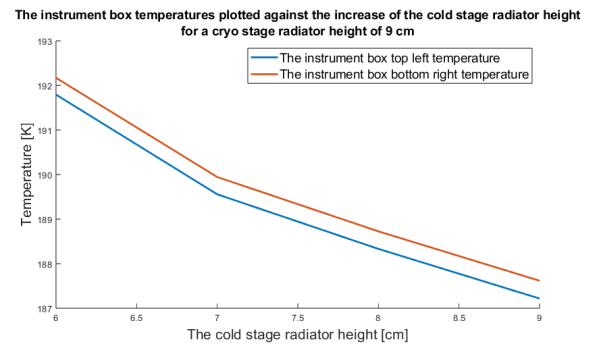


(b) The instrument box temperatures for a cryo stage radiator height of 8 cm, with a varied cold stage height

Figure B.2: The detector and instrument box temperatures for a cryo-stage radiator height of 8 cm



(a) The detector temperature for a cryo stage radiator height of 9 cm, with a varied cold stage height



(b) The instrument box temperatures for a cryo stage radiator height of 9 cm, with a varied cold stage height

Figure B.3: The detector and instrument box temperatures for a cryo-stage radiator height of 9 cm



Worst Case Analysis Results

Component	Minimum Temperature [K]	Maximum Temperature [K]	Temperature change over 10 Orbits
Baffle Segment 1	260.3	266.2	5.9
Baffle Segment 2	261.9	272.4	10.5
Baffle Segment 3	263.3	293.7	30.4
Bus	259.9	262.5	2.6
Detector	117.1	117.1	-
Filter	190	190	-
Instrument Box	182.4	183.2	0.8
Radiator - Cold	179.3	179.3	-
Radiator - Cryo	116.3	116.3	-

Table C.1: The results for the 6 PM SSO nominal case in the worst case analysis

Component	Minimum Temperature [K]	Maximum Temperature [K]	Temperature change over 10 Orbits
Baffle Segment 1	246.1	249.2	3.1
Baffle Segment 2	244.9	255	10.1
Baffle Segment 3	243.9	275.7	31.8
Bus	247.3	250.4	3.1
Detector	112.9	112.9	-
Filter	179.9	179.9	-
Instrument Box	171.1	171.8	0.7
Radiator - Cold	168.3	168.3	-
Radiator - Cryo	112.1	112.1	-

Table C.2: The results for the cold case - minimum OLR for the 6 PM SSO in the worst case analysis

Component	Minimum Temperature [K]	Maximum Temperature [K]	Temperature change over 10 Orbits
Baffle Segment 1	263.1	269.9	6.8
Baffle Segment 2	265	275.7	10.7
Baffle Segment 3	267.2	296.5	29.3
Bus	262.4	264.9	2.5
Detector	117.9	117.9	-
Filter	192.2	192.2	-
Instrument Box	184.8	185.5	0.7
Radiator - Cold	181.6	181.6	-
Radiator - Cryo	117.2	117.2	-

Table C.3: The results for the cold case - minimum albedo for the 6 PM SSO in the worst case analysis

Component	Minimum Temperature [K]	Maximum Temperature [K]	Temperature change over 10 Orbits
Baffle Segment 1	255.7	260.5	4.8
Baffle Segment 2	256.7	267.5	10.8
Baffle Segment 3	256.7	290.1	33.4
Bus	255.9	258.9	3
Detector	115.7	115.7	-
Filter	186.4	186.4	-
Instrument Box	178.4	179.1	0.7
Radiator - Cold	175.4	175.4	-
Radiator - Cryo	115	115	-

Table C.4: The results for the hot case - maximum albedo for the 6 PM SSO in the worst case analysis

Component	Minimum Temperature [K]	Maximum Temperature [K]	Temperature change over 10 Orbits
Baffle Segment 1	270	278.6	8.6
Baffle Segment 2	272.7	284.7	12
Baffle Segment 3	276.1	307.6	31.5
Bus	268.7	271	2.3
Detector	120	120	-
Filter	196.7	196.7	-
Instrument Box	189.8	190.6	0.8
Radiator - Cold	186.4	186.4	-
Radiator - Cryo	119.2	119.2	-

Table C.5: The results for the hot case - maximum OLR for the 6 PM SSO in the worst case analysis

Component	Minimum Temperature [K]	Maximum Temperature [K]	Temperature change over 10 Orbits
Baffle Segment 1	267	276.3	9.3
Baffle Segment 2	268.5	294.1	25.6
Baffle Segment 3	270.2	315.2	45
Bus	264.7	268.6	3.9
Detector	120.2	120.2	-
Filter	193.3	193.3	-
Instrument Box	186.1	186.8	0.7
Radiator - Cold	182.7	182.7	-
Radiator - Cryo	119.4	119.4	-

Table C.6: The results for the 12 PM SSO nominal case in the worst case analysis

Component	Minimum Temperature [K]	Maximum Temperature [K]	Temperature change over 10 Orbits
Baffle Segment 1	256.5	264.4	7.9
Baffle Segment 2	256.3	280.5	24.2
Baffle Segment 3	255.2	301.2	46
Bus	255.1	258.9	3.8
Detector	116.7	116.7	-
Filter	184.8	184.8	-
Instrument Box	176.6	177.3	0.7
Radiator - Cold	173.5	173.5	-
Radiator - Cryo	116	116	-

Table C.7: The results for the cold case - minimum OLR for the 12 PM SSO in the worst case analysis

Component	Minimum Temperature [K]	Maximum Temperature [K]	Temperature change over 10 Orbits
Baffle Segment 1	265.8	274.2	8.4
Baffle Segment 2	267.4	291.8	24.4
Baffle Segment 3	269.2	312.8	43.6
Bus	263.6	267.3	3.7
Detector	119.5	119.5	-
Filter	192.9	192.9	-
Instrument Box	185.7	186.4	0.7
Radiator - Cold	182.5	182.5	-
Radiator - Cryo	118.7	118.7	-

Table C.8: The results for the cold case - minimum albedo for the 12 PM SSO in the worst case analysis

Component	Minimum Temperature [K]	Maximum Temperature [K]	Temperature change over 10 Orbits
Baffle Segment 1	267.2	280.5	13.3
Baffle Segment 2	268.6	297.4	28.8
Baffle Segment 3	269.9	319.5	49.6
Bus	264.7	269.5	4.8
Detector	120.4	120.4	-
Filter	192.2	192.2	-
Instrument Box	184.8	185.6	0.8
Radiator - Cold	181.4	181.4	-
Radiator - Cryo	119.6	119.6	-

Table C.9: The results for the hot case - maximum albedo for the 12 PM SSO in the worst case analysis

Component	Minimum Temperature [K]	Maximum Temperature [K]	Temperature change over 10 Orbits
Baffle Segment 1	274	285.2	11.2
Baffle Segment 2	276.8	304.5	27.7
Baffle Segment 3	280.2	326.8	46.6
Bus	271.2	275.4	4.2
Detector	122.7	122.7	-
Filter	199	199	-
Instrument Box	192.3	193.1	0.8
Radiator - Cold	188.8	188.8	-
Radiator - Cryo	121.9	121.9	-

Table C.10: The results for the hot case - maximum OLR for the 12 PM SSO in the worst case analysis

Orbit	Minimum bus Temperature [K]	Maximum bus Temperature [K]
12 PM	269.3	274.6
2 PM	268.3	273.9
4 PM	262.6	267.5
6 PM	259.2	263.4
8 PM	262.6	267.5
10 PM	268.2	273.9
12 AM	269.7	275

Table C.11: The bus temperature range for each orbit, in the cold case - minimum OLR